

Lancaster
University



Centre
for Global
Eco-Innovation

This project was supported by the Centre for Global Eco-Innovation and is part
financed by the European Regional Development Fund

Simulation- and experiment-driven development of an optimized numerical strategy to design low-NO_x gas burners

Andrea Ortolani, MSc

School of Engineering, Lancaster University

A thesis submitted for the degree of

Doctor of Philosophy

May, 2025



European Union

European Regional
Development Fund

Abstract

Author: Andrea Ortolani

Title: Simulation- and experiment-driven development of an optimized numerical strategy to design low-NO_x gas burners

This thesis presents a comprehensive study of fluid dynamics and pollutant formation in non-premixed industrial gas burners through advanced computational fluid dynamics (CFD) modeling and experimental validation. Two main objectives guide the research: developing accurate and computationally affordable models for nitrogen oxides (NO_x) formation, and investigating the complex flow field within industrial burners.

Validation studies were conducted using the Sandia Flame D experiment. Turbulent combustion was modeled using the Flamelet Generated Manifold (FGM) approach, with both Reynolds-averaged Navier-Stokes (RANS) and Large Eddy Simulation (LES) methods. While both showed good agreement with experimental data, LES better captured streamwise mixture fraction variations. RANS tended to overpredict mixing rates, causing premature peak predictions for temperature and CO/OH mass fractions.

Three NO modeling approaches were evaluated: a baseline FGM scalar transport model (M1), a herein proposed non-adiabatic variant (M2), and a simplified "sum of contributions" model (M3). M2 improved prediction accuracy over M1, while M3 provided the best match for thermal NO predictions.

To address the challenges posed by the burner's complex geometry, a cold flow analysis was performed using three RANS turbulence models. The Reynolds Stress Model (RSM) with the baseline omega equation offered the best balance between accuracy and efficiency. Hybrid grid refinement strategies proved beneficial in regions of flow separation.

Subsequent unsteady RANS simulations of the industrial burner under varied thermal loads (41.7–87.5 kW) showed strong agreement with measured flue gas

temperatures (within 0.65%). M3 predicted NO emissions most accurately (54 ppm vs. 55 ppm measured) at full power. Thermal NO dominated at high loads, while prompt and N₂O-intermediate pathways were more relevant at low loads. M1 and M2 overpredicted emissions, with M2 performing slightly better.

This work advances burner design by providing validated modeling strategies for flow and emissions, enabling optimized performance with lower environmental impact.

Summary

This thesis presents a comprehensive investigation into the fluid dynamics and pollutant formation mechanisms of non-premixed industrial gas burners, based on the complementary use of advanced computational fluid dynamics (CFD) modeling and experimental validation. The work focuses on two key aspects: a) the definition and demonstration of accurate yet affordable modeling strategies for investigating the mechanisms of nitrogen oxides (NO_x) formation in industrial gas burners, and, b) the investigation of the flow field in said burners. The latter aspect is a challenging task in its own right, due to the geometric complexity of the system, but it is an essential prerequisite in the analysis and design of industrial burners, since the performance, efficiency and emissions of the combustor depend significantly on the details of the local flow field.

A detailed study of turbulent combustion in diffusion flames was undertaken considering the Sandia Flame D experiment as a validation test case. The combustion process was modeled by means of the Flamelet Generated Manifold (FGM) method. Both the Reynolds-averaged Navier-Stokes- (RANS) and Large Eddy Simulation- (LES) approaches were employed for this test case. The turbulence closure was accomplished by means of the Reynolds Stress Model (RSM) with the baseline (BSL) omega equation in the former approach, and the Smagorinsky-Lilly dynamic subgrid-scale model in the latter. The overall agreement between both simulation approaches on one hand and measured data on the other, was found to be satisfactory, although some differences were observed: the measured variation of the mixture fraction in the streamwise direction of this cylindrical burner was resolved better by LES. The RANS overestimation of the fuel and oxidizer mixing rates resulted in this approach predicting an earlier occurrence of the peaks of temperature and mass fractions of carbon monoxide (CO) and hydroxide (OH) with respect to the experimental data. The values of the peak temperature predicted by RANS and LES were both in good agreement with measurements, but the LES analysis yielded more accurate predictions of the CO and OH profile maxima. Modeling of the NO

mass fraction was accomplished by means of three alternative approaches, all using an additional transport equation for the NO mass fraction, namely 1) the FGM scalar transport approach (M1), 2) a variant of the FGM scalar transport approach obtained by including the effects of non-adiabatic phenomena (M2), and 3) the so-called method of sum of contributions, whereby the source term of the NO transport equation is computed in a simpler fashion with respect to the other two methods (M3). The analyses of M1 and M2 overpredicted the peak of the NO mass fraction, although the inclusion of non-adiabatic corrections of M2 improved the agreement with the measured peak value. Conversely, the analysis of M3 underpredicted the measured NO peak. Based on plausible estimates of the thermal and prompt NO reported by other studies, these results appeared to indicate that M3 produced a fairly accurate prediction of thermal NO.

The study of the industrial gas burner started with the analysis of the cold flow fluid, addressing the challenges posed by the geometric complexity of the system (e.g. sharp turns, backward facing steps, and transversally injected jets). Three RANS turbulence closures were examined, namely the k-omega Shear Stress Transport (SST) model, RSM using the omega BSL equation, and RSM using the epsilon equation. Among these methods, RSM with BSL omega equation offered the best compromise between accuracy, numerical stability and affordability of the required computational burden. Limitations of wall function-based approaches were investigated, particularly in regions with flow separation. This pointed to the potential of hybrid grid refinement strategies for achieving optimal trade-offs of solution reliability and computational effort.

Building on these foundations, unsteady RANS RSM simulations using FGM for combustion modeling and analyses M1, M2, and M3 for NO_x formation were performed to investigate NO_x emissions in the non-premixed industrial gas burner for a wide range of operating conditions, varying from 41.7 to 87.5 kW of the input thermal power. All CFD analyses closely matched measured flue gas temperatures, with the largest discrepancies varying between 0.13 and 0.65 percent with respect to

performed measurements. This outcome highlights the importance of including heat transfer through the combustor boundaries, an effect modeled by the FGM approach to combustion, since the adiabatic flame temperatures of the considered regimes of this combustor are more than 400 degrees higher than the measured and computed flue gas temperatures. With regard to the prediction of the NO mass fraction in the flue gases, the analysis of M3 predicted a value of 54 ppm against a measured value of 55 ppm at full thermal power, which was the best agreement among the three methods. High-power conditions favored thermal NO pathways, while low-power conditions increased the relevance of prompt and N₂O-intermediate mechanisms. Among the three NO modeling strategies, the analyses of M1 and M2 overpredicted NO emissions, although M2 was in closer agreement with measurements, whereas the M3 analyses were more accurate for predicting thermal NO-dominant conditions.

The presented integrated numerical/experimental study advances the understanding of flow and emission characterization of industrial burners. The findings provide both actionable insights for designing burners with optimized performance and reduced environmental impact, and an optimized simulation framework to accomplish these design objectives.

Declaration

I declare that the work presented in this thesis is, to the best of my knowledge and belief, original and my own work. The material has not been submitted, either in whole or in part, for a degree at this, or any other university.

Andrea Ortolani

Publications

A. Ortolani, J. Yeadon, B. Ruane, M. Paul, and M. S. Campobasso. “Numerical and Experimental Analysis of the Cold Flow Physics of a Nonpremixed Industrial Gas Burner”. In: *J. Fluids Eng.* 145.8 (Apr. 2023), p. 081202

A. Ortolani, J. Yeadon, B. Ruane, M. C. Paul, and M. S. Campobasso. “Numerical and experimental analysis of the formation of nitrogen oxides in a non-premixed industrial gas burner”. In: *Results in Engineering* 23 (2024), p. 102392. ISSN: 2590-1230

Contents

1	Introduction	7
1.1	Transition to net-zero	7
1.2	Nitric oxides emission in combustion	9
1.3	Role of computational fluid dynamics in combustion analysis	10
1.4	Research objectives	12
1.5	Thesis overview	14
2	Literature review	16
2.1	Turbulence modeling	17
2.2	Turbulent combustion modeling	18
2.3	Modeling NO formation in reference turbulent flames	21
2.4	Analysis of industrial burners flows	25
2.4.1	Cold flow analysis	25
2.4.2	Reacting flow and NO formation analysis	27
3	Governing equations	30
3.1	CFD method and turbulence modeling	30
3.1.1	Large Eddy Simulation approach	31
3.1.2	Reynolds Averaged Navier-Stokes approach	32
3.1.2.1	Two-equations models	32
3.1.2.2	Reynolds stress model	33
3.2	FGM method	33

3.2.1	Adiabatic look-up table	34
3.2.2	Non-adiabatic extension	36
3.2.3	CFD simulation and look-up table coupling	37
3.3	NO _x formation and modeling	38
3.3.1	NO _x formation	38
3.3.1.1	Thermal NO	38
3.3.1.2	Prompt NO	39
3.3.1.3	N ₂ O-intermediate NO	40
3.3.2	NO _x modeling methodologies	40
4	Combustion analysis of academic test case	45
4.1	Test case	46
4.2	Methodology	47
4.3	Results	54
4.4	Conclusions	61
5	Cold flow analysis of industrial gas burner	63
5.1	Test Rig	64
5.2	Experimental set-up	66
5.3	Computational fluid dynamics method	70
5.4	Numerical set-up	72
5.4.1	Physical domain and grids.	72
5.4.2	Boundary Conditions	74
5.5	Mesh sensitivity analysis	76
5.6	Results	79
5.6.1	CFD solution sensitivity to inlet BC and wall BLs resolution method	80
5.6.2	CFD solution sensitivity to turbulence model.	85
5.6.3	Flow field analyses	87
5.6.3.1	Flow field at design conditions	87

5.6.3.2	Flow field at off-design conditions	92
5.7	Conclusions	95
6	Combustion analysis of industrial gas burner	99
6.1	Test case and experimental rig	100
6.2	Set-up of CFD simulations	104
6.3	Results	109
6.3.1	Temperature field	109
6.3.2	NO _x field	113
6.4	Conclusions	123
7	Conclusions and Future Work	126

List of Tables

4.1	Boundary conditions at the inlet boundaries.	53
4.2	Contribution of each mechanism to peak NO computed by CFD, and expected range based on measurements and results of [46] and [90]	60
5.1	Dimensions of primary inlet duct, gas burner, and combustion chamber normalized by nozzle external diameter d_n	66
5.2	Mass flow rates and velocity RMS^A values on cross sections at positions L1, L2 and E3 computed with coarse, medium and fine grid $k - \omega$ SST P-WF set-up for operating condition V90.	78
5.3	Air mass flow rate estimated experimentally from the measured velocities and computed by the CFD prescribing the inlet total pressure for the V90 and V50 operating conditions	82
5.4	Reference pressures measured and computed by the CFD prescribing the inlet velocities for the V90 and V50 operating conditions.	83
5.5	Nondimensionalized static pressure p^* in the fuel inlet box evaluated with different set-ups for V90 and V50 conditions	84
5.6	Nondimensionalized static pressure p^* in the fuel inlet box measured and evaluated with different turbulence models for V90 and V50 conditions	87
6.1	Flue gas temperature and NO mass fraction computed with different levels of grid refinement	108
6.2	Power and overall equivalence ratio of the studied conditions.	109

List of Figures

2.1	Comparison of measured (symbols) and calculated (lines) mean NO mass fraction along the centerline for Sandia flame D. The figure is taken from Ihme et al. [46]	22
4.1	Picture of Sandia flame D taken from [7].	46
4.2	2D Computational grid.	48
4.3	Physical domain.	49
4.4	Computational grid.	50
4.5	Measured and computed profiles of Favre-averaged mixture fraction \tilde{Z} , temperature \tilde{T} , CO mass fraction \tilde{Y}_{CO} , and OH mass fraction \tilde{Y}_{OH}	55
4.6	Measured and computed profiles of Favre-averaged NO mass fraction \tilde{Y}_{NO} on the centreline of the flame.	58
5.1	Studied gas burner.	65
5.2	Inner views of gas burner.	66
5.3	Geometry parameters of primary inlet duct and gas burner.	67
5.4	Schematic of station 1.	69
5.5	Schematic of station 2. Black dots indicate pressure tap positions.	69
5.6	Schematic of station 3, and valve regulation.	70
5.7	Main dimensions and outer boundaries of physical domain.	73
5.8	Longitudinal section of medium refinement grid for analysis of V90 operating condition resolving boundary layers down to wall.	74

5.9	Measurement-based data for primary inlet boundary conditions at V90 and V50 conditions.	75
5.10	Profiles of V_x velocity components on transversal lines L1, L2 and E3 computed with coarse, medium and fine grid $k - \omega$ SST P-WF set-up for operating condition V90. Middle subplot also reports profiles of V_r velocity component.	78
5.11	Wall pressure profiles on lines F1 computed with coarse, medium and fine grid $k - \omega$ SST P-WF set-up for operating condition V90.	79
5.12	Analysis of solution sensitivity to inlet boundary conditions and wall BL modeling: computed and measured V_x profiles on transversal lines E1, E2, and E3 in combustion chamber.	81
5.13	Analysis of solution sensitivity to inlet boundary conditions and wall BL modeling: computed and measured nondimensionalized static pressure at V90 condition.	84
5.14	Analysis of solution sensitivity to turbulence model: computed and measured V_x profiles on transversal lines E1, E2, and E3 in combustion chamber.	86
5.15	Velocity field in burner case at V90 condition computed with RSM-BSL P-WR.	88
5.16	Velocity field in downstream part of burner case at V90 condition computed with RSM-BSL P-WR.	89
5.17	Nozzle velocity field at V90 condition computed with RSM-BSL P-WR.	89
5.18	Nondimensionalized static pressure field in burner case at V90 condition computed with RSM-BSL P-WR.	90
5.19	Measured and RSM-BSL P-WR profiles of nondimensionalized static pressure at V90 condition.	91
5.20	Measured and RSM-BSL P-WR V_x profiles on transversal lines E1, E2, and E3 in combustion chamber at condition V90.	91

5.21	Velocity field in burner case at V50 condition computed with RSM-BSL P-WR.	93
5.22	Velocity field in downstream part of burner case at V50 condition computed with RSM-BSL P-WR.	94
5.23	Nozzle velocity field at V50 condition computed with RSM-BSL P-WR.	94
5.24	Measured and RSM-BSL P-WR profiles of nondimensionalized static pressure at V50 condition.	95
5.25	Measured and RSM-BSL P-WR V_x profiles on transversal lines E1, E2 and E3 in combustion chamber at condition V50.	96
6.1	Burner and flow schematic.	101
6.2	Industrial burner physical domain.	104
6.3	Industrial burner mesh.	107
6.4	Measured and computed static temperature at the stack	110
6.5	Static temperature contour plots on the Z=0 and X=0.18m planes for the operating conditions A and D.	112
6.6	Measured and computed NO _x at the stack.	114
6.7	NO formation rate contour plots on the Z=0 plane for the operating conditions A.	116
6.8	Non-dimensionalized NO mass flow rate in the combustion chamber and transversal profiles of normalized oxygen molar fraction, temperature, and non-dimensionalized NO formation rate for operating conditions A.	118
6.9	NO formation rate contour plots on the Z=0 plane for the operating conditions D.	120
6.10	Non-dimensionalized NO mass flow rate in the combustion chamber and transversal profiles of normalized oxygen molar fraction, temperature, and non-dimensionalized NO formation rate for operating conditions D.	122

Nomenclature

Abbreviation

BC	Boundary Conditions
BL	Boundary Layer
CFD	Computational Fluid Dynamics
CFL	Courant-Friedrichs-Lewy number
CH ₄	Methane
CO	Carbon Monoxide
CO ₂	Carbon Dioxides
DNS	Direct Numerical Simulation
EDC	Eddy dissipation concept
EDM	Eddy-dissipation model
FB	Fuel box
FGM	Flamelet Generated Manifold
FPV	Flamelet Progress Variable
GHG	Greenhouse gas
H ₂ O	Water

Nomenclature

LES	Large Eddy Simulation
NO	Nitric Oxide
NO ₂	Nitrogen dioxide
NO _x	Nitrogen Oxides
PDF	Probability Density Function
PPSFM	Partially-premixed steady diffusion flamelet model
RANS	Reynolds Averaged Navier Stokes
RMS	Root Mean Square
RSM	Reynolds Stress Model
RSM- ϵ	Reynolds Stress Model with ϵ equation
RSM- ω	Reynolds Stress Model with standard ω equation
RSM-BSL	Reynolds Stress Model with baseline ω equation
SBES	Stress-blended eddy simulation
SGS	Subgrid-scale
SST	Shear Stress Tensor
TRI	Turbulence Radiation Interaction
UDF	User Defined Function
WF	Wall Function
WR	Wall Resolved flow
WSGGM	Weighted Sum of Gray Gases Model

Symbols

χ	Scalar dissipation rate
χ_{st}	Stoichiometric scalar dissipation rate
\dot{m}_{air}	Air mass flow rate
ϵ	Turbulent dissipation rate
η_c	Non-adiabatic correction factor to NO formation rate
κ_a	Mixture absorption coefficient
μ	Molecular viscosity
μ_{eff}	Effective viscosity
μ_{sgs}	Subgrid-scale viscosity
μ_t	Turbulent viscosity
ω	specific turbulent dissipation rate
Ω_{N_2O}	Formation rate of N ₂ O NO
Ω_{pr}	Formation rate of prompt NO
Ω_{th}	Formation rate of thermal NO
Φ	Equivalence ratio
ϕ	Reactive scalars
ρ	Mixture density
$\tau_{i,j}$	Reynolds stresses
\tilde{C}	Favre-averaged progress variable

Nomenclature

\tilde{H}	Favre-averaged total enthalpy per unit mass
\tilde{h}_{ad}	Adiabatic total enthalpy
\tilde{Z}	Favre-averaged mixture fraction
a	Oxygen reaction order
C	Progress Variable
C_v	Progress variable variance
d	Diameter of the Sandia flame D fuel nozzle
d_c	Diameter of the industrial burner combustion chamber
d_n	Diameter of the industrial burner nozzle
d_{p-in}	Inner diameter of coaxial nozzle in Sandia flame D nozzle
d_{p-out}	Outer diameter of coaxial nozzle in Sandia flame D nozzle
f	Function of number of carbon atoms in a fuel molecule
H	Total enthalpy per unit mass
h	Specific enthalpy per unit mass
h_b	Height and width of the industrial burner case
h_i^0	formation enthalpy of species i
H_e	Heaviside step function
k	Turbulent kinetic energy
$k_{f,x}$	Forward rates of reaction x
$k_{r,x}$	Reverse rates of reaction x

k_r	Reaction rate coefficient
k_t	Thermal conductivity
l_b	Length of the industrial burner case
l_c	Length of the industrial burner combustion chamber
$l_i n$	Length of the industrial burner inlet duct
l_{x_b}	Width of the industrial burner inlet duct
l_{x_h}	Height of the industrial burner inlet duct
$M_{w,i}$	Molar mass of species "i"
p	Static pressure
p^*	Nondimensionalized pressure
p_{t0}	Preference pressure
R	Gas constant
S	Reaction rate
s	Mean beam length
T	Static temperature
T_{ad}	Adiabatic static temperature
T_{nad}	Non-Adiabatic static temperature
$T_{ref,i}$	Reference temperature of formation of species i
V50	Partial load condition in the cold flow test
V90	Full load condition in the cold flow test

Nomenclature

V	Velocity
V_{b_c}	Mean flow velocity normal to a generic section
V_r	Radial component of velocity
V_x	X component of velocity
V_y	Y component of velocity
V_z	Z component of velocity
X_i	Mole fraction of chemical species i
y^+	Normalized wall distance
Y_i	Mass fraction of chemical species i
Y_j	Mass fraction of element j
Z	Mixture fraction
Z_v	Mixture fraction variance
A	Arrhenius constant
E_a	Activation energy

Chapter 1

Introduction

1.1 Transition to net-zero

Since scholars have established a causal relationship between the production of carbon dioxide (CO₂) and other greenhouse gases (GHGs) and climate change [107]; many actors, such as citizens, non-governmental organizations (NGOs) and climate activists, have invoked the application of environmental policies to reduce these pollutants [38]. Indeed, these gases have severe impacts on ecosystems, human health, and, consequently, on global and local economies [122]. On the other side, the positive link between CO₂ emissions and countries' economic growth, through manufacturing production, makes the transition toward zero carbon emissions a complex and costly process. Indeed, the green transition makes evident the governments' trade-off between job creation and environmental quality.

Governments across the world have set ambitious objectives to achieve net-zero carbon emissions, but these goals present immense challenges, both technically and socioeconomically. For instance, the United Kingdom initially pledged to reach net zero by 2050, yet in 2023 former Prime Minister Rishi Sunak scaled back some interim climate targets, citing the need for pragmatism and economic feasibility [9]. The decision highlights the tension between environmental commitments and the immediate economic costs of rapid decarbonization. According to the International

Energy Agency (IEA), achieving net zero globally by 2050 requires reducing coal demand by 90%, oil by 75%, and natural gas by 55% compared to 2020 levels [77]. These figures underscore the radical transformation required across key industries, transformations that are unlikely to happen overnight.

A key factor complicating the transition is the sheer scale of the fossil fuel sector, which remains a cornerstone of the global economy. In 2022, the oil and gas industry alone employed over 11.5 million people worldwide [126]. Similarly, coal, often considered the dirtiest fossil fuel, still accounted for about a third of global electricity production in 2022, according to the International Energy Agency [17]. Political decisions often reflect these realities. For instance, Germany, under pressure from energy shortages exacerbated by the war in Ukraine, temporarily increased coal-fired power generation despite its broader climate commitments [93]. Such actions reveal the difficulty of balancing energy security, economic stability, and environmental goals.

Reconverting these massive industries to sustainable alternatives requires a gradual and carefully managed approach. Abrupt shifts risk destabilizing economies, particularly in regions heavily reliant on fossil fuel extraction. For example, in 2023, the European Union allocated €17.5 billion to a "Just Transition Fund" to support communities dependent on coal, oil, and gas [19]. Yet, even with financial aid, transitioning workers to green jobs and repurposing infrastructure will take decades. As The World Economic Forum noted in a 2024 report, "As the world grapples with the urgent need to decarbonize, it has become increasingly clear that this transformation must be carried out in a just, equitable and inclusive manner" [12]. Policymakers face the monumental task of charting a course that addresses both environmental imperatives and socioeconomic realities, ensuring that the shift to net zero is both effective and equitable.

In this context, it appears clear that it is still crucial to make fossil fuel-based processes more efficient and reduce their environmental impact.

1.2 Nitric oxides emission in combustion

The use of combustion in industrial processes is related to its ability to release significant amounts of energy stored in fuels, which makes this phenomenon indispensable in many sectors. To achieve high efficiencies in processes based on thermodynamic cycles, combustion is often performed at high temperatures. For instance, in the Carnot cycle, which provides a theoretical limit for thermodynamic cycle efficiency, the efficiency increases as the maximum temperature of the cycle rises. This principle drives the design of many engines and power systems, motivating the pursuit of high-temperature combustion. However, higher temperatures also create conditions that promote the formation of nitrogen oxides (NO_x), harmful pollutants that result from high-temperature reactions between nitrogen and oxygen in the air.

In this context, it is worth mentioning the potential of Hydrogen combustion, which is an important topic in the field of clean energy. Hydrogen combustion offers a carbon-free alternative to conventional hydrocarbon fuels. Since hydrogen flames produce no CO_2 emissions, they are of particular interest for sustainable combustion applications. However, NO_x formation remains a challenge, making its study crucial for the development of low-emission hydrogen combustion technologies. Given the relevance of hydrogen combustion to the field in which this work is placed, insights and comments on NO_x formation in such flames are valuable.

NO_x typically includes nitric oxide (NO) and nitrogen dioxide (NO_2), which are produced in significant quantities and pose a variety of environmental and health risks. NO_x emissions are particularly concerning due to their harmful effects. These pollutants contribute to the formation of ground-level ozone and fine particulate matter, both of which have serious health implications, including respiratory and cardiovascular diseases [94]. Additionally, NO_x plays a critical role in the development of acid rain, which can damage forests, soils, and aquatic ecosystems [102]. Given these hazards, it is imperative to develop and implement strategies that mitigate NO_x emissions from combustion processes.

To do so means involving a combination of improving combustion technologies,

adopting cleaner fuels, and employing advanced emission control systems. By focusing on these areas, we can reduce the adverse effects of NO_x while continuing to transition towards a more sustainable and low-carbon future.

1.3 Role of computational fluid dynamics in combustion analysis

Computational Fluid Dynamics (CFD) is a critical tool for optimizing industrial processes due to its ability to simulate and analyze fluid behavior in various environments. By providing detailed insights into fluid flow, heat transfer, and related physical phenomena, CFD enables engineers and scientists to design more efficient systems, reduce costs, and enhance performance across a wide range of industries. For instance, CFD allows for the detailed visualization of fluid dynamics within complex geometries, making it possible to identify inefficiencies and areas for improvement in industrial processes. For example, in the chemical and process industries, CFD can simulate mixing and heat transfer within reactors, estimate reaction rates, and lead to optimized designs that enhance product yield and reduce energy consumption.

One of the strengths of CFD is its ability to reduce the need for expensive physical testing. Traditional methods of testing, such as wind tunnel experiments or full-scale prototypes, are often costly and time-consuming. CFD provides a virtual testing environment where multiple scenarios can be simulated quickly and at a fraction of the cost. This capability is particularly valuable in industries where safety and reliability are paramount, such as nuclear power, oil and gas, and pharmaceuticals. By identifying potential issues and optimizing processes in the virtual space, companies can mitigate risks, improve safety, and comply with regulatory standards more effectively.

In combustion modeling, CFD can be used to predict flame behavior, pollutant formation, and thermal efficiency with high precision. This capability enables

detailed modeling of various flame types, which can differ significantly in their behavior and characteristics. In particular, flames can broadly be classified into premixed and diffusion flames. In premixed flames, the fuel and oxidizer are thoroughly mixed before ignition, leading to a uniform flame front where the reaction zone propagates through the mixture. This type of flame generally offers high efficiency but requires careful control to avoid instability. In contrast, diffusion flames occur when fuel and oxidizer meet and react at the interface, with the mixing process governed by molecular diffusion and turbulence. These flames are slower burning and often produce higher levels of pollutants such as NO_x . By simulating these different flame types, CFD helps optimize combustion systems for energy efficiency and reduced emissions.

The turbulent nature of the combustion found in most industrial processes requires sophisticated turbulence models to capture the effects of turbulence-chemistry interactions (e.g.[41]). Three main approaches of different levels of fidelity exist to describe turbulence in the context of CFD. These are RANS (Reynolds-Averaged Navier-Stokes), LES (Large Eddy Simulation), and DNS (Direct Numerical Simulation). RANS simplifies turbulence by averaging the flow equations over time, focusing on mean flow properties and modeling all turbulence scales, making it computationally efficient but less detailed. LES resolves larger turbulent eddies directly while modeling smaller scales, striking a balance between computational cost and accuracy, and is often used for complex flows like combustion. DNS, on the other hand, resolves all scales of turbulence without any modeling, providing the most accurate results but at an extremely high computational cost, limiting its use to small and idealized problems.

Modeling NO_x emissions is complex and challenging as they are influenced by a multitude of factors ([46]). These include turbulence, heat transfer, and detailed chemical kinetics, all of which need to be accurately represented in the CFD simulation. The challenge lies in capturing the high-temperature reactions and the interaction between various species within the combustion chamber. The

accuracy of CFD models for NO_x prediction relies on the precise representation of these processes. Accomplishing this is not always possible, due to the unavoidably higher computational cost of more accurate (e.g. high-fidelity) analysis frameworks. Due to this, trade-offs of computational cost and fidelity level are often necessary, and finding the optimal balance is often challenging. This concept will be further described in Chapter 2.

Due to the challenge of finding a suitable trade-off between affordability and accuracy, especially in complex problems such as that of industrial gas burners, the models must be validated against experimental data to ensure their reliability. Validation involves comparing CFD predictions with measurements from controlled experiments or real-world scenarios, allowing for the calibration and refinement of the selected models. This process is essential to build confidence in the simulations and to ensure that they can provide accurate and actionable insights for optimizing industrial processes and reducing NO_x emissions also in scenarios different from those tested experimentally. Without thorough validation, the predictions from CFD models may be inaccurate or misleading, potentially leading to suboptimal or even counterproductive design decisions.

1.4 Research objectives

The work of this thesis focuses on an industrial test case. The considered test case is a non-premixed industrial burner for natural gas and methane combustion. The burner is designed to operate in continuous industrial processes with a firing range from 12 to 120 KW.

The primary goal of this thesis is to develop a computationally efficient RANS CFD technology, validated through experiments, for analyzing and designing industrial gas burners. The thesis aims to provide guidelines on the best choices for RANS CFD simulations of industrial gas burners.

This is achieved via the following objectives:

- 1** To create a computational model for analyzing the cold and reactive flow within the industrial gas burner in question using CFD tools.
- 2** To design and construct a full-scale experimental test rig capable of generating data for evaluating flow features in the industrial gas burner and its NO_x emissions, enabling a suitable comparative analysis with numerical modeling.
- 3** Conduct parametric analyses of the simulation setup, to evaluate and identify the most suitable modeling choices such as that of the turbulence and NO_x models.
- 4** To explore and elucidate the intricate fluid dynamics within an industrial gas burner.

The main novelty of this thesis is the investigation of the flow physics of a non-premixed industrial gas burner, and its dependence on the operating condition. Since the control of the turbulent flow pattern is one of the means available to improve the efficiency and reduce the emissions of this system, predicting and explaining the key flow features is paramount to its design optimization. Secondly, this thesis provides new experimental data in the context of non-premixed industrial gas burner physics. The experimental part of this investigation is carried out by using a full-scale test rig that reproduces the conditions in which the gas burner is operated in production. This makes the presented analyses relevant to both the scientific and industrial communities of this sector. The author provided key guidelines for the test rig design and independently conducted all experimental tests, ensuring reliable data collection and accurate results. This highlights the author's significant role in both the setup and execution of the experiments. Additional novelty features of this thesis include a systematic study on NO_x modeling approach in test flame and industrial burners. Moreover, a correction to the Flamelet Generated Manifold (FGM) scalar transport model for NO is proposed to enable accounting for the effect of non-adiabatic phenomena on NO formation without increasing the FGM look-up table dimensionality. This latter point will be better explained in Chapter 6.

1.5 Thesis overview

The outline of this thesis is as follows.

Chapter 2 provides an insight into relevant literature, providing an overview of published research related to the field of turbulent diffusion flame and NO_x formation modeling.

Chapter 3 presents the main governing equations which are of use in this thesis.

Chapters 4 to 6 are the core of this thesis and are developed according to the following workflow.

At first, an academic test case is considered to test modeling strategies and numerical set-up on a flame characterized by simple fluid-dynamic features (Chapter 4). This is Sandia Flame D, a well-established academic test case.

Secondly, the flow in the industrial gas burner at hand is modeled and measured with no flame in it, using air as the sole working fluid (Chapter 5). This allows for an understanding of the complex flow features found in the burner, such as flow separation, flow reattachment, and sudden changes in flow direction. This step is crucial, as many of the modeling difficulties found in this project arise from such fluid-dynamic features. Chapter 5 also provides insights on numerical strategies providing guidelines on the best choices in RANS CFD simulations of industrial gas burners.

The findings of Chapters 4 and 5 lay the foundation for the industrial application and the main analysis of this thesis. In Chapter 6 the analysis of the industrial gas burner is performed including combustion. The analysis, which focuses on the formation of nitrogen oxides (NO_x), provides insights into the burner flow physics and NO_x formation. Once again findings are supported by measurements and insights on numerical strategies for NO_x formation modeling are provided.

Finally, Chapter 7 provides a summary of the study with comments on future work.

The work presented in this thesis has been fully published in two peer-reviewed journal articles [82, 83]. These publications provide a comprehensive account of the

research findings and their contributions to the field.

This project is supported by the Centre for Global Eco-Innovation, the European Regional Development Fund, and Proctor Process Plant. All the simulations in this work were run on the Lancaster University High End Computing (HEC) cluster [58].

Chapter 2

Literature review

Turbulent combustion is notoriously challenging to model, as it sits at the boundary of two strongly nonlinear phenomena interacting with each other: chemistry and turbulence. This chapter presents an insight into relevant literature, providing an overview of published research related to the field of turbulent diffusion flame and NO_x formation modeling. The chapter is divided into four parts. The first part briefly discusses the strategies used to model turbulence in CFD and how these have an effect in the context of turbulent combustion modeling. The second part of the chapter discusses the main strategies commonly used to model turbulent combustion in the context of CFD. A comparison of the strengths and weaknesses of said strategies leads to the choice of using a strategy based on reduced order models in this thesis. The third part of the chapter discusses the application of reduced order models in laboratory test flames with a particular focus on NO_x formation modeling. Finally, the fourth part of the chapter discusses the main modeling strategies that have been used in literature to model both the non-reacting and reacting flow in industrial burners, with a particular focus on NO_x formation.

2.1 Turbulence modeling

Modeling turbulence in CFD is a complex and essential task for accurately predicting fluid behavior in various engineering and scientific applications. The approaches to modeling turbulence can be broadly categorized into several methods, each with its strengths and limitations. The main methods are briefly described herein.

Direct Numerical Simulation (DNS) resolves all the scales of turbulence by solving the Navier-Stokes equations directly without any modeling assumptions. Despite it provides highly accurate results, the very high computational cost makes it impractical for most real-world engineering problems.

Large Eddy Simulation (LES) resolves the large scales of turbulence directly while modeling the smaller scales. Modeling of the smallest scales is achieved via a so-called subgrid-scale model. LES provides a good compromise between accuracy and computational cost, capturing the behavior of the large eddies, which are crucial for many engineering applications. In many cases, especially for high Reynolds number flows and complex geometries, LES is still computationally expensive.

In Reynolds-Averaged Navier-Stokes (RANS) approaches the entire turbulence spectrum is modeled. The Navier-Stokes equations are averaged over time, resulting in additional terms representing turbulent stresses. These stresses are then modeled using various turbulence models. Although less accurate, RANS is computationally much cheaper than DNS and LES, making it suitable for industrial applications. For the following discussion, two approaches to model turbulence in the context of RANS are of interest. One approach is based on the so-called Boussinesq hypothesis[11], which assumes that the momentum transfer caused by turbulent eddies can be modeled with an eddy viscosity, thus considering turbulence as an isotropic phenomenon. The so-called two-equations models such as the $k - \epsilon$ and $k - \omega$ models are based on such hypothesis. In contrast, the Reynolds Stress Model (RSM) provides a more detailed representation of turbulence. RSM aims to directly solve transport equations for the Reynolds stresses and the dissipation rate, providing a more detailed representation of turbulence, which is beneficial for

complex geometries and flow conditions. Not relying on the Boussinesq hypothesis, RSM can more accurately capture the effects of turbulence in flows with strong anisotropy, such as swirling flows, secondary flows, and flows with strong separations. Studies in literature have shown that with complex geometries typical of many industrial applications RSM performs better than two equations models (e.g. [75, 82]). When the studied problem includes combustion, studies have shown that RSM leads to better results even in the case of simple geometries (e.g. [41]). Solving more transport equations than the $k - \epsilon$ and $k - \omega$ models makes RSM marginally more computationally expensive.

2.2 Turbulent combustion modeling

The phenomenon of combustion commonly involves hundreds of chemical species and thousands of reactions. The exact amounts depend on the fuel and oxidizer compositions. Considering all possible reactions is not necessary for most applications, as the effect of many reactions on the flow quantities is negligible. There are many strategies to integrate the effects of the chemical reactions into the CFD model. All strategies use a chemical reaction mechanism, which defines an ensemble of species relevant to the studied problem, and the relevant reactions that govern the interactions of such species. In the absence of turbulence, each reaction occurs at a rate that depends on the local concentration of reactants and products, and some rate coefficients. Said rate coefficients are computed via the Arrhenius formula

$$k_r = A \exp \frac{E_a}{RT} \quad (2.1)$$

where A is the Arrhenius constant, E_a is the activation energy of the reaction, R is the gas constant and T is the static temperature. For the reaction between methane (CH_4) and air, which is that of interest for this project, a widely used mechanism is named GRI-MECH 3.0 [104], which is considered to be highly detailed with 53 species and 325 reactions. Besides the main reactions, the GRI-MECH 3.0 mechanism describes also NO_x formation.

The first approach that historically has been used to model turbulent combustion, is to solve a transport equation for each species included in the reaction mechanism. In the case of GRI-MECH 3.0, this means adding 52 equations to the system. As solving such a number of extra equations significantly increases the computational cost of the simulation, this approach is often used with reduced mechanisms. Reduced mechanisms consider a number of species (and thus of added transport equations) in the order of 15 and 20 (e.g. [112, 136]). The main challenge that this approach presents is the modeling of the source term in the species equations. The source term quantifies the chemical production and destruction of each species, which is challenging to model in the context of turbulent combustion. The complexity increases in a turbulent flame because the reaction rates do not depend only on the reactant and product concentration and static temperature, but also on the turbulent behavior of the flame.

One of three main approaches is commonly used to model the source term. The first modeling approach uses the reaction-rate expressions defined by the Arrhenius formula, neglecting the effect of turbulent mixing. This approach leads to extremely poor predictions unless the modeled flame is laminar or the CFD simulation is based on a high-fidelity approach such as direct numerical simulation (DNS), in which case no turbulence modeling is needed.

A second approach, accounting for turbulent mixing, was proposed by Magnussen and Hjertager [6]. Their model is named Eddy-dissipation model (EDM) and it is based on the assumption that chemical time-scales are much smaller than turbulent time-scales (i.e. chemical reactions are much faster than turbulent mixing). In this context, the limiting factor in the reactions is the mixing of fuel and oxidizer, making it possible to assume instantaneous burning upon mixing, thus neglecting the complex chemical kinetics. In this case, instead of the detailed mechanism, only the global reaction is considered. Given the assumptions, simulations carried out with the EDM give no information on intermediate species. The EDM often leads to poor predictions and it is not suited for NO modeling.

The eddy-dissipation model was then improved and generalized by the same Magnussen [66]. The improved model, named Eddy-dissipation-Concept (EDC), allows the inclusion of detailed chemical mechanisms in turbulent flows. It assumes that reactions occur within small turbulent structures, named "fine scales". Reactions proceed over the turbulent time scale, governed by the reaction rates of the finite-rate-kinetics. In the case of EDC, the full detailed mechanism can be taken into account and concentrations of minor species can be computed. The substantial downside of the EDC is the added computational burden for each of the species included in the mechanism.

To avoid the computational burden of solving a differential equation for each of the many species that appear during the reaction of fuel and oxidizer, one possibility is to use the so-called flamelet model approach, which views a turbulent flame as an ensemble of laminar flamelets. The approach was originally proposed by Peters [88], and has been widely investigated and developed over the years (eg., [92, 90, 91, 46]). With this approach, chemistry is simulated in a pre-processing phase solving the so-called flamelet equations, and key quantities are stored in a look-up table, which is then included in the CFD analysis via a set of conserved scalars used as input variables to the look-up table. The term "reactive scalars ϕ " is used in the following discussion for the outputs of the look-up table. These are chemical species mass fractions Y_i , temperature T , mixture density ρ , and reaction rates S .

Among the many flamelet models proposed in the literature, the choice made for this thesis is the so-called Flamelet Generated Manifold (FGM), proposed by Van Oijen et al. [117]. Despite being developed for premixed turbulent flames, FGM has been successfully applied also to diffusion flames (eg., [118, 55]). In this approach, the conserved scalars used to include chemistry in the CFD simulation are mixture fraction Z , and progress variable C . The mixture fraction quantifies the local level of fuel and oxidizer mixing, and its value can vary between 0 (in the oxidizer stream) and 1 (in the fuel stream). The progress variable represents the advancement of the reaction, and equals 0 in the unburnt mixture and 1 in the burnt mixture. In

the FGM approach, all reactive scalars are the outputs of a 4-dimensional look-up table computed before the CFD simulation. The four input variables of the look-up table are Favre-averaged mixture fraction \tilde{Z} , Favre-averaged progress variable \tilde{C} , mixture fraction variance Z_v , and progress variable variance C_v . Over the years, the use of FGM with high-fidelity methods for turbulence analysis, such as Large Eddy Simulation (LES), has been widely investigated in turbulent combustion (eg., [121, 81, 57, 85, 1, 26, 22, 129, 133]). The FGM has been chosen as the chemical model in this thesis for two main reasons: a) in contrast to other flamelet model methods, whose thermo-chemistry tends to equilibrium towards the outlet of the domain, FGM can theoretically predict flame extinction and sub-equilibrium concentrations of reactants and products even toward the outlet of the domain; and b) FGM allows to solve a handful of extra transport equations to compute the concentration of slow evolving species such as NO_x , increasing only marginally the computational cost. Details about the methodology are provided in chapter 3.

2.3 Modeling NO formation in reference turbulent flames

This section presents the main difficulties of modeling NO in turbulent flames, focusing on strategies based on flamelet models. The discussion in this section is based on studies conducted on reference flames. Reference flames are commonly characterized by simple geometry and provide high-quality experimental data, making them crucial for the validation of CFD models and to study of physical phenomena in a well-controlled environment.

The complexity of modeling turbulent flames increases significantly when the formation of nitric oxide (NO) is of interest, since accurately predicting its formation is challenging for several reasons. Its formation rate strongly depends on other reactive scalars, such as temperature [39], which makes the predicted NO concentration highly sensitive to inaccuracies in the computed temperature

field. Non-adiabatic phenomena, such as radiation, which may have small effects on the main reactive scalars, have instead a significant effect on the formation of NO. Therefore, neglecting non-adiabatic phenomena in NO formation modeling leads to significant overpredictions of its mass fraction. Frank et al. [30] carried out experimental and numerical investigations of Sandia flame D [8], a methane-fueled turbulent diffusion flame. Using two different approaches for chemistry, they predicted a radiative heat loss equal to 10.5% and 12.5% of the total heat of combustion, defined as the energy released when the supplied flow rate of fuel burns completely. Accounting for these heat losses, they observed a drop in peak NO mass fraction Y_{NO} of 37% and 57% with respect to the adiabatic flame analysis, obtaining an improved agreement with measured data in both cases. Ihme et al. [46] studied the same test case and adopted the flamelet progress variable (FPV) approach [89, 45] extended to account for radiation. They found that the inclusion of radiation in the model reduced Y_{NO} by approximately 25-30% with respect to the adiabatic case, improving the agreement with the experiments. This is shown in Fig. 2.1 In

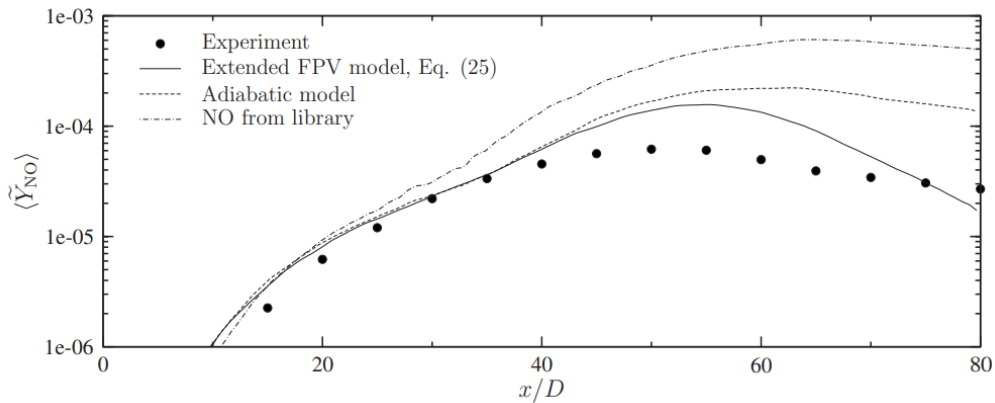


Figure 2.1: Comparison of measured (symbols) and calculated (lines) mean NO mass fraction along the centerline for Sandia flame D. The figure is taken from Ihme et al. [46]

the same study, the authors carried out the same analysis at the outlet section of a Pratt & Whitney aircraft engine combustor. Against a radiation loss-induced 0.4%

reduction in outlet temperature, they reported a reduction in Y_{NO} by 67%, with the non-adiabatic model still overestimating the measured value by 38%.

Another reason that makes the NO concentration challenging to predict is the fact that it is formed at a rate smaller than that of fuel oxidation reactions [46]. This occurrence, combined with the typical short residence times in modern combustion devices, results in NO concentrations being significantly below equilibrium [42]. As the progress variable is commonly defined in a way that can adequately keep track of the main product formation, the concentrations of slowly-forming species, such as NO, are significantly overpredicted when retrieved from the look-up table. Godel et al. [37] performed LES simulations of the jet flame in a vitiated coflow defined in Cabra et al. [14]. They improved the agreement between CFD and measured data by adopting a definition of the progress variable based on both the main products of combustion and NO_x . Pitsch and Steiner [92, 90] used the LES approach to simulate the Sandia flame D with an in-house CFD code, and achieved very good agreement with measured values of Y_{NO} by implementing the Lagrangian flamelet model. This is an approach in which the reactive scalars are determined by solving the unsteady flamelets equations rather than the steady ones.

To account for the different time scales of product formations, Ihme et al. [46] used a scale-separation method. Here the main reaction progress variable is used to track the main reactions, while an extra transport equation for slow-forming NO is solved in a segregated manner. The source term in this equation is obtained via a linear expression whose coefficients are tabulated from steady diffusion flamelet libraries. Vervisch et al. [119] proposed a similar approach where the reaction rate in the Y_{NO} equation is defined as a function of the difference between the instantaneous concentration of NO and its equilibrium value. Pecquery et al. [86] proposed tabulating the NO reaction rate in two ways: once using a canonical progress variable based on main products, and then using a progress variable based on both main products and NO. In the region near the flame front, where the formation of NO is fast, the source term of the segregated equation is taken from

the look-up table computed with the canonical progress variable. In the burnt gases, where the formation of NO is slower, the same source term is taken from the look-up table computed including NO in the progress variable. All the approaches based on a segregated transport equation for NO with tabulated source term show a significant improvement with respect to those tabulating NO concentration. Yadav et al. [130] used the commercial code ANSYS Fluent, which is the same adopted in this study, and modeled the Sandia flame D by combining LES and FGM. They used counterflow diffusion flamelets to tabulate reactive scalars, and solved a segregated equation for Y_{NO} with tabulated source term. Such an approach improved the results obtained by tabulating the value of Y_{NO} , reducing the peak value from $1.5 \cdot 10^{-3}$ to $2.6 \cdot 10^{-4}$, but still overpredicting the measured value of $6.0 \cdot 10^{-5}$.

To include the effect of non-adiabatic phenomena in flamelet models, the common strategy is adding enthalpy as an input variable of the look-up table, leading to a 5-dimensional database in the case of FGM. Following this approach, the memory size requirements for the database increases to tens of Gb, an amount which is hard to handle with standard computer processors without sacrificing the resolution of the flamelets. Wen et al. [124] had to decrease the resolution of their flamelets to increase the dimensionality of their look-up table. Some researchers have proposed the use of artificial neural networks to avoid this problem with 5-dimensional look-up tables [134, 44, 54]. Weise et al. [123] developed a methodology to mitigate the memory issue by converting the look-up table into a set of polynomial functions. Some codes, including ANSYS Fluent, avoid this issue by not considering non-adiabatic effects on species concentration, while still considering them on temperature and fluid properties. This assumption is commonly known as the frozen species assumption and, in most cases, it is a reasonable assumption. The frozen species assumption is often dictated by physical aspects, such as minimal reaction rates close to actively cooled walls in liquid rocket engines (e.g. [48]). However, it commonly leads to inaccuracies when NO formation is of interest.

To conclude this section, it is important to highlight a key observation drawn

from the literature on test flames and NO_x modeling. In the context of test flames, the literature generally shows that key quantities such as temperature are reliably predicted across various modeling approaches. However, the accurate prediction of NO_x concentrations remains significantly more challenging. Although some studies have achieved promising results using LES techniques, these successes often rely on the use of customized, in-house computational codes (e.g. [90, 46]). In contrast, simulations performed with commercial CFD software, which are more accessible and commonly used in industrial settings, tend to yield less accurate predictions of NO_x emissions (e.g. [130, 95]), highlighting a gap between academic advances and practical industrial application.

In this thesis, a commercial CFD code is used to perform a systematic analysis on the Sandia D test flame, assessing how the NO_x modeling approach affects agreement with experimental data. A correction to the NO scalar transport within the FGM framework is also proposed and implemented, resulting in improved accuracy compared to the default model in the commercial solver.

2.4 Analysis of industrial burners flows

This section discusses an overview of fluid dynamic simulations of case studies similar to that of this thesis. First are presented cases where the non-reacting flow in industrial applications characterized by complex geometrical domains is simulated, and then the complexity of chemical reactions and NO_x formation is added.

2.4.1 Cold flow analysis

Most industrial burners are characterized by geometries and flow fields which are far more complex than those of reference laboratory experiments, such as the Sandia Flames [7]. In industrial applications, it is important to optimize and validate the predictive capabilities of the CFD analysis of the cold flow of the system, ie that without chemistry, before including also reactive flow modeling in the simulations.

This is because the levels and patterns of flow turbulence have a strong impact on the predictions of the combustion process [41]. Recently, this approach was adopted by Wronski et al. [127], who analyzed the cold flow field of a magnesium burner performing RANS analyses with the CFD code ANSYS Fluent. To avoid handling simultaneously the uncertainty affecting the analysis of swirling flows in geometrically complex ducts, and that associated with modeling the combustion of the two-phase flow of magnesium and air, they started their investigations by modeling the cold one-phase swirling air flow. The authors compared the results of their simulations with experimental data that they obtained for two operating conditions, characterized by different levels of flow swirl. They tested several variants of the $k - \epsilon$ turbulence model [60] and of the Reynolds Stress Model (RSM) [59]. It was found that, for the low-swirl case, the Renormalization Group $k - \epsilon$ turbulence model [60] performed slightly better than the other variants. In the high swirl case, the RSM variant based on the ω -equation of the standard $k - \omega$ [125] gave the best predictions. In both cases, the shape and position of the zone with negative values of axial velocity in the main duct could be predicted with reasonable accuracy.

Meraner et al. [73] conducted a numerical study of the cold flow in a partially premixed bluff body burner, and compared their computed velocity fields with the Particle Image Velocimetry measurements of Dutka et al. [24]. The authors tested three RANS eddy viscosity turbulence models, namely the standard $k - \epsilon$ model, the realizable $k - \epsilon$ model [100] and the $k - \omega$ Shear Stress Transport (SST) [69]. An overall good agreement with experiments was found, particularly with regard to the size of the flow recirculation region behind the bluff body. However, the predicted magnitude of the axial velocity deviated from the experimental data. The $k - \omega$ SST model performed better than the other two models in capturing the velocity decay in the jet region downstream of the recirculation zone, but worst in terms of predicting the overall velocity level. The agreement between SST-based predictions and experiments improved when the analysis was carried out in unsteady mode. Even larger improvements were observed using LES and a stress-blended eddy

simulation (SBES) [72, 68].

2.4.2 Reacting flow and NO formation analysis

Modeling of NO formation in complex industrial applications is commonly achieved with a simplified approach. The NO formation rate is computed as the sum of the contributions of the mechanisms relevant to the studied problem, which are computed separately. This approach has often been used in combination with RANS approaches for turbulence closure and different chemical models. For instance, Schluckner et al. [13] investigated its accuracy when coupled with different chemistry models. They performed simulations of an industrial jet burner working with natural gas and oxygen using the realizable $k - \epsilon$ model for turbulence closure. Chemistry modeling was achieved via two flamelet-based approaches and two classical species transport models. The flamelet models investigated were the laminar flamelet model (SFM), and the partially-premixed steady diffusion flamelet model (PPSFM). The former model assumes chemistry to be close to equilibrium and it is based solely on mixture fraction, the latter does not make such an assumption and it is based on mixture fraction and progress variable. The investigated species transport models were the eddy dissipation model and eddy dissipation concept. The comparison between measured and computed temperatures showed a generally good agreement between experiments and all numerical models. In particular, the CFD overpredicted the temperature by 2.2% to 7.5% depending on the chemistry model and probe position in the combustion chamber. The PPSFM was the only model to properly predict both the flame shape and the NO emissions. The authors stated that despite leading to overall good NO concentration prediction, the EDM could hardly be considered an adequate solution to the problem as it ignores detailed combustion reaction pathways.

Zhou et al. [40] studied the effects of geometry modification on a swirl heavy fuel oil boiler NO_x emissions. They applied a flamelet model for chemistry, the realizable $k - \epsilon$ model for turbulence closure, and the simplified approach for

NO. This combination resulted in a good agreement between the measured and computed concentration of NO in the flue gases. Rago et al. [32] studied a swirl-stabilized coal burner both experimentally and via CFD. They used a combination of realizable $k - \epsilon$ for turbulence closure, a flamelet-based model for chemistry, and the simplified approach for NO. The comparison between CFD and measured data at the combustion chamber exit location showed good agreement: the CFD overpredicted the gas temperature by 5% and underpredicted the NO concentration by 22%. Lin et al. [64] performed a CFD and experimental analysis on a series of non-premixed double swirl burner configurations changing the blade angles of the external swirler. They used a combination of the realizable $k - \epsilon$ model for turbulence closure and the EDM for modeling chemical reactions. This setup achieved good agreement between CFD and measures. The simulation overpredicted the values of temperature by 3.1% to 6.5% depending on the position in the domain. The concentration of NO at the outlet of the system was overpredicted by the CFD by 2.9% to 7.2% depending on the burner configuration. Nhan et al. [78] numerically investigated the effect of recirculating flue gas on NO formation in a mid-/large-sized combustion system. Turbulence closure was achieved via the realizable $k - \epsilon$ model and chemical reactions were modeled with a modified version of the EDM. The constants in the chemical model were modified to best match the experimental temperature profiles measured in [15] for the same test case. The modification to the EDM improved the agreement between CFD and experiments, but a significant deviation was still observed in some regions of the flame. The numerical results computed at the outlet of the systems without and with flue gas recirculation in the burner showed a reduction in NO by a factor of 8.5 in the latter. A comparison between computed and measured NO concentration at the outlet of the system with recirculating flue gas showed good agreement, with the computed NO emission being about 10ppm against the measured 15ppm.

To conclude this section, it is important to highlight a key observation drawn from the literature on industrial applications concerning NO_x formation modeling.

Studies on NO_x formation in industrial applications typically rely on commercially available CFD codes and tend to focus primarily on the specific application context (e.g. [40, 78]). While some research does explore the sensitivity of results to turbulence and combustion modeling approaches (e.g. [13]), NO_x itself is often treated using simplified models. A detailed and systematic sensitivity analysis of NO_x modeling strategies, especially one validated against test flames, is rarely performed, leaving a gap in understanding how different modeling choices influence NO_x predictions in industrial applications.

The novelty of the work lies in several key contributions: the development and validation of a modeling approach for both cold and reactive flows in an industrial gas burner, the formulation of practical guidelines for simulating complex flow dynamics in such systems, the provision of new experimental data, and valuable insights into the flow physics specific to the industrial burner under investigation. Moreover, a systematic analysis of NO_x modeling strategies is conducted within the context of an industrial application.

Chapter 3

Governing equations

This chapter will present the main governing equations which are of use in this thesis. The first part of this section briefly presents how turbulence is modeled in this thesis. The second part describes the equations governing the chemistry model used herein to describe combustion. Finally, the third part presents the main physical mechanisms governing NO_x formation and describes how this is modeled in the present work.

3.1 CFD method and turbulence modeling

Computational Fluid Dynamics (CFD) applies fluid mechanics using computer simulations to solve fluid flow problems based on the Navier-Stokes equations, which describe the conservation of mass (continuity equation), momentum, and energy. These equations are complex partial differential equations that are difficult to solve analytically, especially for most real-world flows. To address this, CFD employs numerical methods to approximate solutions by discretizing the equations into algebraic forms that can be solved computationally. Common discretization methods include finite difference, finite element, and the widely used finite volume method. This process involves dividing the flow domain into small control volumes (meshing), and solving the equations iteratively for each volume to approximate

fluid behavior. Additionally, temporal discretization divides the time domain into discrete intervals for time-dependent problems. To directly solve Navier-Stokes with such an approach, thus using DNS, is usually computationally expensive due to the presence of turbulence. Turbulence is a complex phenomenon defined by chaotic, unpredictable motion, along with rapid changes in pressure and velocity. It is characterized by swirling eddies and fluctuations in flow variables, occurring across a wide range of length and time scales. As mentioned in Chapter 2, the use of DNS is impracticable for most applications due to its cost. For this reason, a certain degree of turbulence modeling is often used.

3.1.1 Large Eddy Simulation approach

As anticipated in Chapter 2, LES is a strategy that greatly reduces computational cost with respect to DNS. Despite that, it is still considered too burdensome for many applications. In LES, the flow is separated into large and small eddies using a spatial filter. The large eddies are directly computed and the smaller, sub-grid scale (SGS) eddies are approximated using an SGS model. The SGS turbulence model in this thesis employ the Boussinesq hypothesis as RANS. In SGS models, the SGS eddies act as an increased viscosity of the fluid, usually named SGS eddy viscosity (μ_{sgs}). One of the most common SGS models, and that used in the LES simulations of this thesis, is the Smagorinsky-Lilly dynamic subgrid-scale model [103, 34, 63]. Here the value of μ_{sgs} is computed via Eq. 3.1.

$$\mu_{sgs} = \rho L_s^2 |\bar{R}| \quad (3.1)$$

$$|\bar{R}| \equiv \sqrt{2\bar{R}_{ij}\bar{R}_{ij}} \quad (3.2)$$

$$L_s = \min(\kappa_v d, C_s \Delta) \quad (3.3)$$

$$\Delta = V^{1/3} \quad (3.4)$$

where L_s is the mixing length for subgrid scales, \bar{R}_{ij} is the rate-of-strain tensor for the resolved scale, κ_v is the von Kármán constant, Δ is the local grid scale, and

V is the local computational cell volume. C_s is the Smagorinsky constant and it is dynamically calculated using the data from the resolved flow scales.

One can see that μ_{sgs} is computed algebraically and depends on the resolution of the discretization itself. An effective viscosity (μ_{eff}) is then computed as the sum of SGS eddy viscosity and molecular viscosity (μ), which represents the physical viscosity of the fluid:

$$\mu_{eff} = \mu + \mu_{sgs} \quad (3.5)$$

The effective viscosity replaces the molecular viscosity in the Navier-Stokes equations. This allows the equations to account for the enhanced diffusion caused by turbulent eddies, not just molecular diffusion.

3.1.2 Reynolds Averaged Navier-Stokes approach

The use of RANS models significantly reduces the computational cost, reason why they are widely used for many applications.

The Reynolds-averaged turbulence modeling approach necessitates proper modeling of the Reynolds stresses in the momentum equations. A common technique, typical of single-equation or two-equations models, uses the Boussinesq hypothesis, which connects the Reynolds stresses to the mean velocity gradients through turbulent viscosity. Alternatively, the Reynolds Stress Model (RSM) takes a different approach by directly solving transport equations for each term in the Reynolds stress tensor.

3.1.2.1 Two-equations models

Two-equation models are based on the Boussinesq hypothesis, thus modeling turbulence as an increase in the viscosity of the fluid. These models solve two additional transport equations to account for turbulence effects: one for turbulent kinetic energy (κ) and another for either the turbulence dissipation rate (ϵ) or specific dissipation rate (ω). In this thesis the only two equations model used is the κ - ω

Shear Stress Tensor (SST) model, thus the solved transport equation for turbulence are those of κ and ω .

The values of the two turbulent quantities are then used to compute the value of the turbulent viscosity μ_t , which similarly to the LES approach is added to the physical viscosity of the fluid. The value of μ_t is computed algebraically and the exact equation used to do so depends on the RANS model applied. For the κ - ω SST model, the turbulent viscosity is computed as:

$$\mu_t = \frac{a_1 \rho \kappa}{\max\left(\frac{a_1 \omega}{\alpha^*}, R F_2\right)} \quad (3.6)$$

where $a_1=0.31$ is a constant, α^* is a damping coefficient used for low-Reynolds correction, and F_2 is a blending function.

3.1.2.2 Reynolds stress model

The Reynolds stress model solves an additional transport equation for each component of the Reynolds stress tensor together with an extra equation for ϵ or ω . The individual Reynolds stresses $\tau_{i,j}$ are then used to obtain closure of the Reynolds-averaged Navier-Stokes equations avoiding the use of the Boussinesq approximation and thus providing a more detailed representation of turbulence. The computational cost of this model is higher than the two-equations model, as 5 extra equations are solved in 2D applications and 7 extra equations in 3D applications for turbulence closure.

3.2 FGM method

This section presents the main equations used within the FGM method, the model used in this thesis to describe combustion. It also explains how chemistry is tabulated and included in the CFD simulation when using the FGM model. First, the procedure to compute and store chemistry in the adiabatic case is presented. Then, the non-adiabatic extension to the model is explained. Finally, it is shown

how the tabulated values are included in the CFD simulation and how the scale-separation methodology is implemented. Further model detail and the numerical method for solving the FGM equations in the FLUENT code used in this research are provided in [4].

3.2.1 Adiabatic look-up table

To generate a look-up table, the Favre-averaged values of all reactive scalars ($\tilde{\phi}$) are defined as a function of the Favre-averaged mean values and variances of two parameters: Z and C .

The first step to generate a look-up table is to compute a series of flamelets based on a kinetic reaction mechanism. In this work, diffusion flamelets are obtained using FLUENT by solving laminar counterflow diffusion flame equations in the Z space. The parameter Z is defined by Eq. (3.7):

$$Z = \frac{Y_j - Y_{j,ox}}{Y_{j,f} - Y_{j,ox}} \quad (3.7)$$

where Y_j is the local elemental mass fraction of the j^{th} element, $Y_{j,ox}$ is its value in the oxidizer stream, and $Y_{j,f}$ is its value in the fuel stream. Under the assumption of equal diffusivity for all species, the value of Z is the same for all elements. The system of laminar counterflow diffusion flame equations consists of Eq. (3.8), which is solved for every species in the reaction mechanism, and Eq. (3.9), which is solved for temperature.

$$\rho \frac{\partial Y_i}{\partial t} = \frac{1}{2} \rho \chi \frac{\partial^2 Y_i}{\partial Z^2} + S_i \quad (3.8)$$

$$\rho \frac{\partial T}{\partial t} = \frac{1}{2} \rho \chi \frac{\partial^2 T}{\partial Z^2} - \frac{1}{c_p} \sum_i h_i S_i + \frac{1}{2c_p} \rho \chi \left[\frac{\partial c_p}{\partial Z} + \sum_i c_{p,i} \frac{\partial Y_i}{\partial Z} \right] \frac{\partial T}{\partial Z} \quad (3.9)$$

In Equations (3.8) and (3.9) the subscript i refers to the i^{th} species, Y_i is its mass fraction, the term h is the specific enthalpy per unit mass, and S is the reaction rate. The symbol χ represents the scalar dissipation rate and must be modeled across the flamelet ($\chi = \chi(Z)$). Introducing a dimensionless function $\Phi = \Phi(Z, \rho)$ [56], one

can define:

$$\chi(Z) = \chi_{st} \frac{\Phi(Z, \rho)}{\Phi(Z_{st}, \rho_{st})} \quad (3.10)$$

In Eq. (3.10) the subscript st denotes the stoichiometric condition, and the stoichiometric scalar dissipation rate χ_{st} is a user-given input that quantifies the departure from the equilibrium condition of the flamelet. Equations (3.8) and (3.9) are solved for several values of χ_{st} , starting from a minimum value of $\chi_{st} = 0.01s^{-1}$ and gradually increasing it up to the value of χ_{st} for which the flamelet is extinguished. A series of steady diffusion laminar flamelets are obtained: $\phi = \phi(Z, \chi_{st})$.

The second step to generate a look-up table is to express the flamelets in the progress variable space. The parameter C is defined in Eq. (3.11):

$$C = \frac{\sum_i \alpha_i (Y_i - Y_i^u)}{\sum_i \alpha_i (Y_i^{eq} - Y_i^u)} = \frac{Y_c}{Y_c^{eq}} \quad (3.11)$$

where the superscript u denotes the unburnt mixture, and the superscript eq the quantity computed with the lowest value of χ_{st} available. The term α_i is a constant equal to 0 for all species except for three products, for which it has a value of 1: carbon dioxide (CO_2), carbon monoxide (CO) and water vapor (H_2O). The next step to generate the look-up table is to change the two independent variables defining the reactive scalars: from mixture fraction and stoichiometric scalar dissipation rate ($\phi = \phi(Z, \chi_{st})$), to mixture fraction and progress variable ($\phi = \phi(Z, C)$). Flamelets are converted in progress variable space for C that goes from 1 down to its extinction value C_{ext} . From there, the time history of the last computed flamelet is used to obtain unstable flamelets and complete the manifold down to $C = 0$.

To complete the look-up table it is necessary to account for the effect of Z and C fluctuations due to turbulence. This is accomplished by using a joint probability density function (PDF) $P(Z, C)$ to calculate the mean value $\tilde{\phi}$ of the reactive scalars, that is:

$$\tilde{\phi} = \int_0^1 \int_0^1 \phi(Z, C) P(Z, C) dZ dC = \tilde{\phi}(\tilde{Z}, \tilde{C}, Z_v, C_v) \quad (3.12)$$

The term $P(C, Z)$ in Eq. (3.12) is the joint PDF of Z and C , assumed to result from the product of two beta distribution [74]. This is a probability distribution that depends on two parameters determined univocally by mean and variance. Thus, the mean value of the reactive scalars depends on the four parameters $\tilde{Z}, \tilde{C}, Z_v$, and C_v . To avoid an increased computational cost of the CFD simulation, the integrals of Eq. (3.12) in the 4-dimensional $(\tilde{Z}, \tilde{C}, Z_v, C_v)$ space are computed beforehand.

3.2.2 Non-adiabatic extension

As mentioned in Chapter 2, a look-up table with more than four dimensions can be hard to handle due to large increases of the required processor memory [124, 44, 54]. Here is presented the approach proposed by Müller et al. [76] to avoid this issue when studying turbulent flames with adiabatic flamelet methods.

A transport equation is solved for the total enthalpy per unit mass H . The fluctuations of H due to turbulence are neglected and only the Favre-averaged value \tilde{H} is considered. Mixture properties, such as temperature and density, are computed accounting for the dependence on \tilde{H} and neglecting that on the turbulent fluctuations of C :

$$\tilde{\phi} = \int_0^1 \phi(Z, \tilde{C}, \tilde{H}) P(Z) dZ = \tilde{\phi}(\tilde{Z}, \tilde{C}, Z_v, \tilde{H}) \quad (3.13)$$

where the term $\phi(Z, \tilde{C}, \tilde{H})$ in Eq. (3.13) is computed with Equations (3.14) and (3.15), which are solved to find the extreme of integration \tilde{T} .

$$\tilde{H} = \sum_i \tilde{Y}_i H_i \quad (3.14)$$

$$H_i = h_i^0(T_{ref,i}) + \int_{T_{ref,i}}^{\tilde{T}} c_{p,i} dT \quad (3.15)$$

$h_i^0(T_{ref,i})$ in Eq. (3.15) is the formation enthalpy of species i at reference temperature $T_{ref,i}$. Species mass fractions and reaction rates are computed adiabatically with Eq. (3.12), and the effect that \tilde{H} has on them is neglected.

The approach proposed by Müller gives satisfactory results in many applications, but not in predicting the formation of NO. As discussed in Chapter 2, NO formation is highly sensitive to temperature: the mass fraction and formation rate of NO computed neglecting the effect of \tilde{H} will grossly overestimate the real values.

3.2.3 CFD simulation and look-up table coupling

All input variables to the look-up table must be computed to include the reactive scalars in the CFD simulation. In the case of RANS-based turbulence modeling, a transport equation is solved for each of the five conserved scalars which serve as input to the look-up table: \tilde{Z} , \tilde{C} , \tilde{Z}_v , \tilde{C}_v , and \tilde{h} . When a LES approach is used to handle flow turbulence, the quantities \tilde{Z}_v and \tilde{C}_v are computed algebraically to account for their subgrid-scale variance from the spatial gradients of the mean \tilde{Z} and \tilde{C} and the turbulent length scale. The added transport equations are coupled with the momentum, continuity, and turbulence closure equations, coupling thus the effects of chemical reactions with flow field and turbulence.

To improve the accuracy of slow-evolving species, a scalar transport equation for each species of interest (φ) can be solved. These equations are solved in a segregated manner, and do not affect the flow field, making this approach well suited only for minor species such as NO. These scalar transport equations have the form:

$$\frac{\partial(\rho\tilde{\varphi})}{\partial t} + \nabla \cdot (\rho\tilde{v}\tilde{\varphi}) = \nabla \cdot \left(\left(\frac{k_t}{c_p} + \frac{\mu_t}{Sc_t} \right) \nabla\tilde{\varphi} \right) + \bar{\rho}\bar{S}_\varphi \quad (3.16)$$

where the term k_t is the thermal conductivity, μ_t is the turbulent viscosity, and Sc_t is the Prandtl number, a dimensionless number defined as the momentum and thermal diffusivity ratio. The source term \bar{S}_φ is given by:

$$\bar{S}_\varphi = \bar{S}_{\varphi, fwd} - \bar{S}_{\varphi, rev} \frac{\tilde{\varphi}}{\tilde{\varphi}_{PDF}} \quad (3.17)$$

The terms $\bar{S}_{\varphi, fwd}$ and $\bar{S}_{\varphi, rev}$ denote the forward and reverse reaction rates of species φ , and are obtained from the look-up table. The term $\tilde{\varphi}_{PDF}$ indicates the concentration of $\tilde{\varphi}$ obtained from the look-up table. In this work, the transported scalar approach has been applied only for NO and NO₂.

3.3 NO_x formation and modeling

The first part of this section presents the main mechanisms (or paths) of NO formation in hydrocarbon flames. These are thermal, prompt, and via intermediate nitrous oxide N₂O. As mentioned in Chapter 1, comments on NO_x formation in hydrogen flames are made, as they are considered valuable in the general context of this thesis. All approaches adopted herein for NO_x modeling are described and discussed in the second part of the section.

3.3.1 NO_x formation

3.3.1.1 Thermal NO

Thermal NO is formed when nitrogen molecules N₂ break due to the high temperatures reached during combustion. Nitrogen atoms N quickly react with oxygen forming NO molecules. In most applications, the thermal path is the main contributor to NO formation.

The accepted mechanism governing thermal NO formation is that proposed by Zeldovich [132]. Activation of the thermal path requires high temperatures, typically above 1800 K [67], due to the high energy required to break the N₂ triple bond. The activation energy needed for the oxidation of N atoms is low compared to that needed for breaking the N₂ molecule, which leads to the consumption rate of N atoms being close to that of its formation. A quasi-steady state assumption for atomic nitrogen concentration [N] can be made, which leads to the formation rate of thermal NO to be:

$$\Omega_{th} := \frac{d[NO]_{th}}{dt} = 2k_{f,1}[O][N_2] \frac{\left(1 - \frac{k_{r,1}k_{r,2}[NO]^2}{k_{f,1}[N_2]k_{f,2}[O_2]}\right)}{\left(1 + \frac{k_{r,1}[NO]}{k_{f,2}[O_2] + k_{f,3}[OH]}\right)} \quad (3.18)$$

as demonstrated in [43]. The subscript *th* in Eq. (3.16) indicates the thermal mechanism. The coefficients $k_{f,x}$ and $k_{r,x}$ are the forward and reverse rates of reaction x and are defined as Arrhenius rates by Eq. (3.19):

$$k_r = AT^n e^{-\frac{E}{T}} \quad (3.19)$$

where the rate constants A , n , and B are obtained from the work of Hanson et al. [39].

Hydrogen flames burn generally hotter than hydrocarbon flames. For instance, the adiabatic flame temperature of a stoichiometric hydrogen-air mixture at ambient condition is close to 2500 K. A stoichiometric mixture of methane and air in the same condition has an adiabatic flame temperature just above 2200 K. For this reason, thermal NO_x formation can be significant in hydrogen flames.

3.3.1.2 Prompt NO

Prompt NO forms in the region of fast-rate chemistry near the flame front, where nitrogen interacts with carbon in a chain of reactions that leads to the formation of NO. The prompt path can lead to a significant amount of NO in fuel-rich regions even at moderate temperatures [67, 36].

The model to compute the prompt contribution to the overall NO formation rate proposed by De Soete [20] and modified by Dupont [23] is often used in combustion analyses [13, 40, 32, 64, 78, 80, 29]). In this model, the prompt NO formation rate is defined as:

$$\Omega_{pr} := \frac{d[NO]_{pr}}{dt} = f k'_{pr} [O_2]^a [N_2] [fuel] e^{-\frac{E'_a}{RT}} \quad (3.20)$$

where the subscript pr denotes the prompt path. The symbols R and E'_a denote, respectively, the gas constant and the activation energy of the reaction, equal to 303474.125 J/mol. The variable f is a function of the number of carbon atoms in the fuel molecule and the overall equivalence ratio Φ of the system. The equivalence ratio is a parameter that depends on the ratio of fuel and air mass flow rates and their ratio in the stoichiometric case. The empirical correlation linking f to the aforementioned parameters is reported in [23]. The variable k'_{pr} is defined as:

$$k'_{pr} = 6.4 \cdot 10^6 \left(\frac{RT}{p} \right)^{a+1} \quad (3.21)$$

where p denotes the static pressure. The symbol a in Equations (3.20) and (3.21) is the so-called oxygen reaction order, which depends on \tilde{X}_{O_2} , the mole fraction of O_2 .

According to De Soete [20] the value of a can be defined as:

$$a = \begin{cases} 1, & \tilde{X}_{O_2} < 4.1 \cdot 10^{-3} \\ -3.95 - 0.9 \ln(\tilde{X}_{O_2}), & 4.1 \cdot 10^{-3} \leq \tilde{X}_{O_2} \leq 1.11 \cdot 10^{-2} \\ -0.35 - 0.1 \ln(X_{O_2}), & 1.11 \cdot 10^{-2} < \tilde{X}_{O_2} < 0.03 \\ 0, & \tilde{X}_{O_2} \geq 0.03 \end{cases} \quad (3.22)$$

Since hydrogen combustion lacks hydrocarbon radicals, prompt NO_x formation is minimal or negligible in pure H_2 flames.

3.3.1.3 N_2O -intermediate NO

Under suitable conditions, NO can be formed via the so-called N_2O -intermediate path. The weight of the N_2O -intermediate path becomes more significant in high-pressure lean conditions [79]; in most cases, however, its contribution to NO formation is considerably smaller than that of the thermal path.

The first mechanism of NO formation via nitrous oxide intermediate was proposed by Malte et al. [84], and is composed of two reactions:



where M is a generic third body. The molar concentration of nitrous oxide $[\text{N}_2\text{O}]$ is often computed assuming a quasi-steady state ($d(\text{N}_2\text{O})/dt=0$), as done in this study. Under these assumptions, the formation rate of NO via the N_2O path is:

$$\Omega_{\text{N}_2\text{O}} := \frac{d[\text{NO}]_{\text{N}_2\text{O}}}{dt} = 2(k_{f,4}[\text{N}_2\text{O}][\text{O}] - k_{r,4}[\text{NO}]^2) \quad (3.25)$$

where $k_{f,4}$ and $k_{r,4}$ are the forward and reverse rate of reaction (3.24).

3.3.2 NO_x modeling methodologies

In this section are described the methodologies applied in this study for NO_x modeling. All methods are based on solving a segregated transport equation in the form of Eq. (3.16) for NO_2 or NO mass fractions.

Nitrogen dioxide NO_2 is typically formed via the oxidation of NO [120]. In most applications its concentration is lower than that of NO , thus many CFD-based studies neglect its modeling (e.g., [13, 40]). In this study, the approach described in Sec. 3.2 is used for NO_2 . A transport equation in the form of Eq. (3.16) is solved for Favre-averaged NO_2 mass fraction \tilde{Y}_{NO_2} , and the source term of such equation is computed neglecting non-adiabatic effects with Eq. (3.17).

Three alternative methods are used to model NO formation. Each method differs from the others in how the source term of the NO mass fraction transport equation is computed.

The first method, labeled M1, is the scalar transport with the FGM closure method described in Sec. 3.2. The source term $\bar{S}_{Y_{NO}}$ in the \tilde{Y}_{NO} equation is computed with Eq. (3.16) for NO . Thus, the source term becomes:

$$\bar{S}_{Y_{NO},M1} = \bar{S}_{Y_{NO},fwd} - \bar{S}_{Y_{NO},rev} \frac{\tilde{Y}_{NO}}{\tilde{Y}_{NO,PDF}} \quad (3.26)$$

Differently from the sum of contributions approach, this method takes into account the detailed chemistry used for generating the look-up table. On the other hand, method M1 neglects the effects of non-adiabatic phenomena such as heat transfer by radiation. Due to the high sensitivity of NO formation to even small variations in temperature, these phenomena can have a significant effect on NO formation. Neglecting them may result in an overprediction of NO concentration [46, 30].

The second method, labeled M2, is a modified version of M1. Method M2 is similar to the approach of Trisjono et al. [115], who applied a similar idea to source terms and flow properties such as density and viscosity. The source term of Eq. (3.26) is modified as follows:

$$\bar{S}_{Y_{NO},M2} = \eta_c \bar{S}_{Y_{NO},M1} \quad (3.27)$$

The parameter η_c is a locally defined variable aiming to make the source term $\bar{S}_{Y_{NO},M2}$ take into account non-adiabatic phenomena. The value of η_c represents the ratio between the NO formation rate computed including and neglecting non-adiabatic phenomena. Method M2 evaluates the correction factor η_c via physical

considerations and the NO formation mechanisms proposed by Zeldovich [132] and Dupont [23]. It is assumed that in the burnt gases, a flame region where reactions are slower and temperature is high, NO formation is dominated by the thermal path. By contrast, the effect of other mechanisms is neglected in the evaluation of η_c , as they are assumed to be less significant. Near the flame front, a flame region characterized by fast reactions, the prompt mechanism is assumed to dominate NO formation. The Heaviside step function H_e applied on the value of the Favre-averaged progress variable is used to distinguish between the two regions. Similar approaches have been successfully used in literature for distinguishing between the burnt gases and flame front regions in the context of NO formation modeling [86, 109]. With these assumption, the correction factor η_c can be defined as:

$$\eta_c = H_e(C_{step} - \tilde{C})\eta_{c,pr} + H(\tilde{C} - C_{step})\eta_{c,th} \quad (3.28)$$

where C_{step} is a threshold value for the progress variable, set to 0.9 in this study. The choice of this value for the parameter C_{step} is made because when 90% of the reaction is completed, i.e. $\tilde{C}=0.9$, the temperature of the mixture close to stoichiometry rises above 1800 K. The formation of NO via the thermal path is usually predominant at high temperatures and drastically decreases at lower temperatures [67].

The value of $\eta_{c,th}$, representing the ratio of adiabatic and non-adiabatic formation rate of NO via the thermal path, is computed with the Zeldovich mechanism as the ratio:

$$\eta_{c,th} := \frac{\Omega_{th,nad}}{\Omega_{th,ad}} \quad (3.29)$$

where the values of $\Omega_{th,nad}$ and $\Omega_{th,ad}$ are obtained with Eq. (3.18) using the non-adiabatic temperature T_{nad} and adiabatic temperature T_{ad} , respectively. The value of T_{nad} is read from the look-up table, and that of T_{ad} is computed as follows:

$$T_{ad} = T_{nad} + \frac{\Delta\tilde{h}}{c_p} \quad (3.30)$$

$$\Delta\tilde{h} = \tilde{h}_{ad} - \tilde{h} \quad (3.31)$$

The adiabatic total enthalpy \tilde{h}_{ad} is retrieved from the look-up table as it depends only on the level of mixing \tilde{Z} of fuel and oxidizer. The specific heat is retrieved from the look-up table.

The molar concentrations $[N_2]$, $[O_2]$ and $[OH]$ are assumed to be unaffected by non-adiabatic phenomena, whereas the dependence of atomic oxygen molar concentration $[O]$ on temperature is modeled with the partial equilibrium approach [49].

The value of the parameter $\eta_{c,pr}$, representing the ratio of adiabatic and non-adiabatic formation rate of NO via the prompt path is given by the ratio:

$$\eta_{c,pr} := \frac{\Omega_{pr,nad}}{\Omega_{pr,ad}} \quad (3.32)$$

where the values of $\Omega_{pr,nad}$ and Ω_{pr} are obtained from Eq. (3.20) using T_{nad} and T_{ad} , respectively. The molar concentrations $[N_2]$, $[O_2]$, and $[\text{fuel}]$ are assumed to be unaffected by non-adiabatic phenomena.

The advantage of method M2 is that it considers complex reaction mechanisms while accounting for non-adiabatic effects, unlike method M1. The advantage of method M2 over the more common strategy of adding enthalpy to the set of input variables of the look-up table, an action leading to a 5-dimensional FGM database, is that the burden on the computer memory is significantly reduced. In this study, method M2 was implemented via a user-defined function (UDF) in Fluent.

The third method, labeled M3, is the sum of contributions approach. The total NO formation rate is computed with Eq. (3.33), and it is the sum of the formation rates of the three NO paths described in Sec. 3.3.1.

$$\Omega_{tot} = \Omega_{th} + \Omega_{pr} + \Omega_{N_2O} \quad (3.33)$$

The molar concentration of atomic oxygen $[O]$, needed to compute Ω_{th} and Ω_{N_2O} , is calculated via two methods. The first method, labeled 'Part. Eq. $[O]$ ', assumes partial equilibrium for $[O]$ [49]. The second method, labeled 'Tab. $[O]$ ', consists of retrieving the value of $[O]$ stored in the look-up table. The concentration of the OH molecule $[OH]$, needed to compute Ω_{th} , is always retrieved from the look-up table.

To compute the source term in the \tilde{Y}_{NO} equations, one must account for turbulence-chemistry interactions. The effect of turbulence on the NO formation rate is taken into account assuming a beta probability distribution $P(T)$ [74] for the instantaneous temperature around its mean value. The beta probability distribution depends on two parameters uniquely defined by mean and variance. While the mean temperature is obtained from the look-up table, an additional transport equation is solved for the temperature variance. The value of the source term in the \tilde{Y}_{NO} equation is computed as in Eq. (3.34).

$$\bar{S}_{Y_{NO},M3} = \int_{T_{min}}^{T_{max}} M_{w,NO} \Omega_{tot} P(T) dT \quad (3.34)$$

where the term $M_{w,NO}$ is the molar mass of NO, T_{min} is the minimum temperature in the CFD solution, and T_{max} is set to 2300 K.

Chapter 4

Combustion analysis of academic test case

Given the complexity of modeling problems with both turbulence and combustion, as discussed in Chapter 2, a validation test case characterized by a simple geometric domain is first considered. Here one can study the interaction between turbulence and chemistry avoiding the added complexity given by industrial burners' complex geometry. This chapter presents the numerical set-up and the analysis of the validation test case Sandia flame D.

The outline of the chapter is as follows. Section 4.1 presents the test case selected for this study: Sandia flame D. Section 4.2 describes the CFD code, and the methodology, defines the physical domain, grids, and boundary conditions (BCs). Section 4.3 presents the results of this study: first, the discussion focuses on a comparison between CFD models and measured data for the main flow quantities; then the discussion moves toward the comparison in terms of NO predictions. Finally, Section 4.4 provides a summary of the chapter.

This chapter is an adapted version of a part of the work in Ortolani et al.[83].

4.1 Test case

The case selected to validate the methodology is the methane/air turbulent jet flame Sandia D [7], a picture of which is shown in Fig.4.1.



Figure 4.1: Picture of Sandia flame D taken from [7].

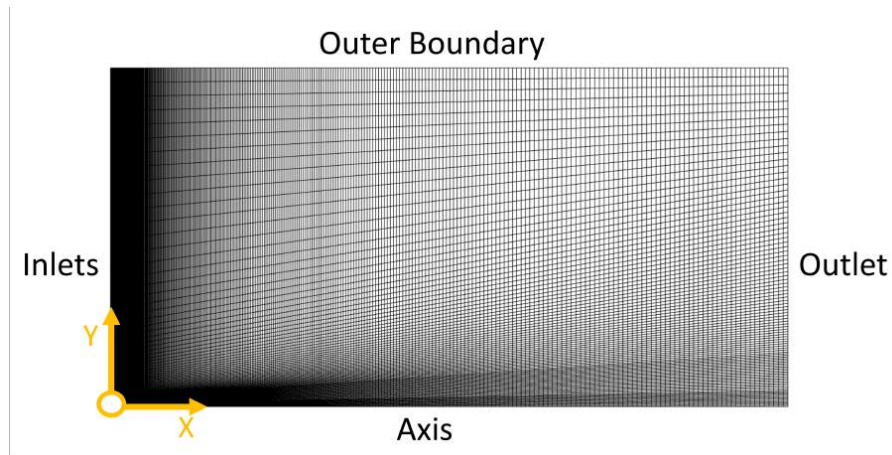
A fuel jet flowing at 49.6 m/s, composed of 75% air and 25% CH₄ by volume, supplies the flame via a nozzle with a diameter of $d=7.2$ mm. Given the fuel composition, the value of the stoichiometric mixture fraction is $Z_{st}=0.351$. Since the methane concentration in the jet is above its high flammability limit, most studies consider this flame to be non-premixed [90, 46, 129]. The fuel jet is surrounded by a

pilot flame. This is a premixed lean flame with equivalence ratio $\Phi=0.77$, supplied by a coaxial nozzle with inner diameter of $d_{p-in}=7.7$ mm and outer diameter of $d_{p-out}=18.2$ mm. The pilot flame provides a power of approximately 6% that of the main flame. Fuel jet and pilot flame are surrounded by a coaxial flow of air, flowing at 0.9 m/s. Laser-induced fluorescence/Raman/Rayleigh spectroscopy was used at the Sandia National Laboratory to measure temperature and species mass fractions [8]. Measurements of the velocity field were carried out with laser Doppler velocimetry (LDV) at the University of Darmstadt [96].

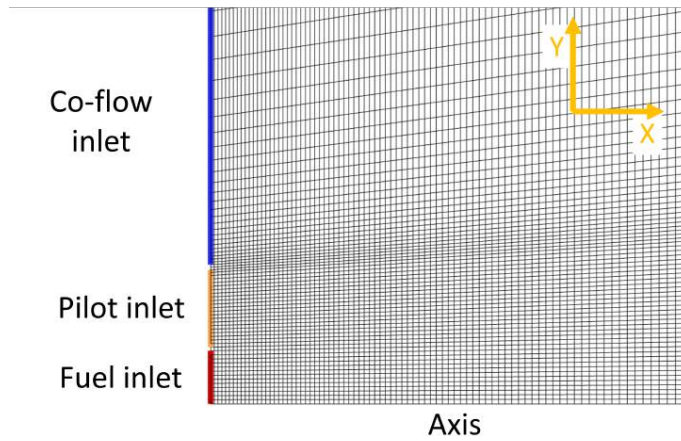
4.2 Methodology

Simulations of the Sandia flame D are performed on both a 3-dimensional physical domain and a 2-dimensional physical domain used with an axisymmetric approach. All simulations are carried out using the commercial code ANSYS Fluent V21R2 [4]. All grids are generated with ICEM CFD V21R2 [3]. Figure 4.2a shows a 2D grid and the frame of reference. The 2D domain starts at the exit of the nozzles, which coincides with the inlet boundaries of the physical domain, and extends axially (x direction) for 100 d and radially (y direction) for 50 d. Three 2D grids with different levels of refinement are generated: a coarse, medium, and fine grid. Figure 4.2a shows the overall view of the 2D grid with medium refinement and the origin of the frame of reference. The structured grid with medium refinement has 28623 cells. There are 329 cells in the axial direction and 87 cells in the radial direction. The finest refinement is used close to the nozzle exit (Fig. 4.2b), and the cell size increases both axially and radially. The coarse and fine grids are obtained from the medium grid, respectively reducing and increasing the number of cells in each direction by a factor 1.3. The differences between the results obtained with the three grids are found to be negligible, thus only the results of the medium grid are reported herein.

Figure 4.3a depicts the physical domain of the 3D simulations. This consists of



(a) overall view of the grid.

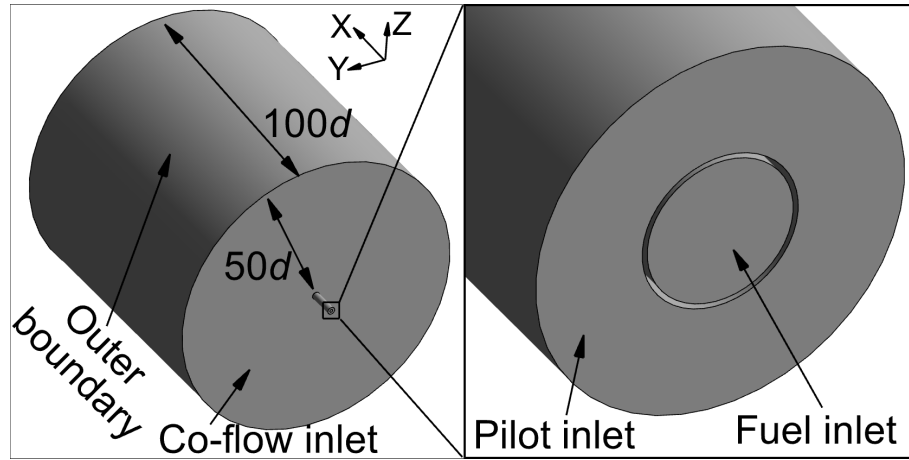


(b) view of the grid close to the nozzle's exit.

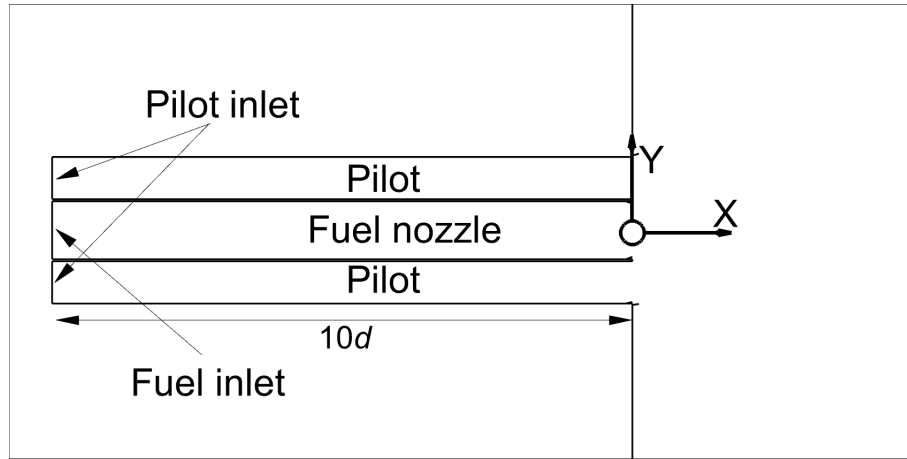
Figure 4.2: 2D Computational grid.

a large cylinder that extends from the exit of the fuel and pilot flame nozzles for $100d$ axially and $50d$ radially (left), and a small cylindrical region occupied by the fuel and pilot flame nozzles (right). A schematic of the latter region is reported in Fig. 4.3b, which shows that the fuel and pilot flame nozzles extend for $10d$ before connecting to the large cylinder. Figure 4.3b also reports the origin of the frame of reference.

The coarse 3D grid, shown in Fig. 4.4, is a hybrid structured/unstructured multi-block mesh. A butterfly mesh topology of the blocks around the axis of the domain



(a) Main dimensions and outer boundaries of the physical domain.



(b) Schematic of the nozzles in the physical domain.

Figure 4.3: Physical domain.

is used to build a structured grid close to the centerline (central region of Fig. 4.4a). Such blocks are surrounded by a region of unstructured tetrahedral elements visible in Figures 4.4a and 4.4b, which allow the transition to a coarser refinement. Finally, the outer region of the mesh is again characterized by a structured axisymmetric topology. The use of unstructured grids allows keeping the cell count significantly lower than that of an entirely structured grid. The structured blocks close to the axis of the domain composing the butterfly mesh are divided into 200 elements in the axial direction, refined close to the nozzles exit, and 44 in the tangential direction. In the radial direction, the fuel nozzle area has 17 cells, and the pilot nozzle area

has 14 cells. The outer structured blocks have 40 cells in both axial and tangential directions. This meshing strategy yields a total cell count to $6.1 \cdot 10^5$. A fine grid is obtained by refining the coarse mesh by a factor of 1.3 in all directions, reaching a cell count of $1.41 \cdot 10^6$. The fine grid is used to investigate the sensitivity of the results to an increased amount of resolved turbulent scales.

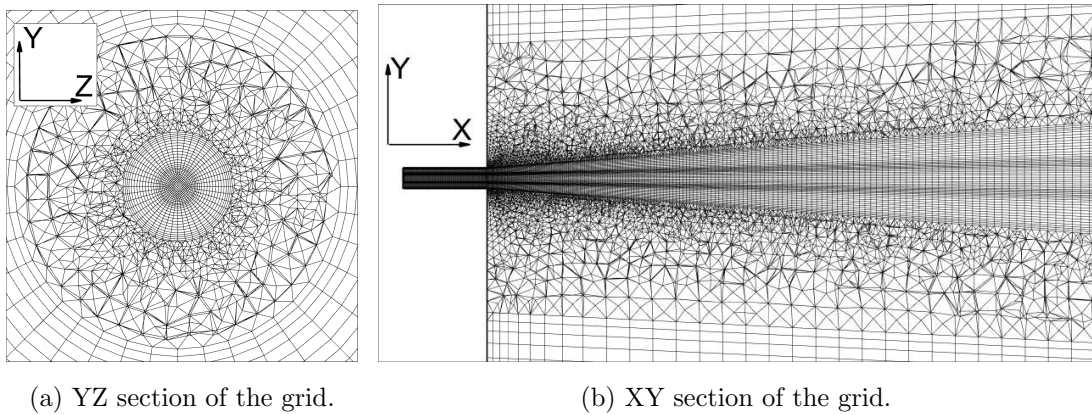


Figure 4.4: Computational grid.

In this study, turbulence is included in the Sandia flame D simulations using either the RANS and or the LES approaches. The 3D meshes are used for the LES simulations. The Smagorinsky-Lilly dynamic subgrid-scale (SGS) model [103, 34, 63] is used for the unresolved turbulence scales. The RANS simulations are performed with the 2D meshes in a steady fashion. The adopted turbulence model is the Reynolds Stress Model (RSM) [59] with the baseline equation for specific turbulent dissipation rate ω by Menter [70]. In 2D, the RSM approach requires solving a transport equation for four distinct components of the Reynolds stress tensor τ_{ij} . The choice of this turbulence model is motivated by three factors: a) literature shows that RSM models yield better agreement of numerical results and experimental data for the Sandia flame D than 2-equation eddy viscosity models [41]; b) as will be better presented in Chapter 5, the RSM model with baseline ω equation has shown to be the best trade-off of numerical stability and solution accuracy when modeling the cold flow of the industrial burner under consideration in this thesis [82]; and

c) in contrast with 2-equation turbulence models, RSM allows modeling turbulence anisotropy and thus obtaining improved predictions in complex problems such as those with significant swirl levels [75, 127, 28]. This is an important factor for burner design optimization, as the swirl intensity in burners has been shown to significantly affect and potentially reduce the formation of NO_x [64].

The FGM model is used for combustion chemistry in all simulations herein. The chemical mechanism used to solve the counterflow diffusion flamelet equations is the well-validated GRI-Mech 3.0 kinetic mechanism [104], which is composed of 53 species and 325 reactions. Fresh air humidity is included in the computation of the flamelets, as many studies show that this parameter has a non-negligible effect on the formation of NO_x [87]. The local molecular viscosity of the mixture is computed with Sutherland's law for air [113]. The thermal conductivity of the mixture is calculated with the formula for air by Stephan et al. [110].

Radiation is taken into account with the P-1 model [16, 101], whereby an additional transport equation for the incident radiation is solved. The radiation model is extended to take into account the turbulence-radiation interaction (TRI). Many studies have shown that TRI is often non-negligible in turbulent combustion applications [114, 137, 33], particularly when considering NO formation [128]. The computation of the extra radiation heat due to TRI is implemented via a UDF following the guidelines of [128], and its contribution is added to the source term of the energy equation. The mixture absorption coefficient κ_a is a crucial property in the evaluation of radiation heat transfer. In this study, the value of κ_a is computed with the Weighted Sum of Gray Gases Model (WSGGM) [25, 105], which is a mid-fidelity method between expensive models that take all absorption bands into account and the cheaper but less accurate gray gas assumption. The WSGGM model computes the absorption coefficient as a function of temperature, partial pressures of H_2O and CO_2 , and the mean beam length s . The value of s must be defined prior to the simulation. It is commonly computed following the guidelines of [101], thus using the volume and surface area of the physical domain. Since the Sandia flame D is an

open flame, the extension of the physical domain is unrelated to the test rig, and computing the value of the mean beam length following the guidelines of [101] would lead to unrealistic values of s . To avoid this issue the mean beam length for the Sandia flame D has been tuned so that the total radiated heat transfer computed with preliminary RANS simulations matched the experimental value observed by Frank et al. [30].

Table 4.1 summarizes the conditions prescribed at the inlet boundaries for the RANS and LES simulations. As the physical domain of the RANS simulations starts at the exit of the fuel nozzle, pilot, and co-flow, the profiles of the Reynolds-averaged axial velocity \bar{V}_x and Reynolds stress components $\bar{\tau}_{ij}$ measured by Schneider et al. [96] are prescribed on all inlets. The components normal to the inlet boundaries of the Reynolds-averaged velocity are set to 0. The inlet profile of the specific dissipation rate ω is computed with the equations suggested in [5]. The profile of ω is estimated from the measured profile of turbulent kinetic energy k and the hydraulic diameters. The hydraulic diameter of the vertical wind tunnel that surrounds the nozzles is used to compute the profile of ω in the fresh air co-flow. The measured velocity profile is prescribed on the co-flow inlet boundary also for the LES simulations. Since part of the fuel nozzle and pilot are included in the LES physical domain, the velocity prescribed at the fuel and pilot inlets is the bulk velocity; turbulent fluctuations are neglected. The value of \tilde{C} on the pilot flame inlet boundary is imposed so that the adiabatic temperature on the boundary is close to the measured 1880 K. In the LES simulation a UDF is used for zeroing the source term of the Favre-averaged progress variable equation from the pilot inlet to the pilot exit. This is done to prevent chemical reactions in the pilot and makes sure that the temperature at the pilot exit equals that measured. The last line of the table refers to the NO mass fraction boundary conditions for all the methodologies described in Sec. 3.3(M1, M2, and M3). Similarly to the Favre-averaged progress variable equation, NO formation in the LES simulations is frozen in the pilot for methodologies M1 and M2. This is achieved within the same UDF used for modifying

the NO source term of method M2. This is not done for method M3, which would require a UDF to be applied only in the pilot flame region to zero the source term. However, preliminary tests showed that the extra NO production in the pilot is negligible in the context of the analysis in this chapter. Zero gauge static pressure is prescribed at the outlet boundary. The outer boundary is treated as an inviscid wall.

	Fuel inlet	Pilot inlet	Co-flow inlet
$\bar{V}_x[\frac{m}{s}] - RANS$		Meas. profile[96]	
$\bar{\tau}_{ij}[\frac{m^2}{s^2}] - RANS$		Meas. profile[96]	
$\bar{V}_x[\frac{m}{s}] - LES$	49.6	11.4	Meas. profile[96]
\tilde{Z}	1	0.27	0
\tilde{C}	0	0.9834	0
$\tilde{T}[K]$	294	1880	291
\tilde{Y}_{NO}	0	$4.8 \cdot 10^{-6}$	0

Table 4.1: Boundary conditions at the inlet boundaries.

In both RANS and LES simulations, pressure-velocity coupling is achieved using the COUPLED algorithm. In the RANS analyses, the convective terms of all transport equations are discretized with a second-order upwind scheme. In the LES simulations, the convective term of the momentum equations are discretized with a bounded central differencing scheme. All diffusion terms are discretized using second-order finite-differencing in both RANS and LES analyses. The RANS simulations are performed in a steady fashion. The LES simulations use a dual time-stepping approach with a bounded second-order implicit scheme for the time integration. For each time step 25 subiterations are performed. The time step size is $2.5 \cdot 10^{-6}$ s, which guarantees a Courant number lower than 0.2. The time step used with the fine grid was reduced by a factor of 1.3 to maintain the same CFL. After reaching statistically stationary flow fields, averages are computed across a period of over 8 flow-trough times (0.12 s).

RANS simulations were computationally cheap, requiring only a few minutes on 16 cores or fewer. In contrast, LES simulations demanded significantly greater resources, running for several weeks on up to 120 cores to achieve a properly averaged flow.

4.3 Results

This section presents and discusses the validation tests based on the CFD analysis of the Sandia flame D test case.

Figure 4.5 compares computed and measured profiles of Favre-averaged mixture fraction \tilde{Z} , temperature \tilde{T} , CO mass fraction \tilde{Y}_{CO} and OH mass fraction \tilde{Y}_{OH} on the centreline of the flame. The label 'RANS' indicates the results obtained with RSM using the baseline ω equations. The label 'LES crs.' indicates LES results obtained with the coarse mesh, and the label 'LES fin.' indicates LES results obtained with the fine mesh, which allows to resolve a larger spectrum of turbulent scales compared to the 'LES crs.' set-up. Simulations using Unsteady RANS (URANS) were performed using a double time step approach with a physical time step of 0.01 s and 25 subiterations per time step. As the difference between RANS and URANS results was negligible for all the quantities discussed in this section, the discussion below uses the RANS analysis of Sandia flame D.

Figure 4.5a shows the profiles of \tilde{Z} on the centreline. Closest to the nozzle ($x/d < 20$), the three CFD profiles are close to each other and in good agreement with experiments. This indicates that the velocity and turbulence boundary conditions at the inlets are properly defined, as the modeling choices made for the inlet boundary conditions have a significant impact on the flow field in the near-nozzle region. In the region $20 < x/d < 60$, the RANS \tilde{Z} profile drops more rapidly than the measured profile, indicating that fuel and oxidizer mixing predicted with RANS is faster than that in the experiments. The RANS misprediction of the rate of fuel and oxidizer mixing may be explained by the fact that complex fluid dynamic phenomena happen

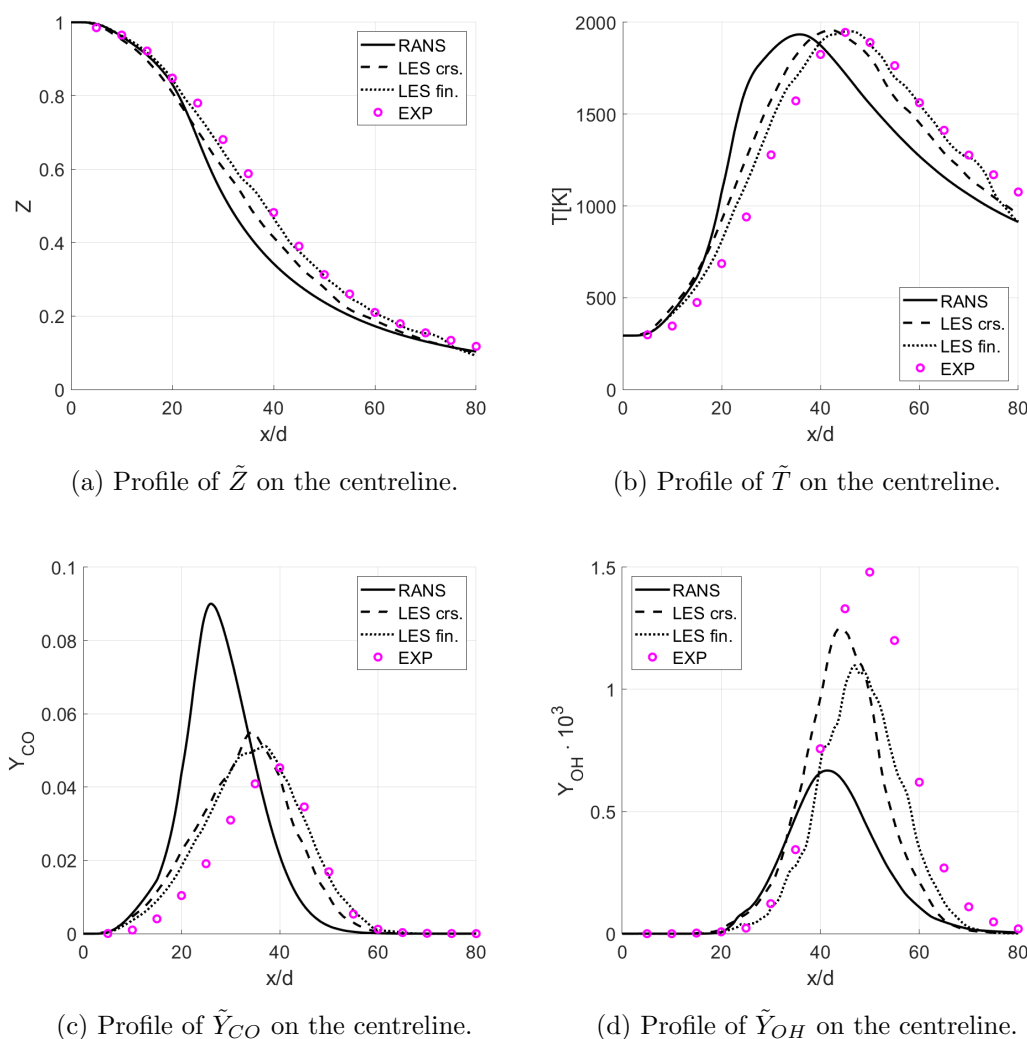


Figure 4.5: Measured and computed profiles of Favre-averaged mixture fraction \tilde{Z} , temperature \tilde{T} , CO mass fraction \tilde{Y}_{CO} , and OH mass fraction \tilde{Y}_{OH} .

in that region. Pecquery et al. [86] performed LES simulations of this test case and noted the presence of low-frequency modes, which are typical of jets, and lead to tangential asymmetries in the mean fields computed in their simulations. The 'LES crs.' set-up shows a clear improvement over RANS. Despite the predicted mixing is still faster than that of the experiments, the LES and measured profiles are closer to each other, and trends are similar. Due to the larger amount of resolved turbulent scales, the profile obtained with the 'LES fin.' set-up is in even better agreement

with experiments compared to the 'LES crs.' set-up.

Figure 4.5b reports the profiles of \tilde{T} on the centreline. The peak temperature is always well predicted and does not vary significantly with the set-up. RANS underpredicts the peak by 0.6%, while the 'LES crs.' set-up overpredicts the peak by 0.6%. The 'LES fin.' set-up underpredicts the temperature peak by less than 0.3%. One sees that a better prediction in mixing (see Fig. 4.5a) corresponds to a better prediction of the temperature peak position. The measured position of the temperature peak is $x/d=45$, whereas RANS moves upstream the peak at $x/d=35.7$. The 'LES crs.' approach predicts the highest value of temperature at $x/d=42.3$ and the 'LES fin.' approach at $x/d=44.3$.

Figure 4.5c presents measured and computed profiles of \tilde{Y}_{CO} on the domain centreline. The RANS set-up predicts the \tilde{Y}_{CO} peak to be 0.090, against a significantly lower measured value of 0.045. A similar result was obtained by Yadav et al. [130] with a similar set-up and the same code. That study predicted the peak value of \tilde{Y}_{CO} in Sandia flame D to be 0.108. The agreement between measured and computed profiles improves significantly with the LES approach, as the peaks predicted with the coarse and fine grids are 0.055 and 0.052.

Figure 4.5d presents measured and computed profiles of \tilde{Y}_{OH} on the domain centreline. The RANS set-up underpredicts the \tilde{Y}_{OH} peak: it calculates a value of $6.7 \cdot 10^{-4}$ against a measured value of $14.8 \cdot 10^{-4}$. The agreement of measured and computed profiles improves significantly using LES, as the peaks predicted with the coarse and fine grids are $12.5 \cdot 10^{-4}$ and $10.8 \cdot 10^{-4}$ respectively. As anticipated by inspecting Eq. (3.18), the OH molecule affects the formation of NO via the thermal path, even though its impact is not as significant as that of the O radical.

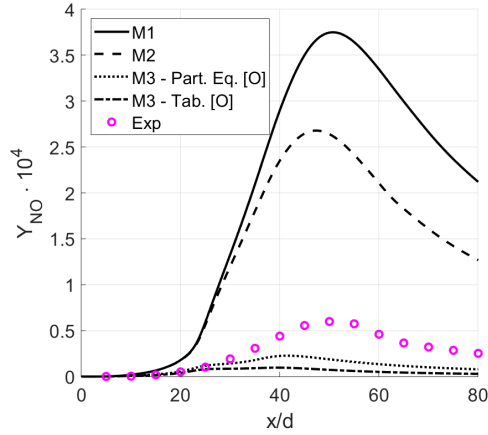
For all quantities examined in Fig. 4.5, the differences between the LES profiles obtained with coarse and fine grid analyses are fairly small. This indicates that the increased resolution achieved by using the fine grid does not justify, at least in terms of \tilde{Z} , \tilde{T} , \tilde{Y}_{CO} and \tilde{Y}_{OH} predictions, the higher computational cost incurred.

Figure 4.6 presents the comparison between computed and measured profiles

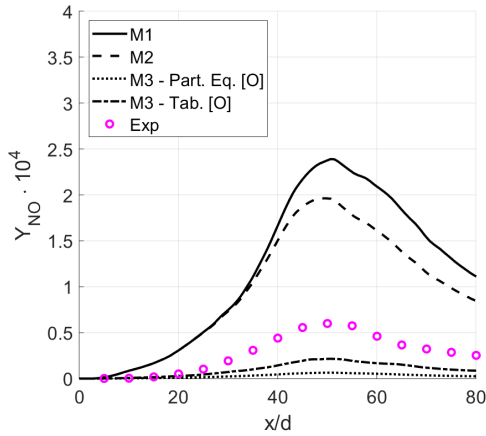
of Favre-averaged NO mass fraction. The computed profiles of the left, middle and right sub-figure have been obtained with RANS, LES with coarse grid and LES with fine grid, respectively. In each sub-figure, the line style indicates the approach applied to model the formation of NO, which is one of those presented in Sec. 3.3. The solid line denotes results obtained with the scalar transport with FGM closure method ('M1'), and the dashed line indicates results obtained with the corrected model to account for non-adiabatic phenomena ('M2'). Both the dotted and dot-dashed lines refer to results obtained with the simplified model for NO formation ('M3'). The difference between the two set-ups is the way of computing the oxygen atom concentration: the dotted line indicates that [O] is computed with the partial equilibrium approach ('Part. Eq. [O]'), and the dot-dashed line indicates that [O] is read from the look-up table ('Tab. [O]'). The simulation with the 'LES fin. - M3 - Tab. [O]' set-up has not been performed due to its high computational cost.

All three plots of Fig. 4.6 show that the scalar transport with FGM closure methods M1 and M2 significantly overpredict the profile of \tilde{Y}_{NO} on the centreline. The same code gave similar results in the past, when a similar modeling strategy was adopted [130]. A possible reason for this misprediction is suggested in a recent study by Yue et al. [131], which showed that using unstretched premixed flamelets resulted in better NO predictions than those obtained with counter-flow diffusion flamelets, which is the type of flamelet used also in the present study. The LES M1 and M2 results of Figures 4.6b and 4.6c show a reduction of the discrepancy between measured and computed profiles over the corresponding RANS results. Comparing the LES M1 and M2 profiles obtained with coarse and fine grids shows that the differences of the peak value are relative small. Therefore, the discussion below is based on the comparison of RANS and coarse grid LES results.

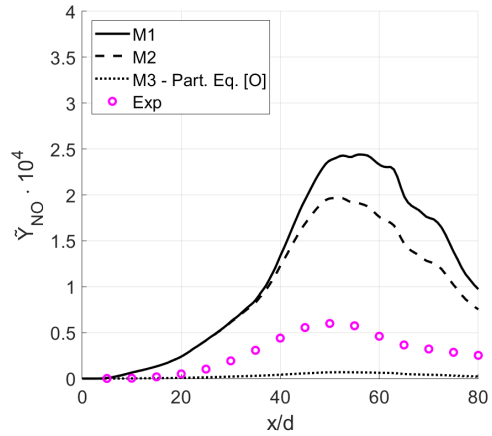
The comparison of Figures 4.6a and 4.6b shows that the LES approach combined with methods M1 and M2 improves the agreement with the experiments over that achieved by the same methods used in the RANS framework. When method M1



(a) CFD profiles with RANS.



(b) CFD profiles with LES and coarse grid.



(c) CFD profiles with LES and fine grid.

Figure 4.6: Measured and computed profiles of Favre-averaged NO mass fraction \tilde{Y}_{NO} on the centreline of the flame.

is used, the difference between experiments and CFD decreases by 43% when moving from 'RANS' to 'LES crs.'. When method M2 is used, the difference between numerical results and experimental data decreases by 34%. Consideration of non-adiabatic effects in NO formation via method M2 shows an improvement in the results with respect to method M1, regardless of the turbulence modeling approach. The \tilde{Y}_{NO} peak computed with RANS and method M2 is 29% lower than that computed with RANS and method M1 (Fig. 4.6a). Using 'LES crs.', the

peak computed with method M2 is 18% lower than that computed with method M1 (Fig. 4.6b). These reductions can be attributed to considering non-adiabatic phenomena in method M2, in particular to considering radiation heat transfer. The fact that the LES M2 profile is closer to the LES M1 profile than the RANS M2 profile is to RANS M1 profile, is probably due to a lower impact of radiation on NO formation in the 'LES crs.' case. This can be explained by the fact that the LES simulations predict the radiant fraction to be 15% lower than that computed with RANS. The radiant fraction quantifies the enthalpy deviation from the adiabatic case, which has a direct effect on the \tilde{Y}_{NO} deviation from the adiabatic case. The effect of radiation heat transfer on the formation of NO in the Sandia flame D test case computed herein is in line with that computed in previous studies. For instance, Frank et al. [30] estimated the reduction of the peak \tilde{Y}_{NO} due to the effect of radiation to be 37%, while Ihme et al. [46] estimated it to be 25-30%. Both studies modeled radiation in the optically thin limit, which is known to overpredict radiation heat transfer because it neglects self-absorption [30, 18]. The effect of radiation on peak \tilde{Y}_{NO} predicted by the M2 method is quantitatively similar to that obtained in the literature with more sophisticated approaches. This suggests that the correction proposed to the scalar transport with the FGM closure method may describe properly the effects of non-adiabatic phenomena on NO production.

The simplified method M3 significantly underpredicts the centreline profile of \tilde{Y}_{NO} in all three plots of Fig. 4.6. The comparison of the M3 profiles in Fig. 4.6b and Fig. 4.6c shows no significant difference of the \tilde{Y}_{NO} peak due to variations of the resolved turbulence spectrum. Therefore, also in the M3 case, the discussion below considers only results obtained with the 'RANS' and 'LES crs.' set-ups.

An advantage of method M3 is that it enables a separate analysis of the contribution of the thermal, prompt, and N_2O -intermediate mechanisms to NO formation. This approach is subjected to a certain degree of uncertainty, as the three formation mechanisms are in reality coupled by the reverse reaction rates, which depend on the local molar concentration of NO. Nevertheless, a meaningful

analysis can still be performed. Several studies showed that most of the NO in the Sandia flame D is formed via the prompt path. This is attributed to the fuel composition, which is partially premixed. According to Ihme et al. [46] 25% of the NO is formed via the thermal path, less than 5% is formed via the N₂O-intermediate path, and the rest is formed via the prompt path. Similarly, Pitsch et al. [90] suggest that one third of the total NO is formed via the thermal path, about 10% is formed via the N₂O-intermediate path and the rest is formed via the prompt path. Table 4.2 compares the peak of \tilde{Y}_{NO} computed in the present study with each mechanism with an estimate based on the measured peak and the consideration of [46] and [90].

	RANS		LES crs.		Expected
	Part Eq. [O]	Tab. [O]	Part Eq. [O]	Tab. [O]	
$\tilde{Y}_{NO,pr}$	$0.5 \cdot 10^{-5}$	$0.6 \cdot 10^{-5}$	$0.8 \cdot 10^{-5}$	$0.8 \cdot 10^{-5}$	$3.4 \cdot 10^{-5} - 4.2 \cdot 10^{-5}$
$\tilde{Y}_{NO,th}$	$1.8 \cdot 10^{-5}$	$0.3 \cdot 10^{-5}$	$0.6 \cdot 10^{-5}$	$2.0 \cdot 10^{-5}$	$1.5 \cdot 10^{-5} - 2.0 \cdot 10^{-5}$
\tilde{Y}_{NO,N_2O-int}	$0.1 \cdot 10^{-6}$	$0.4 \cdot 10^{-6}$	$0.1 \cdot 10^{-6}$	$1.7 \cdot 10^{-6}$	$3.0 \cdot 10^{-6} - 6.0 \cdot 10^{-6}$

Table 4.2: Contribution of each mechanism to peak NO computed by CFD, and expected range based on measurements and results of [46] and [90]

One sees that most of the difference between the computed and measured peak of \tilde{Y}_{NO} is due to the prompt mechanism modeling. The peak of prompt NO mass fraction is expected to be between $3.4 \cdot 10^{-5}$ and $4.2 \cdot 10^{-5}$. Instead, its contribution is observed to be below $0.8 \cdot 10^{-5}$ in all simulations.

The peak of thermal NO mass fraction is expected to be between $1.5 \cdot 10^{-5}$ and $2.0 \cdot 10^{-5}$. The results in Tab. 4.2 show how the accuracy of the thermal path model depends on the approach followed for the computation of [O]. When the RANS approach is used for turbulence, the partial equilibrium model for [O] works better than the value read from the look-up table. The opposite is true when the LES approach is used for turbulence closure. In those cases the Zeldovich mechanism leads to accurate results and the NO mass fraction attributed to the thermal path is in line with previous results in the literature.

Finally, the peak of N₂O-intermediate NO mass fraction is expected to be between $3.0 \cdot 10^{-6}$ and $6.0 \cdot 10^{-6}$. One sees that the predicted contribution of such a path is smaller than that expected. When the RANS approach is used for turbulence, the contribution of the N₂O-intermediate path is always below $0.4 \cdot 10^{-6}$. The best performing set-up is that using the LES approach for turbulence and value of [O] read from the look-up table, which predicts the contribution of such path to be $1.7 \cdot 10^{-6}$. Despite the differences, the N₂O-intermediate mechanism contributes to the total NO emissions only to a minor extent, making the prompt path model the main reason for the deviation between experiments and CFD.

Despite the De Soete model used in this study for prompt NO modeling may be outdated, it is often used in industrial applications [13, 40, 32, 64, 78]), where possible inaccuracies of the model are often hidden by the fact that the thermal path dominates the formation of NO. As most of the NO in Sandia flame D is due to the prompt mechanism, method M3 performs poorly for such a test case. In contrast, method M3 is expected to perform better in applications where the thermal path dominates the other paths. This is expected to be the case for the industrial gas burner studied herein, where the fuel composition is fully non-premixed.

4.4 Conclusions

The results presented in this Chapter show that, overall, the modeling approaches used in this study can predict the main characteristics of the validation test case. The RANS approach predicts faster fuel and oxidizer mixing with respect to measurements. This may be due to the presence of complex turbulent phenomena typical of jets and previously observed in Sandia flame D [86]. LES improves the prediction of the mixing rate and yields very good agreement of the temperature, CO, and OH mass fractions with measured data. The good results obtained with LES highlight the key role of achieving a sufficient fidelity level and choosing best suited models for turbulence, chemistry and turbulence-chemistry interaction

modeling. The peak temperature is always well predicted, independently of the approach adopted to model turbulence. The peak levels of CO and OH are well predicted by LES, whereas RANS overpredicts the peak value of CO and underpredicts that of OH. In all cases, methods based on the FGM scalar transport (M1 and M2) overpredict NO, and this is possibly due to the choice of the counter-flow diffusion flamelet type rather than the unstretched premixed flamelet type, as recently pointed out in [131]. The proposed correction to the FGM scalar transport (M2) to account for non-adiabatic effects lowers the peak of the centerline NO profile, bringing it closer to the measured value. The observed NO peak reduction attributed to non-adiabatic phenomena is in line with the literature. The sum of contributions approach (M3) significantly underpredicts the NO peak. This can be attributed to inadequacies of this approach to model the prompt path contribution. Therefore, the dominance of the prompt path in the considered test case, results in the observed underprediction of the measured peak of peak NO concentration. The thermal contribution is accurately predicted provided that the concentration of the oxygen atom is properly modeled. Using RANS, the thermal model gives accurate results if [O] is computed with the partial equilibrium approach, whereas using LES the thermal model gives accurate results if [O] is read from the look-up table.

Chapter 5

Cold flow analysis of industrial gas burner

The general aim of this chapter is to develop an experimentally validated computationally affordable RANS CFD technology for the analysis and design of industrial gas burners. The objective of the analyses herein is two-fold: on one hand, it is to investigate and shed light on the complex fluid dynamics of an industrial gas burner, supporting the findings on its flow physics with measurements of its flow field; on the other hand, the objective is to present parametric analyses of the simulation set-up, including inflow boundary condition (BC) choice, approach to the solution of wall-bounded flows, and turbulence closure, and provide guidelines on the best choices in RANS CFD simulations of industrial gas burners. The investigation focuses on the nonreactive flow of the burner because of the importance of an adequate prediction of turbulent flow patterns to reliably predict turbulent combustion problems, as discussed in the previous chapters. The considered test case is a non-premixed industrial burner for natural gas and methane combustion. The burner is designed to operate in continuous industrial processes with a firing range from 12 to 120 KW. The flow simulations and measurements of this study refer to two load conditions using only air as the working fluid. The main novelty of this chapter is the investigation of the cold flow physics of a non-premixed industrial

gas burner, and its dependence on the operating condition. Since the control of the turbulent flow pattern is one of the means available to improve the efficiency and reduce the emissions of this system, predicting and explaining the key flow features is paramount to its design optimization. The experimental part of this investigation is carried out by using a full-scale test rig that reproduces the conditions in which the gas burner is operated in production. This makes the presented analyses relevant to both the scientific and industrial communities of this sector.

The outline of the chapter is as follows. Section 5.1 presents the test rig and a general description of the fluid flow paths in this case study. In Section 5.2 the experimental set-up and the procedure followed for the measurements are described. Section 5.3 describes the CFD code and methodology, whereas Section 5.4 defines the physical domain, grids, and BCs. Section 5.5 assesses the grid independence of the CFD solutions. Section 5.6 presents the results of this study: first, the main findings of the parametric analyses varying inlet BC, calculation of the wall-bounded flows, and turbulence models are presented; then the main features of the flow field of the system are presented and discussed. Finally, Section 5.7 provides a summary of the chapter.

This chapter is an adapted version of Ortolani et al.[82].

5.1 Test Rig

The outer geometry of the considered burner, consisting of a case containing part of the nozzle, is reported in Fig. 5.1a. A fan, connected to the burner with an inlet duct, provides the air flow supply (Fig. 5.1b). The fan works at constant angular speed, with the air flow rate being regulated by a throttling valve located just before the case. The inlet duct has a rectangular cross section equal to that of the throttling valve case. Figure 5.1b also shows the combustion chamber bolted to the burner case. The chamber has a cylindrical shape and it is open on the outlet section, communicating directly with the external ambient. Figure 5.2a shows that

the nozzle consists of a conical part surrounded by a coaxial cylinder. The cone has several holes arranged in a periodic pattern. Figure 5.2a also highlights a flame detector, and a spark plug. Together with some bolts, these two components are the only elements breaking the axial symmetry of the nozzle geometry.

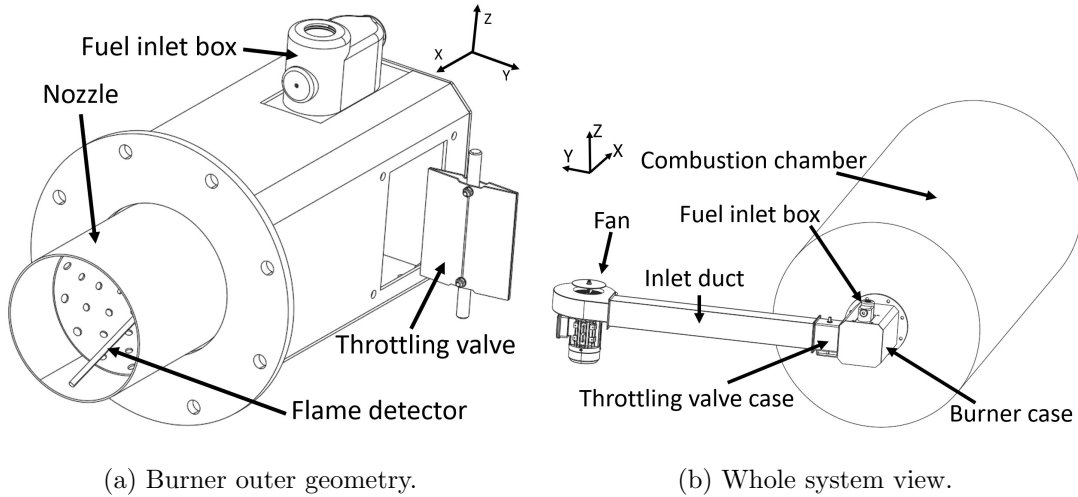


Figure 5.1: Studied gas burner.

The schematic of Fig. 5.2b shows the flow path in the burner. The stream of fresh air enters the case, and after a 90° turn, it splits into multiple co-axial streams. The innermost stream flows in a tube ("nozzle inlet duct") whose axis lays on the centerline of the chamber. This is the stream indicated by the central black arrow. This stream then passes through the nozzle and reaches the combustion chamber. Most of the remaining air enters the chamber through the holes on the conical part of the nozzle. Secondary air streams enter in the combustion chamber following two different paths: the small gap between the external face of the cylinder and the burner case, and the gap between the internal face of the cylinder and the cone. When the burner is firing, the fuel stream follows the path of the striped arrows in Fig. 5.2b, guided by the fuel system ducts shown in Fig. 5.2a. The fuel mixes with the air directly in the nozzle, and in this way, it feeds the flame.

Since this study focuses on the cold flow field of the considered system, the fuel inlet is disconnected from the fuel supply. It is also sealed so that no air enters from

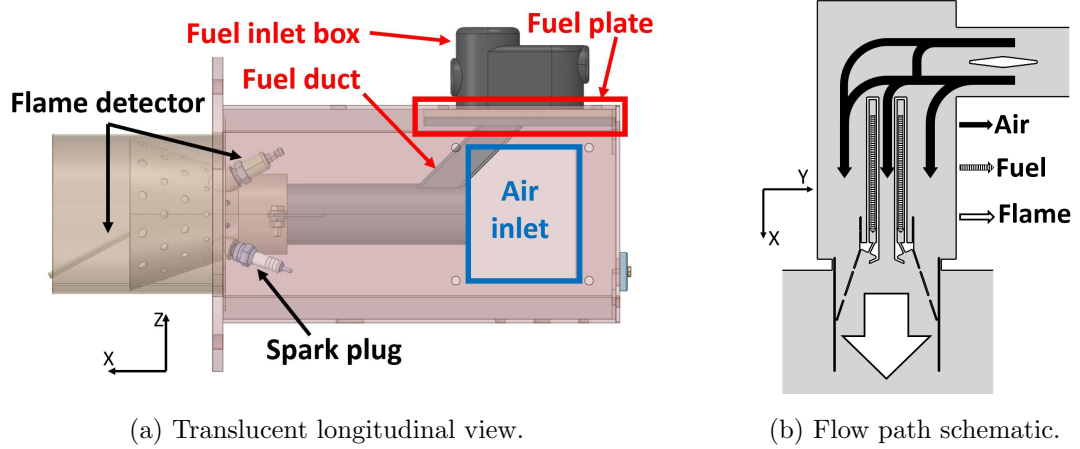


Figure 5.2: Inner views of gas burner.

there. In this way, the fuel inlet box communicates only with the nozzle via the fuel duct shown in Fig. 5.2a.

Figure 5.3 provides the symbols used in this study to denote the characteristic lengths of the system. The diameter and the length of the cylindrical combustion chamber, not reported in Fig. 5.3, are denoted by d_c and l_c , respectively. Table 5.1 reports all characteristic lengths normalized with the nozzle external diameter d_n , which equals 125 mm.

Table 5.1: Dimensions of primary inlet duct, gas burner, and combustion chamber normalized by nozzle external diameter d_n .

l_n/d_n	l_b/d_n	h_b/d_n	l_{in}/d_n	l_{x_b}/d_n	l_{x_h}/d_n	l_c/d_n	d_c/d_n
1.00	2.48	1.36	6.40	0.66	0.80	16.00	6.40

5.2 Experimental set-up

The measured quantities in this study are static pressure, total pressure, and velocity. Flush-mounted pressure taps are used to measure the static pressure. The probe used to measure the total pressure consists of a tube with a hole whose

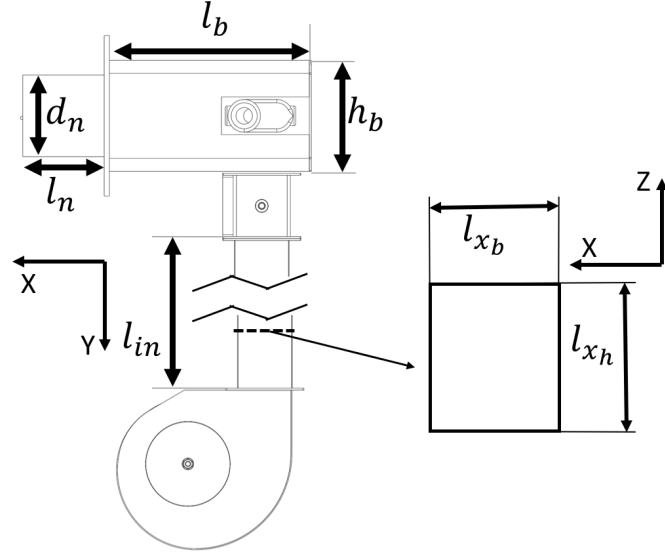


Figure 5.3: Geometry parameters of primary inlet duct and gas burner.

axis is oriented as the incoming flow. Both static and total pressures are measured with the SDP816-500PA analog transducer by Sensirion [99]. This sensor measures the difference between probed and ambient pressures, and it outputs an analog ratiometric voltage. The sensor covers a range of ± 500 Pa with an accuracy of $\pm 3\%$ of the measured value ± 0.1 Pa. Five of these transducers are connected to an Arduino board and collect 500 samples of static or total pressures with a sampling frequency of 5.4 Hz. In this chapter, the static and total pressures measured with these transducers are labeled "SDP816".

Some static and total pressure measurements are repeated with a second differential manometer to verify the calibration of the SDP816 transducer. For this purpose, the Kimo MP 200 P manometer [65], characterized by a range of ± 500 Pa with an accuracy equal to $\pm 0.2\%$ of the measured value ± 1.5 Pa, is used. This manometer measures the difference between probed and ambient pressures, and outputs its value on a screen. As this sensor does not have data-logging capability, an average pressure value is computed with 10 screen readings. In this study, the static and total pressures measured with this manometer are labeled "Kimo". Unless otherwise stated, the measured pressure data reported are those measured by the

SDP816 transducer.

A constant-temperature thermal anemometer, namely the TA440 model by TSI Incorporated [98], measures the velocity along the desired direction. The measured velocity component depends on the orientation of the probe. The measuring range of the thermal anemometer goes from 0 to 30 m/s with an accuracy of $\pm 3\%$ of the measured value and a resolution of 0.01 m/s. The anemometer has a sampling frequency of 1 Hz and measures time-averaged values of the velocity over 1 s. Each measurement is carried out for more than 5 min, providing velocity time-histories consisting of over 300 samples.

All measured time-series are elaborated to compute the mean value and the Root-Mean-Square (RMS) of the deviations from such mean value at each measurement point. The measured quantities presented in the following Sections 5.4 and 5.6, unless otherwise stated, are in form of time-averaged values.

The measurement locations are divided into three subsets or *stations* to help the discussion. Each station consists of all the measurements carried out in one region of the test rig. Station 1 is located at the mid length of the inlet duct, and is depicted in Fig. 5.4. Here the sensors are used to measure velocity and total pressure with the aim of providing data for the inlet BCs of the CFD simulations. Both quantities are measured at five positions, indicated by black dots in Fig. 5.4. The orientation of the probes is such that they capture the component of the flow velocity in the Y direction. The X and Z velocity components are neglected. The static pressure is measured on the midpoint of each side of the measuring section (white dots in Figure 5.4).

Figure 5.5 provides a schematic of the station 2, showing the locations at which the static pressure is measured on the burner case. A pressure tap is positioned on the fuel box (FB), as its pressure provides an indirect measure of the velocity in the nozzle itself. This method allows collecting information on the flow in the nozzle in a non-intrusive way. The figure also shows lines F1 and F4 along which the static pressure on the burner case is measured.

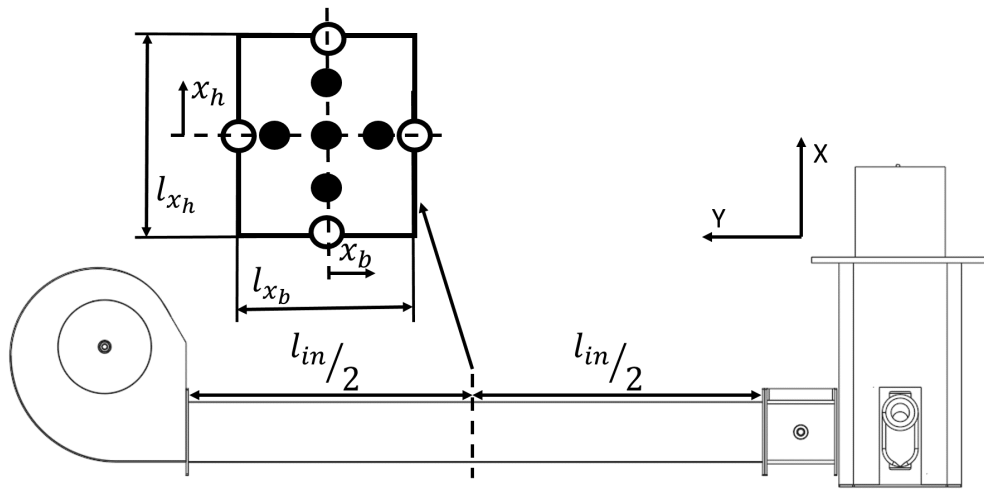


Figure 5.4: Schematic of station 1.

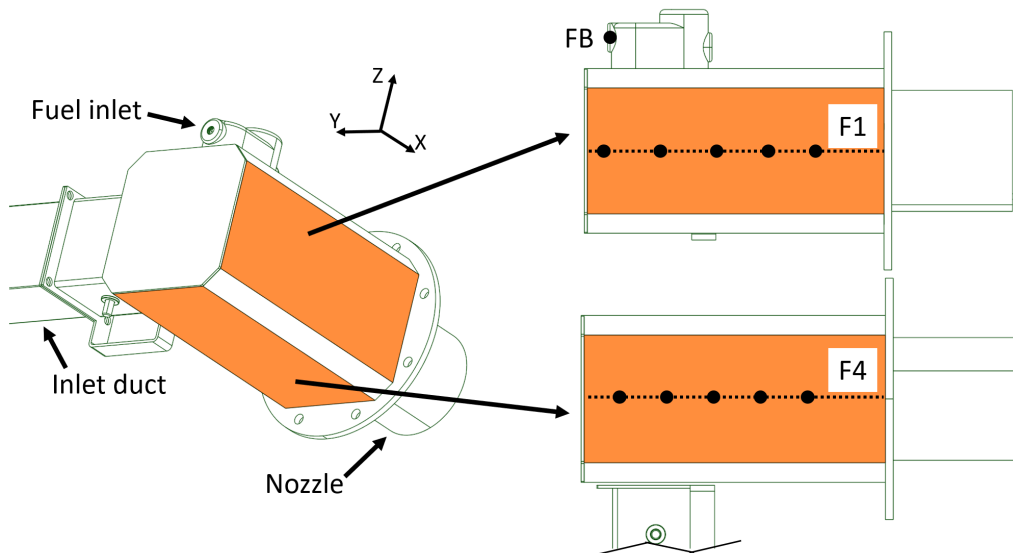


Figure 5.5: Schematic of station 2. Black dots indicate pressure tap positions.

A schematic of station 3 is given in Fig. 5.6a. The axial component of the velocity (V_x) is measured in the combustion chamber, namely along the three transverse lines E1, E2, and E3. Figure 5.6a also shows the origin of the selected reference frame. The origin is on the nozzle and chamber centerline, and its X position is at the bottom of the combustion chamber.

All the measurements are repeated for two load conditions. One is that of full

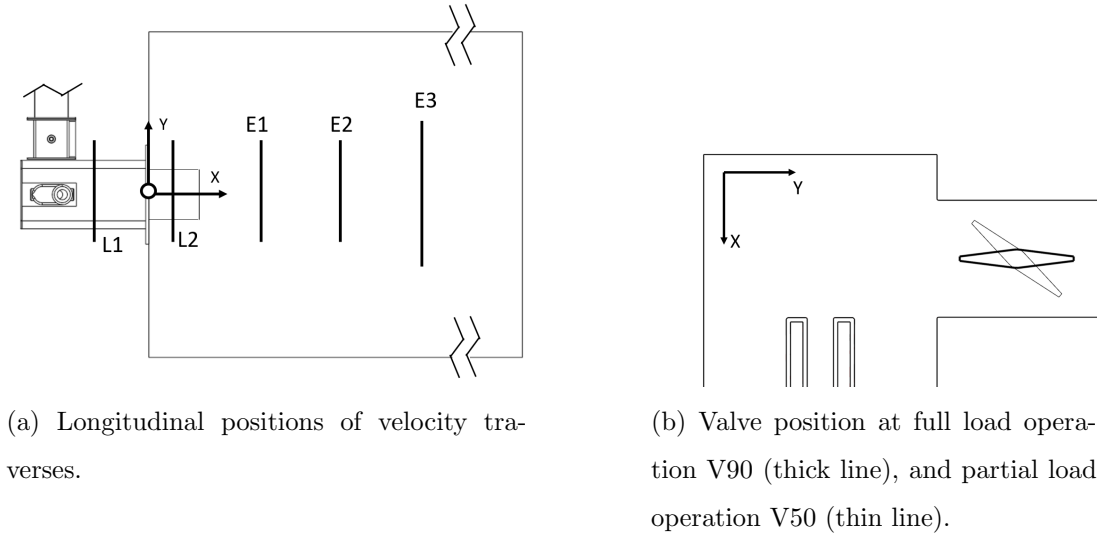


Figure 5.6: Schematic of station 3, and valve regulation.

load when the throttling valve is fully open (condition V90). The other is the partial load regime, corresponding to a partial valve opening of 50° (condition V50). A schematic of the valve orientation for the two configurations is shown in Fig. 5.6b.

5.3 Computational fluid dynamics method

All numerical analyses are carried out with the commercial CFD code ANSYS FLUENT [2], using version v19.3, unless otherwise stated. The code is used to solve the pressure-based incompressible RANS equations. FLUENT uses the finite volume method for the space discretization of all conservation laws. In all analyses, a second-order upwind scheme for the convective fluxes is chosen. Diffusion terms are discretized with second-order finite-differencing. All simulations herein are time-dependent, and, all reported numerical results are time-averages of unsteady CFD simulations using a first-order discretization scheme in time with a dual time-stepping approach. None of the considered simulations could be performed using a steady-state solver, because, even if not large, the physical level of unsteadiness prevented convergence to a mean state to be achieved with a steady solver. All

simulations use the COUPLED solver, which solves the continuity and momentum equations in a strongly coupled fashion, whereas all other transport equations are solved in a loosely coupled fashion.

Part of the presented analyses uses the $k - \omega$ SST turbulence model [69]. The model is based on Boussinesq hypothesis, and computes the turbulent viscosity μ_t from the turbulent kinetic energy (k) and the specific turbulence dissipation rate (ω), which are transported variables. The remainder of the analyses uses the higher-fidelity RSM approach [59].

RSM is a RANS approach that is not based on the Boussinesq hypothesis, and better accounts for the anisotropy of turbulence. Thus, it is often better suited for cases where this character is more pronounced, such as highly swirling flows [127, 75]. The independence of the Reynolds stress tensor τ_{ij} on the laminar stress tensor in the RSM approach, requires solving a transport equation for each of the six distinct components of τ_{ij} . Moreover, an additional transport equation for the dissipation of τ_{ij} needs to be solved. Therefore, RSM uses 7 transport equations to model turbulence. This increases notably computational costs with respect to two-equation turbulence models.

Several options are available for the equation of the τ_{ij} dissipation. These can be subdivided in ϵ -based methods, where ϵ is the turbulent dissipation rate, and ω -based methods. Two variants of each approach are implemented in FLUENT. The ϵ -based variants differ for how they model the pressure strain term in the τ_{ij} equations. The default option is that proposed by Gibson and Launder [35], Fu et al. [31], and Launder [61, 62]. This solution, named "linear pressure strain term", is less accurate than the "quadratic pressure strain term" by Speziale, Sarkar, and Gatski [108], but is found to be more stable. The ϵ -based RSM variant tested in this study is the latter one; it has been found that, in order to prevent these simulations from becoming numerically unstable, the convection terms of the transport equations of τ_{ij} and ϵ have to be discretized with a first order upwind scheme.

The available ω -based RSM variants are the RSM- ω and the RSM-BSL variants.

The RSM- ω model is based on the ω -equation of the standard $k - \omega$ model of Wilcox [125], which was shown to give free-stream sensitive results [71]. The RSM-BSL model uses instead the ω -equation of the baseline $k - \omega$ model of Menter [70], which removes the free-stream sensitivity. The ω -based RSM variant tested in this study is the latter one, which unlike the tested ϵ -based variant has been found to be sufficiently stable also with a second order upwind discretization of the convective terms of turbulence transport equations.

The RSM simulations are carried out with FLUENT version v21.2, as the use of v19.3 led to numerical instabilities causing residuals to rapidly grow, and the simulation to crash after just a few time steps.

5.4 Numerical set-up

5.4.1 Physical domain and grids.

The physical domain considered herein is shown in Fig. 5.7. It starts at the measurement station 1, it includes throttling valve, burner case and nozzle, and it contains the cylindrical combustion chamber. Preliminary analyses highlighted the necessity of resolving also the flow field around the combustion chamber to avoid strong numerical instabilities caused by recirculation regions reaching the outlet of the chamber. Thus, the physical domain extends $85d_c$ downstream of the chamber outlet, and $37.5d_c$ radially, as indicated in Fig. 5.7. Figure 5.7 shows the main outer boundaries of the physical domain, which include the primary inlet through which the fan feeds the burner, the secondary inlet through which air flowing past the combustion chamber enters the domain, the outlet boundary through which the primary and secondary air leave the domain, and the outer boundary. The BCs applied on these boundaries are stated in Section 5.4.2. The physical domain does not include the flame sensor, the spark plug and the bolts.

All meshes are generated with ANSYS FLUENT Meshing, and are high-quality hybrid unstructured grids with regular hexahedral cells in most of the domain.

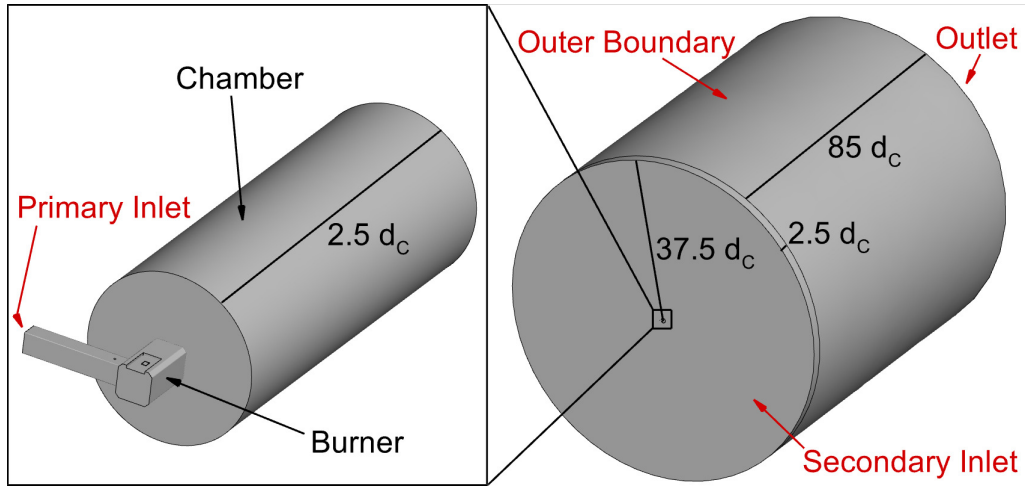


Figure 5.7: Main dimensions and outer boundaries of physical domain.

Polyhedral cells are used close to the boundaries, in regions connecting grid portions with different refinement, and where the complexity of the geometry requires their use. Figure 5.8 shows the longitudinal section of a grid with medium refinement for the V90 operating condition for simulations which resolve wall boundary layers (BLs) down to the wall without wall functions. As the number of cells increases significantly when solving BLs down to the wall, two different approaches have been assessed in this work. One reduces the computational cost by generating an inflation layer with only two cells in the direction normal to the walls. This method used wall functions (WFs). The other approach resolves BLs down to the wall. This is enabled by generating an inflation layer that guarantees a nondimensionalized wall distance y^+ of the cell centers closest to the walls smaller than 1 almost everywhere. For the fluid problem studied herein, the overall number of grid cells for the same level of grid refinement on the interior domain doubles when BLs are resolved. This method is labeled "WR" in the remainder of this article. Section 5.6.1 will present a comparative analysis of the results obtained with the WR and WF.

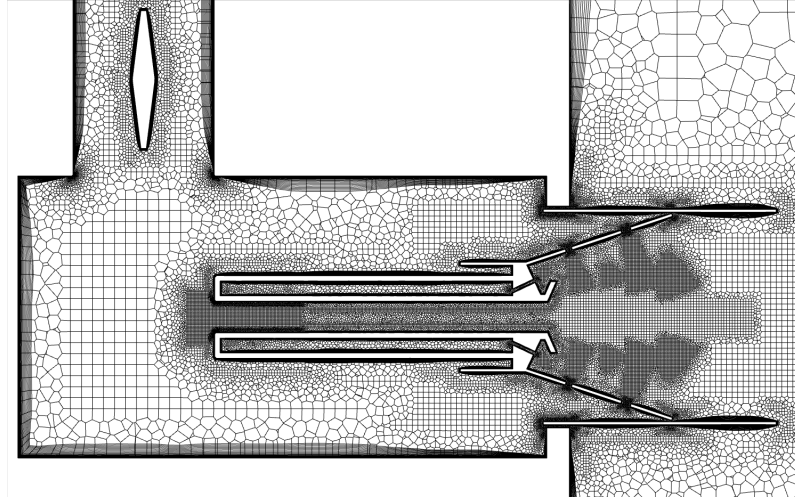


Figure 5.8: Longitudinal section of medium refinement grid for analysis of V90 operating condition resolving boundary layers down to wall.

5.4.2 Boundary Conditions

The BCs on the primary inlet boundary are prescribed as 2D maps of either total pressure or velocity. The two cases are labeled "P" and "V", respectively. These maps are obtained elaborating the data measured at station 1.

The spatial variations of the measured total pressure at station 1 are relatively low. The maximum deviation from the mean of the five values measured at the five positions indicated by black dots in Fig. 5.4 is less than 2.5%. Including also the measured wall static pressure (white dots in Fig. 5.4) this difference increases to 16%. Since these variations are relatively small, and the highest differences arise in a narrow region close to the wall, the prescribed total pressure is based only on the measured points indicated in black. A constant interpolation method is used, whereby the total pressure on a point of the boundary, is the closest measured value. The result of this operation is shown in Fig. 5.9a, in the form of total pressure profiles extracted from the generated maps.

The spatial variations of the measured velocity in the primary inlet duct are more significant than those of the total pressure, with a maximum deviation from the mean above 15%. Moreover, the velocity decreases sharply near the walls, becoming zero

there. Figure 5.9b shows the velocity profiles for the CFD simulations generated from the measured profiles. The CFD input values are interpolated along the lines $x_b = 0$ and $x_h = 0$ (Fig. 5.4) using a shape-preserving cubic Hermite interpolation. They are then extrapolated linearly to a distance from the wall of 20% of l_{x_b} and l_{x_h} , respectively. The profiles are then extended to the wall with the logarithmic law of the wall [53]. The 2D velocity map on the primary inlet boundary is obtained by interpolations based on the two profiles described above.

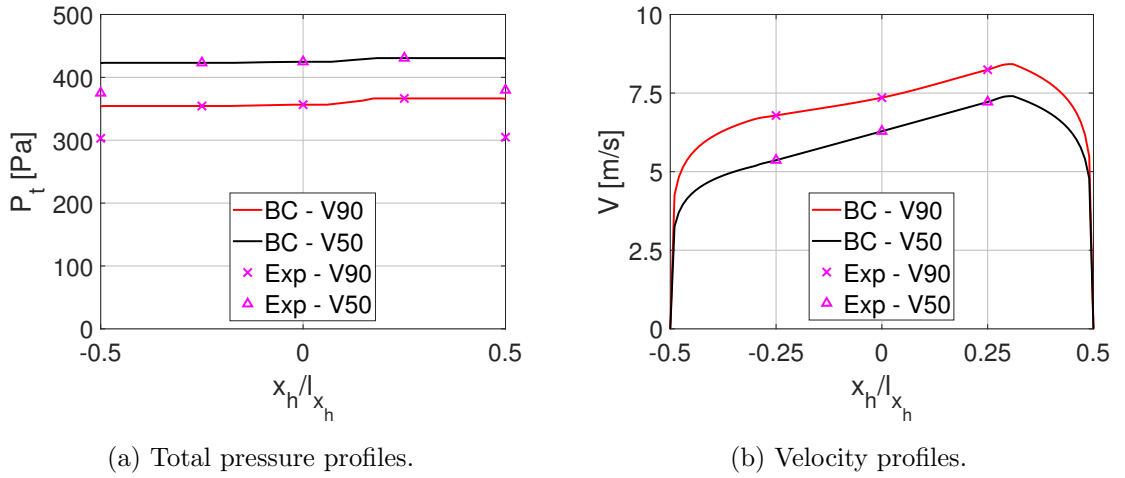


Figure 5.9: Measurement-based data for primary inlet boundary conditions at V90 and V50 conditions.

All wall boundaries, except the domain outer boundary, are treated as viscous walls. An inviscid wall condition is instead applied on the domain outer boundary (Fig. 5.7). A pressure outlet condition, which enforces zero gauge pressure, is enforced on the outlet boundary of the domain. To avoid the occurrence of back-flow on this boundary, a non-zero V_x of 0.002 m/s is imposed on the secondary inlet boundary.

Choosing either of the aforementioned methods for prescribing the BC at the primary inlet, and either of the approaches described in Section 5.4.1 for handling wall BLs, four possible set-ups are defined, labeled "P-WF", "P-WR", "V-WF", and "V-WR" in the parametric analyses of Section 5.6.1.

5.5 Mesh sensitivity analysis

Selected results of a three-mesh sensitivity study are presented in this section. Due to the high computational cost of these time-dependent simulations, the analysis is carried out only for the P-WF with $k - \omega$ SST model for the V90 operating condition. The limiting factor for the set-up choice is the computational cost of the fine grid simulation. The WF set-up was selected because the WR fine grid has a larger cell count of 17.43 million, and, more importantly, the convergence rate of the time-averaged flow field to a steady state was found to decrease when reducing the cell size in the near-wall regions. Both factors made the use of a fine grid without wall functions not affordable with the available computational resources. The reason for selecting the $k - \omega$ SST rather than an RSM set up, was also to make the computational burden of the fine grid simulation affordable.

The coarse, medium, and fine grids have, respectively, 3.8, 5.9, and 8.7 million cells. For reference, the WR grid with the same refinement of the medium WF grid away from walls has 12.0 million cells. Since the simulations are time-dependent, only the time-averaged flow fields computed with the three grids are compared. A constant time-step of $dt = 5 \cdot 10^{-3}s$ with 25 iterations at each time step are used in all simulations. The flow-through time, an estimate of the time required for a fluid particle to travel from the primary inlet boundary to the end of the combustion chamber, is defined as the ratio of a characteristic length and velocity. The characteristic length is defined as the sum of three lengths: the combustion chamber, the burner case and portion of the inlet duct included in the physical domain. The considered characteristic velocity is evaluated as the average measured velocity at station 1. All simulations are initialized with a hybrid initialization, and have been run for about 10 flow-through times in order to achieve a statistically stationary condition. From this time, simulations are run for another 50 flow-through times, and a time-average solution over this time interval is obtained at the end of the simulation. The solution sensitivity to mesh refinement is assessed by comparing local and global values of the mean flow field computed on the three grids.

One considered parameter is the computed mass flow rate \dot{m}_{air} . Another parameter used for the analysis is the RMS of the differences between the local velocity V_x in a section A normal to the X axis and the mean velocity V_{bc} in the same section. The definition of this global metric is:

$$RMS^A = \sqrt{\frac{\int_A (V_x - V_{bc})^2 dA}{A}} \quad (5.1)$$

All velocities in Eq. (5.1) are final time-averaged values of the simulation, and, therefore, RMS^A provides only a measure of the spatial variability of the velocity, and not a measure of possible unsteady fluctuations.

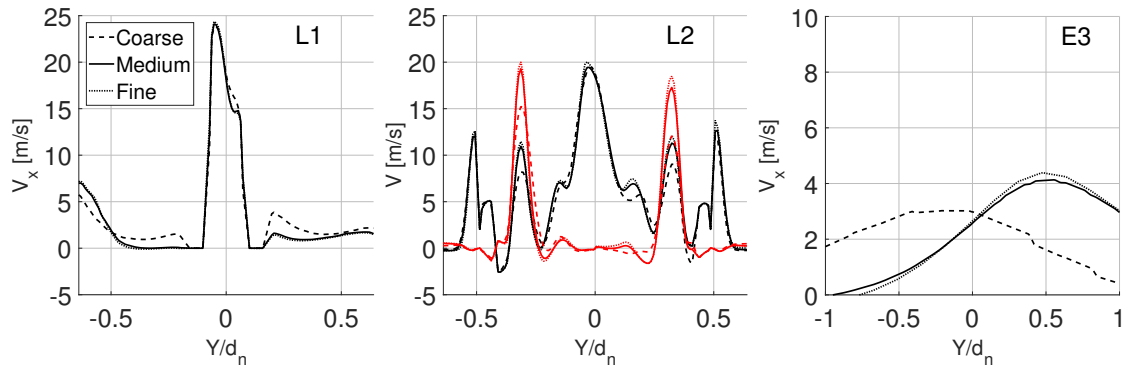
The first, second and third rows of Tab. 5.2 report integral quantities computed on the coarse, medium and fine refinement grids, respectively. The second column provides the mass flow; the third, fourth and fifth columns provide the value of RMS^A , respectively, on the cross sections at the longitudinal positions where lines L1, L2, and E3 are positioned in Fig. 5.6a. One sees that the values of the mass flow rates are very similar in all three grids, and the three values are within about 0.4% of each other. The value sets of RMS^A at the three axial positions highlight that the differences between medium and fine grids are notably lower than those between the medium and the coarse grids in all cases. In fact, the RMS^A percentage differences between medium and fine grids lay between 0.8% and 1.9%, whereas those between coarse and medium grids range from 2.0% to 7.5%. These data provide a first indication of sufficient grid independence of the medium grid.

The profiles of V_x computed on the lines L1, L2 and E3 are reported in Figures 5.10a, 5.10b and 5.10c, respectively. Figure 5.10b reports also the profiles of the radial velocity component V_r , which is significant at this position, due to the transverse jets in the conical nozzle. At all three positions, the profiles obtained with the medium and fine grids differ notably less than those obtained with the coarse and medium grids. On the line L2, the differences between coarse and medium profiles of V_r are particularly significant at $\frac{Y}{d_n} \approx \pm 0.3$, where the peaks of the radial velocity component due to the jets are observed. On line E3 in the combustion chamber,

Table 5.2: Mass flow rates and velocity RMS^A values on cross sections at positions L1, L2 and E3 computed with coarse, medium and fine grid $k - \omega$ SST P-WF set-up for operating condition V90.

Load Condition	$\dot{m}_{air} [\frac{kg}{s}]$	$RMS^A_{L1} [\frac{m}{s}]$	$RMS^A_{L2} [\frac{m}{s}]$	$RMS^A_{E3} [\frac{m}{s}]$
Coarse	$6.310 \cdot 10^{-2}$	2.971	1.022	0.895
Medium	$6.334 \cdot 10^{-2}$	3.210	1.043	0.980
Fine	$6.333 \cdot 10^{-2}$	3.269	1.052	0.993

large differences between the coarse and medium profiles of V_x are also observed, despite the smaller flow gradients in this region.



(a) Profiles of V_x on line L1. (b) Profiles of V_x (black) and V_r (red) on line L2. (c) Profiles of V_x on line E3.

Figure 5.10: Profiles of V_x velocity components on transversal lines L1, L2 and E3 computed with coarse, medium and fine grid $k - \omega$ SST P-WF set-up for operating condition V90. Middle subplot also reports profiles of V_r velocity component.

Figure 5.11 compares the coarse, medium and fine grid wall pressure profiles on the line F1 indicated in Fig. 5.5. Consistently with the trends highlighted above, the fine and medium grid profiles are superimposed, whereas the coarse grid profile differs slightly from the other two for $\frac{X}{d_n} < -1.5$. That is the region where the flow from the primary inlet duct hits the facing wall of the burner case, causing static pressure to increase at this location.

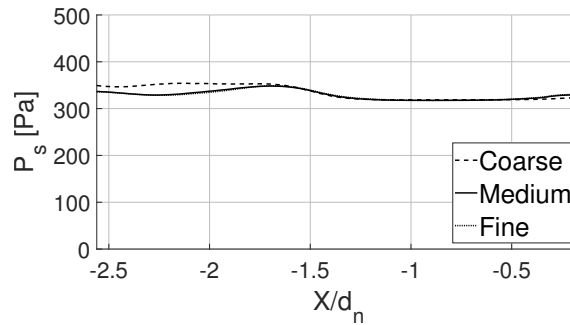


Figure 5.11: Wall pressure profiles on lines F1 computed with coarse, medium and fine grid $k - \omega$ SST P-WF set-up for operating condition V90.

The results above indicate the suitability of the medium refinement grid to properly resolve the flow physics of the considered industrial gas burner. As stated above, three wall BL resolving grids could not be used for the complete mesh sensitivity analysis, due to the computational burden of the fine grid analysis. However, a comparison of preliminary results obtained with a BL-resolving 8.44 million-cell coarse grid and a 12.00-cell medium grid showed relatively small differences of the two analyses, also in the near-wall regions. This occurrence gives confidence that also the medium level of refinement of WR set-up is adequate for the scopes of the reported analyses.

5.6 Results

The first part of this section presents a parametric analysis comparing a selection of results obtained with the numerical set-ups P-WF, P-WR, V-WF, and V-WR defined at the end of Section 5.4. In the second part, the solutions obtained with three turbulence models using the same wall BL approach and inlet BC type are compared. Finally, the detailed analysis of the flow field of the analyzed system is presented in the third subsection. The section also presents comparisons of the simulations with all available measured data.

5.6.1 CFD solution sensitivity to inlet BC and wall BLs resolution method

The $k - \omega$ SST turbulence model is used in all four numerical set-ups obtained by using either primary inlet BC and either wall BLs solution approach discussed in Section 5.4.

Figure 5.12a shows three sets of V_x profiles in the combustion chamber for the operating condition V90. The axial positions E1, E2, and E3 to which the profile sets refer are those indicated in Fig. 5.6a, and each set reports the CFD profiles computed with the four set-ups and the measured profile. The error bars on the experimental profiles are the RMSs of the deviations from the mean values of the measured time-series at each measurement point. The measurements at some locations were repeated, and the results are reported on the same plots. The left plot of Fig. 5.12a shows that, although the magnitude and position of the peak velocity are well predicted by P-WF, the shape of the profile differs from those predicted by the other three set-ups, which are closer to the measured data. This is a first indication of a poorer predictive performance of the P-WF set-up. At the axial positions E2 and E3, the Y position of the P-WF V_x peak is different from that of all other profiles (middle and right plots). Further investigations not reported for brevity show that a likely cause is that using wall functions to model part of the BL around the throttling valve results in a flow reversal where the valve has maximum thickness. This separation, not present when the BL is resolved down to the wall, affects the vortical patterns in the burner case and, subsequently, the V_x profiles in the combustion chamber. The flow reversal in the valve region is present also with the set-up V-WF. However, in the V-WF solution, its impact on the downstream flow is reduced due to the convective forces which, in the valve region, are higher than those of the P-WF flow field. This is because the velocities prescribed in set-up V-WF are higher than those computed with P-WF.

The P-WR, V-WR, and V-WF velocity profiles are close to each other. The only significant difference is seen in the left plot of Fig. 5.12a where the peak

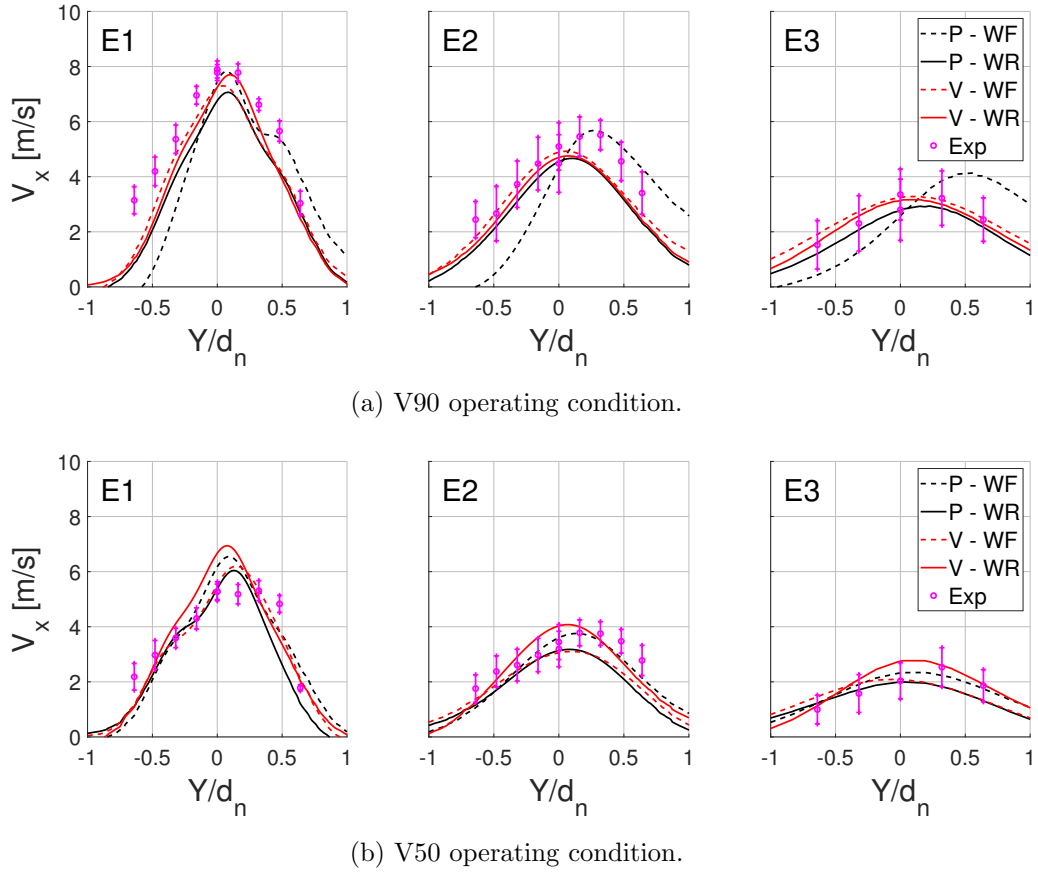


Figure 5.12: Analysis of solution sensitivity to inlet boundary conditions and wall BL modeling: computed and measured V_x profiles on transversal lines E1, E2, and E3 in combustion chamber.

velocity is underpredicted by P-WR. The profiles predicted by the set-ups with prescribed velocity at the primary inlet differ very little, suggesting that the prediction improvements associated with resolving BLs for the V90 regime are small when the primary inlet velocity is prescribed.

Figure 5.12b refers to operating condition V50, and has the same structure as Fig. 5.12a. The P-WF set-up appears to perform better than in the V90 case, since its predictions are now closer to those of the other three set-ups and the experimental data. The left plot of Fig. 5.12b highlights that the profiles computed prescribing the inlet velocity differ significantly only in the central part of the profile, for $-0.4 < \frac{Y}{d_n} < 0.2$. Significant differences occur instead over most part of the

profiles at stations E2 and E3 (middle and right plots). This suggests that these differences may be due primarily to differences in the flow field of the nozzle inlet duct. Thorough flow field investigations reveal that these differences occur in two regions: where the flow accelerates past the valve, and where it enters the nozzle inlet duct generating a recirculation region in the duct itself. These phenomena will be explained in detail in Section 5.6.3.

Table 5.3 reports the mass flow rate \dot{m}_{air} estimated using the experimental data and the results of the P-WF and P-WR simulations for the two operating conditions. The \dot{m}_{air} values computed by integrating the 2D velocity maps based on the measured velocities are reported in the Exp_{est} column. Those computed by the two CFD simulations are reported in the columns labeled P-WR and P-WF. The percentage differences of the \dot{m}_{air} values of two simulations are reported in the Δ_{CFD} column. The P-WF estimates are between 5.4% and 6% larger than P-WR estimates. These notable differences underline the importance of using the more reliable wall BL resolving approach rather than wall functions to properly correlate mass flow rate and pressure jump. The values of \dot{m}_{air} estimated from the measured velocities are consistently higher than those computed by CFD. This may be due to the uncertainty affecting the generation of the 2D velocity maps at the primary inlet.

Table 5.3: Air mass flow rate estimated experimentally from the measured velocities and computed by the CFD prescribing the inlet total pressure for the V90 and V50 operating conditions

Load Condition	$\dot{m}_{air}[\frac{Kg}{s}]$			$\Delta_{CFD}[\%]$
	Exp_{est}	P-WR	P-WF	
V90	$6.95 \cdot 10^{-2}$	$5.97 \cdot 10^{-2}$	$6.33 \cdot 10^{-2}$	6.0
V50	$5.79 \cdot 10^{-2}$	$5.33 \cdot 10^{-2}$	$5.62 \cdot 10^{-2}$	5.4

The static pressure analyses below use the nondimensionalized pressure p^* ,

defined by Eq. (5.2).

$$p^* = \frac{p}{p_{t0}} \quad (5.2)$$

where p is the local static pressure and p_{t0} is a reference pressure corresponding to the total pressure at the center point of the primary inlet boundary. Both p and p_{t0} are gauge pressures. The measured values of p_{t0} , and those computed by the V-WR and V-WF set-ups are provided in Tab. 5.4 (the P-WR and P-WF set-ups enforce the measured p_{t0} value. Since in the V-WR and V-WF set-ups, p_{t0} is an output of the simulation, it provides an indication of the computed pressure jump when the velocities are prescribed at the primary inlet. The measured p_{t0} values are fairly reliable, as indicated by the fact that the Kimo manometer p_{t0} value regime V50 is $421.9Pa$, very close to the value measured by the SDP816 transducer in Tab. 5.4.

Table 5.4: Reference pressures measured and computed by the CFD prescribing the inlet velocities for the V90 and V50 operating conditions.

Load Condition	$p_{t0}[Pa]$		
	Exp-SDP816	V-WR	V-WF
V90	356.5	486.7	444.7
V50	424.7	515.5	464.5

Figures 5.13a and 5.13b report the results obtained for the V90 regime on the lines F1 and F4, respectively, highlighted in Fig. 5.5. Figure 5.13a shows that the trend of the P-WF profile differs slightly from that of the other three set-ups. The cause of this deviation is likely to be the same yielding the P-WF velocity patterns observed in Fig. 5.12a and discussed above. The profiles of p^* predicted by V-WF are lower than those predicted by the other three set-ups, but the slope of this profile is similar to that of the P-WR and V-WR profiles. Figure 5.13b underlines that the V-WF profile on line F4 is lower than the other three numerical profiles. The results obtained for the V50 regime, not reported for brevity, show that all CFD profiles are very close to each other.

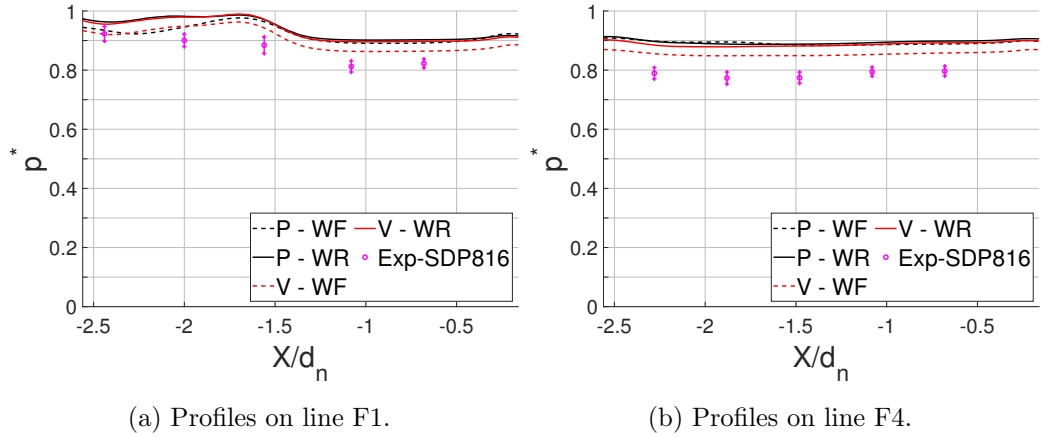


Figure 5.13: Analysis of solution sensitivity to inlet boundary conditions and wall BL modeling: computed and measured nondimensionalized static pressure at V90 condition.

Finally, Tab. 5.5 reports the values of p^* evaluated in the fuel box (FB in Fig. 5.5) for all considered cases. The value of p_{FB}^* measured with the Kimo transducer for the V50 condition is -0.069 . V-WR and P-WR seem to perform slightly better than V-WF and P-WF, even though the differences are minimal. This may suggest that resolving wall BLs has a stronger impact on the nondimensionalized static pressure predicted in the fuel box than the choice of the quantity prescribed at the primary inlet.

Table 5.5: Nondimensionalized static pressure p^* in the fuel inlet box evaluated with different set-ups for V90 and V50 conditions

Load Condition	$p_{FB}^*[-]$				
	Exp-SDP816	V-WR	V-WF	P-WR	P-WF
V90	-0.107	-0.111	-0.121	-0.111	-0.120
V50	-0.062	-0.070	-0.077	-0.072	-0.080

The results shown in this section indicate that P-WF gives poorer predictions in full load conditions, while V-WR overestimates velocity magnitudes in partial load

conditions. Thus, P-WR has been chosen as baseline set-up for the remainder of the analyses, as it gives good predictions in both operating conditions and is more trustworthy than V-WF which does not resolve BLs.

5.6.2 CFD solution sensitivity to turbulence model.

This section presents a parametric study on the impact of using either the SST or the RSM turbulence model in the P-WR analysis of the considered problem.

Figures 5.14a and 5.14b, featuring the same structure of Figures 5.12a and 5.12b, report the V_x profiles on in the combustion chamber for operating conditions V90 and V50, respectively, using the considered turbulence models. At design conditions (Fig. 5.14a), the two RSM set-ups predict very similar velocity profiles. The RSM set-ups yield slightly better prediction than the $k - \omega$ SST, especially in the region close to the nozzle exit (line E1). Some larger differences between the two RSM set-ups occur for the V50 condition Fig. 5.14b). The RSM-BSL model predicts the position of the peak velocity and the overall shape of the distribution better than both the SST and RSM- ϵ . The latter two models, however, yield a better prediction of the peak velocity magnitude on the E1 line. The $k - \omega$ SST model performs slightly worst than the RSM variants, especially in the V90 condition, where the values of V_x that it predicts close to the nozzle exit are too low with respect to measurement (left plot of Fig. 5.14a).

The comparison of the p^* profiles on the F1 and F4 lines, not reported for brevity, does not show significant differences among the predictions using the three turbulence models.

Table 5.6 provides the values of p^* in the fuel box. One sees that all models succeed in predicting a small negative gauge pressure, differing from the experimental value by less than 1% of p_{t0} for the $k - \omega$ SST and RSM-BSL set-ups. The RSM- ϵ model underestimates the magnitude of the FB gauge pressure, particularly at design conditions. A possible cause may be the use of a first order discretization for the convective terms in the τ_{ij} and ϵ equations, as discussed in

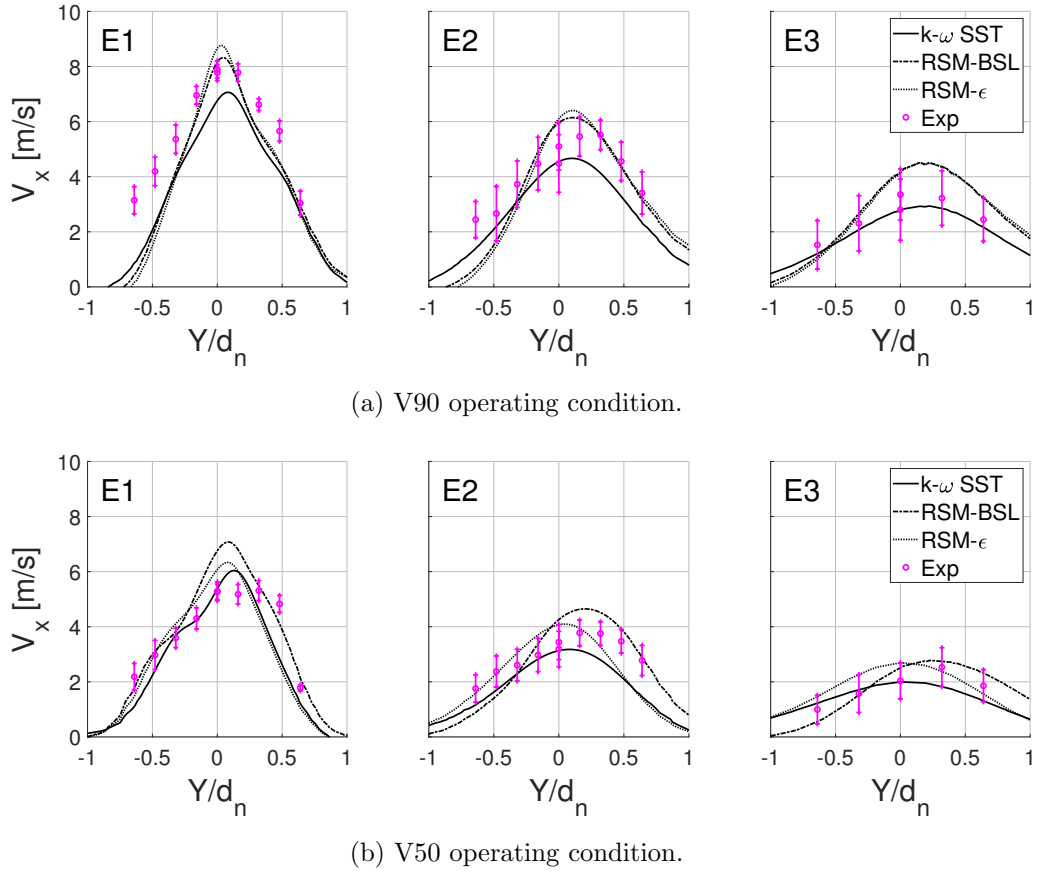


Figure 5.14: Analysis of solution sensitivity to turbulence model: computed and measured V_x profiles on transversal lines E1, E2, and E3 in combustion chamber.

Section 5.3. Overall, all turbulence models perform fairly well for the V50 condition, although the RSM predictions are closer to the experimental measurement than the $k-\omega$ SST model. The p^* value recorded by the Kimo manometer for the V50 regime is -0.069 , slightly different from the reading of that SDP816 transducer, and very close to the RSM-BSL prediction.

The comparative analysis above highlights that, overall, the RSM-BSL set-up yields prediction improvements over the $k-\omega$ SST and the RSM- ϵ set-ups. Therefore, the RSM-BSL method is used in the detailed flow analyses presented below.

Table 5.6: Nondimensionalized static pressure p^* in the fuel inlet box measured and evaluated with different turbulence models for V90 and V50 conditions

Load Condition	$p_{FB}^*[-]$			
	Exp-SDP816	$k-\omega$ SST	RSM-BSL	RSM- ϵ
V90	-0.107	-0.111	-0.102	-0.082
V50	-0.062	-0.072	-0.069	-0.059

5.6.3 Flow field analyses

In the analyses below, the P-WR RSM-BSL set-up is used to investigate the key flow features of the gas burner for both V90 and V50 operating conditions.

5.6.3.1 Flow field at design conditions

Figure 5.15 shows the flow field in the burner case at the design conditions V90. As the valve is parallel to the direction of the oncoming flow, the air stream flows around the valve without flow reversals. However, separation occurs downstream, due to the backward facing steps at the junction of the inlet duct and the burner case. The resulting vortical structures are visible in all three subplots of Fig. 5.15b. The recirculation zone labeled "A₁" covers the whole width of the burner case. The fuel duct and plate, highlighted in by solid and dashed rectangles, respectively, in Fig. 5.15b, and visible more clearly in Fig. 5.2a, interact with the counter-rotating vortex in the upper region of the case, breaking it into two weaker vortices labeled "B₁" and "B₂". The three plots of Fig. 5.15b are similar to each other, and show that the velocity gradients in the X direction are small in this region. In the region highlighted by the rectangle in Fig. 5.15a, one sees that the fluid accelerates entering the nozzle inlet duct. A recirculation region is formed on the inner wall of the nozzle inlet duct opposite the direction of the oncoming flow.

Figure 5.16 reports the velocity field in the YZ planes whose X positions are indicated in Fig. 5.15a. In all three planes, the asymmetry of the V_x contour

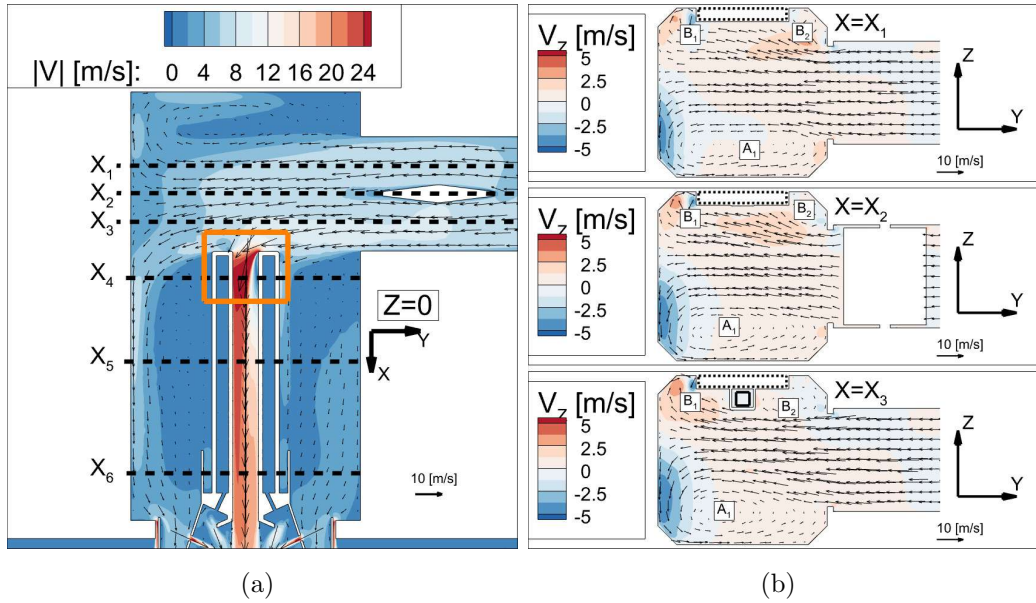


Figure 5.15: Velocity field in burner case at V90 condition computed with RSM-BSL P-WR.

maps of the flow approaching the nozzle from outside the fuel duct is visible. Flow asymmetry exists also in the nozzle inlet duct, as clearly visible in Fig. 5.16a. The reduction of V_x in the Y direction indicates that most of the flow rate goes through the half of the burner case at $Y < 0$. This effect is particularly significant at the section closer to the inlet duct (left plot). Figure 5.16 also illustrates the downstream development of the vortices identified in Fig. 5.15b. The strongest vortex "A₁" dominates the flow in the burner case. The vortex "B₂" is completely dissipated, as it is no longer visible in Fig. 5.16b. The vortex "B₁" does not disappear completely, but its intensity decreases significantly as the stream advances in the burner case.

The velocity field of the nozzle is analyzed in Fig. 5.17. A fast stream on the centerline, originating from the nozzle inlet duct, is visible in Fig. 5.17a. The velocity contour map also highlights the asymmetry of this primary stream. High-speed secondary streams or jets emanate from the holes on the nozzle cone, and merge with the primary stream. Figures 5.17b and 5.17c show the flow patterns before and after the nozzle. One can see that the vortex "A₁" generated upstream

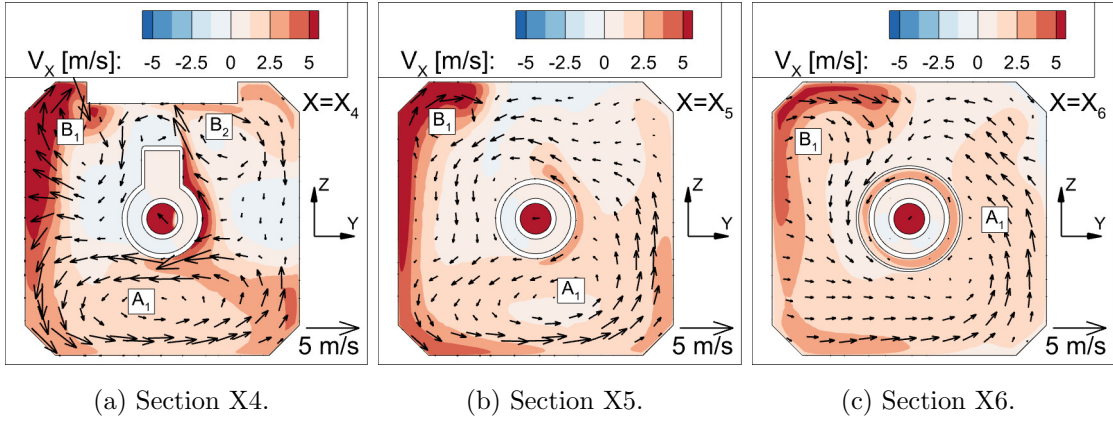


Figure 5.16: Velocity field in downstream part of burner case at V90 condition computed with RSM-BSL P-WR.

is still significant at the inlet of the combustion chamber.

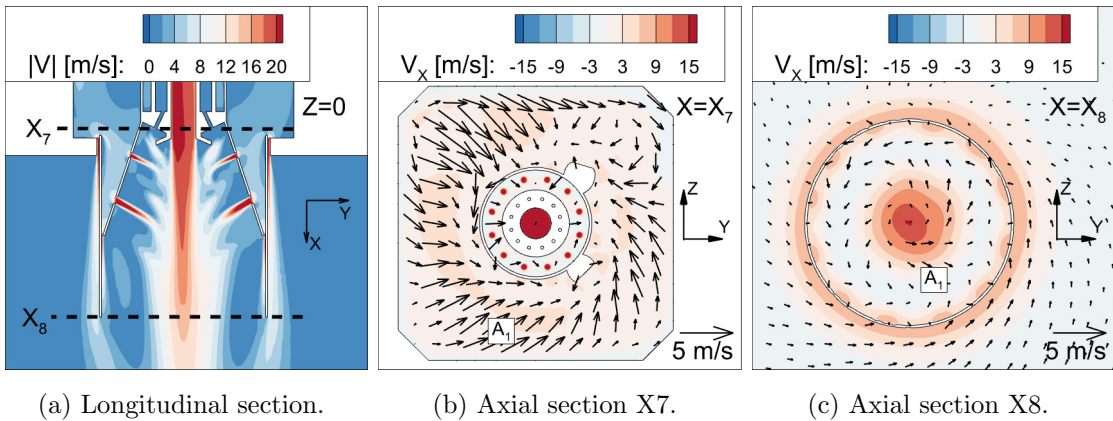


Figure 5.17: Nozzle velocity field at V90 condition computed with RSM-BSL P-WR.

Figure 5.18 shows the contour plot of p^* in the plane $Z = 0$ of the burner case. The figure shows a stagnation region (highlighted by a rectangle) resulting from the impingement of the oncoming flow entering the case from the inlet duct.

Computed and measured p^* profiles on lines F1 and F4 are compared in Figures 5.19a and 5.19b, respectively. On line F1, both experiments and simulations predict higher static pressure in front of the inlet duct ($\frac{X}{d_n} < -1.5$) than immediately downstream ($\frac{X}{d_n} > -1.5$). This higher pressure is caused by the impingement of the

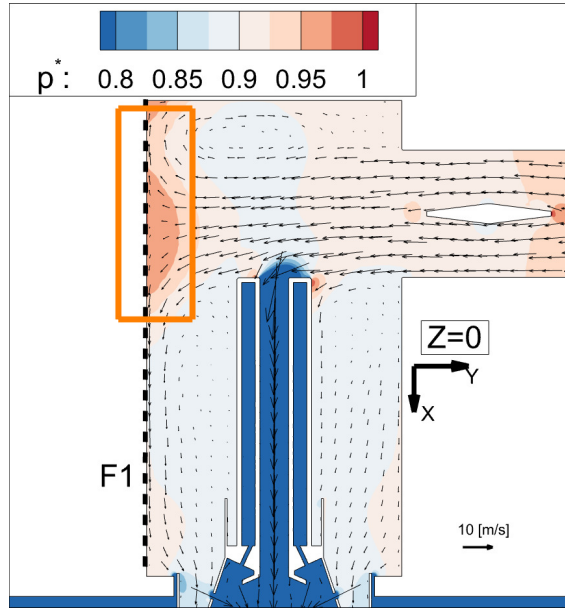


Figure 5.18: Nondimensionalized static pressure field in burner case at V90 condition computed with RSM-BSL P-WR.

oncoming primary flow on the wall of the burner case. On line F4 (Fig. 5.19b), both simulations and experiments show that p^* is almost constant, and a small adverse pressure gradient exists. Both plots of Fig. 5.19 show that the level of static pressure in the burner case is overpredicted by CFD. This implies that the pressure drop in the inlet duct and past the valve is underestimated by CFD. This could be due to the fact that the computed velocity field on the primary inlet boundary does not feature transverse velocity components, and, therefore, does not take into account all the expected three-dimensionality of the flow coming from the fan.

Measured and computed profiles of the V_x velocity component on lines E1, E2, and E3 are compared in Fig. 5.20. Inspection of these profiles indicates that the lack of axial symmetry in the burner case and around the nozzle extends to the combustion chamber. The measured profiles of all plots of Fig. 5.20 show that the peak velocity is shifted towards positive Y values, and this pattern is correctly predicted by the CFD simulation. The asymmetry is due to the highly 3D flow field in the burner case, caused primarily by the 90° turn when the primary stream enters

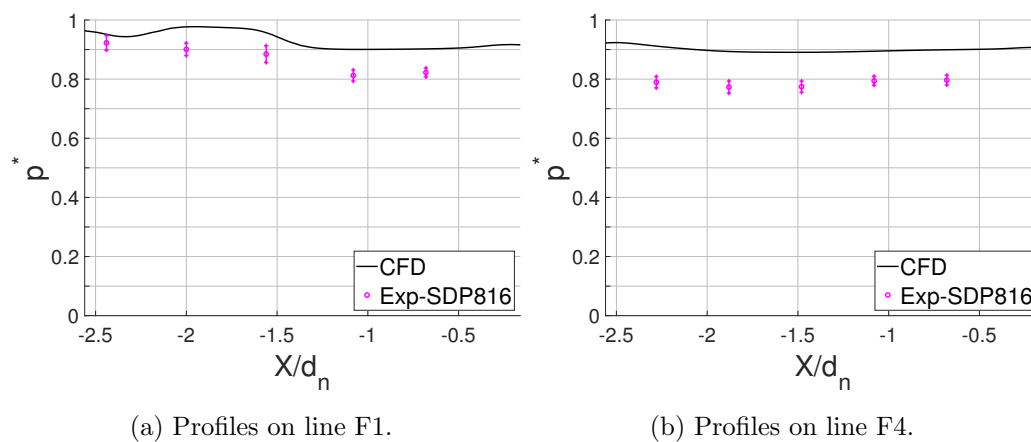


Figure 5.19: Measured and RSM-BSL P-WR profiles of nondimensionalized static pressure at V90 condition.

the burner case. Computed velocity profiles close to the nozzle (left and middle plots) are in good agreement with experiments both in terms of peak velocity and shape of the profile. Further downstream (right plot) the computed V_x profile is slightly higher than the measured profile, although the overall agreement remains fairly good.

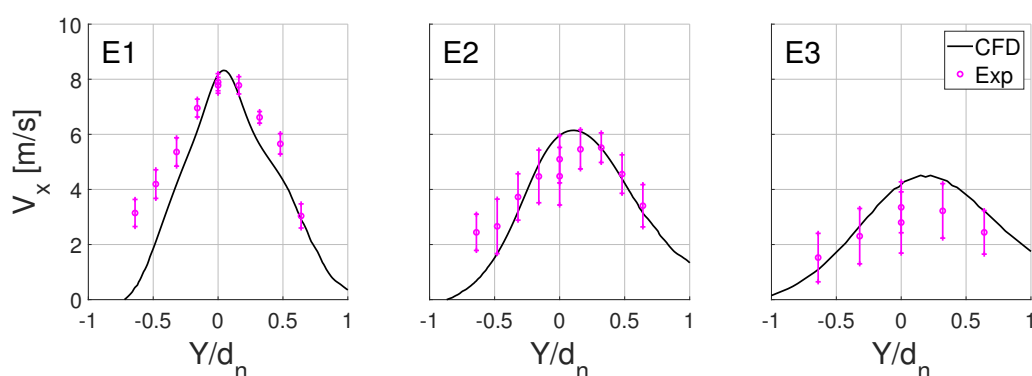


Figure 5.20: Measured and RSM-BSL P-WR V_x profiles on transversal lines E1, E2, and E3 in combustion chamber at condition V90.

5.6.3.2 Flow field at off-design conditions

Figure 5.21 presents the velocity field in the burner case for the off-design regime V50. As highlighted in Fig. 5.21a, the direction of the longer axis of the valve cross section forms an angle of 40° with the oncoming flow direction. Due to this high flow incidence to the valve, a low-speed recirculating flow region forms behind the valve. A second flow feature caused by this orientation of the valve is an acceleration of the two streams flowing on the two sides of the valve. These high velocity streams are highlighted with ellipses. The stream highlighted by the lower ellipse reaches directly the nozzle inlet duct in the region indicated by a rectangle. When this stream hits the inlet area of the nozzle duct, a separation bubble forms on the inner wall of the duct facing the oncoming stream, similarly to the V90 operating condition. Figure 5.21b shows the presence of two secondary flows in the Z direction at the end of the inlet duct, highlighted by dashed oriented curves in the central plot. These secondary flows are due primarily to the two forward-facing steps located at the top and bottom of the inlet duct, indicated by circles in all three subplots. To a minor extent, vortices A_1 and B_1 also contribute to the formation of these secondary flows, by pushing the flow toward the center of the inlet duct. The point where the two secondary flows meet is marked by a solid circle in Fig. 5.21a. This flow feature also exists at the design condition V90, but, due to the greater momentum of the flow in the Y direction following the valve (i.e. larger V_y level), it is less pronounced. This can be seen by comparing Figures 5.15b and 5.21b. The comparison also highlights that the velocity variations in the X direction, in this region of the burner case, are stronger in the V50 condition. Figure 5.21b also shows the presence of two secondary vortices, " A_0 " and " B_0 ", which are not observed at design conditions. These vortices are not convected downstream: they are visible in the top subplot of Fig. 5.15b, and by the time the flow reaches the section at $X = X_3$, they are no longer visible.

The three subplots of Fig. 5.22 examine the velocity field at the axial stations X_4 , X_5 and X_6 indicated in Fig. 5.21a. The behavior of the flow in this region is

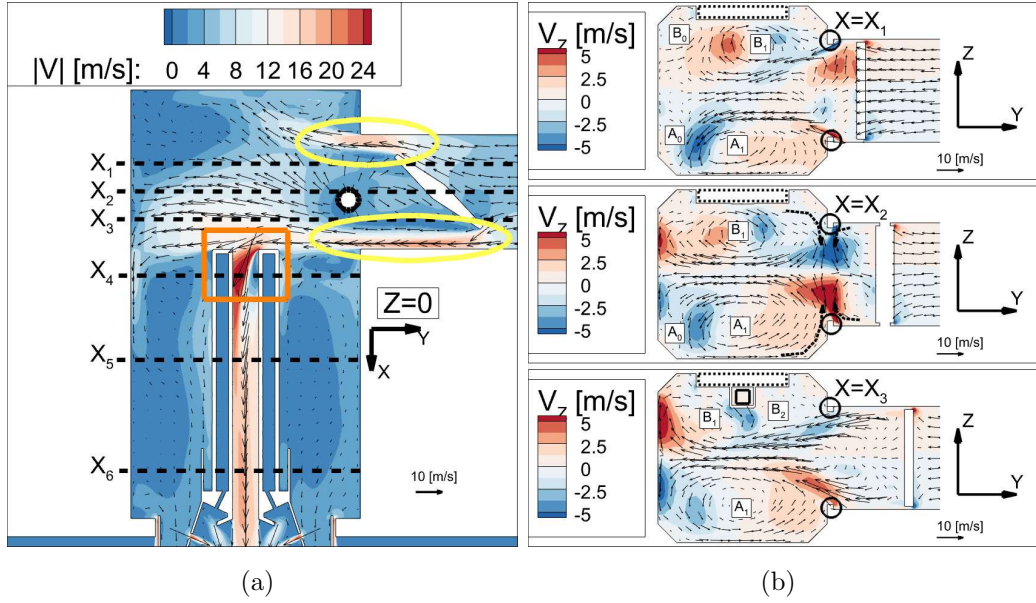


Figure 5.21: Velocity field in burner case at V50 condition computed with RSM-BSL P-WR.

similar to that of the V90 regime considered in Fig. 5.16, with some differences. For example, the interaction of vortices A_1 and B_1 , which have different relative strengths with respect to the design condition, lead to the formation of a small secondary vortex B_3 at station X_5 , not observed in the V90 operating condition.

The flow field in the nozzle is visualized in Fig. 5.23. The overall velocity level is in the V90 condition. Figure 5.23c also shows that the vortex A_1 persists in the combustion chamber, similarly to the design condition.

Figure 5.24 compares CFD and measured p^* profiles along lines F1 and F4, and its inspection leads to similar considerations to those reported in Section 5.6.3.1 for the V90 condition. For the V50 operating condition, two sets of measured static pressure are available, one measured with the SDP816-500PA analog transducer (Exp-SDP816 in the legend) and one measured with the Kimo MP 200 P manometer (Exp-Kimo in the legend). In this operating condition $p_{t0} = 424.7\text{Pa}$ for SDP816 and CFD, while $p_{t0} = 421.9\text{Pa}$ for Kimo. Figure 5.24 shows that the two transducers give very similar readings. The simulation predicts a peak static pressure at $-2 <$

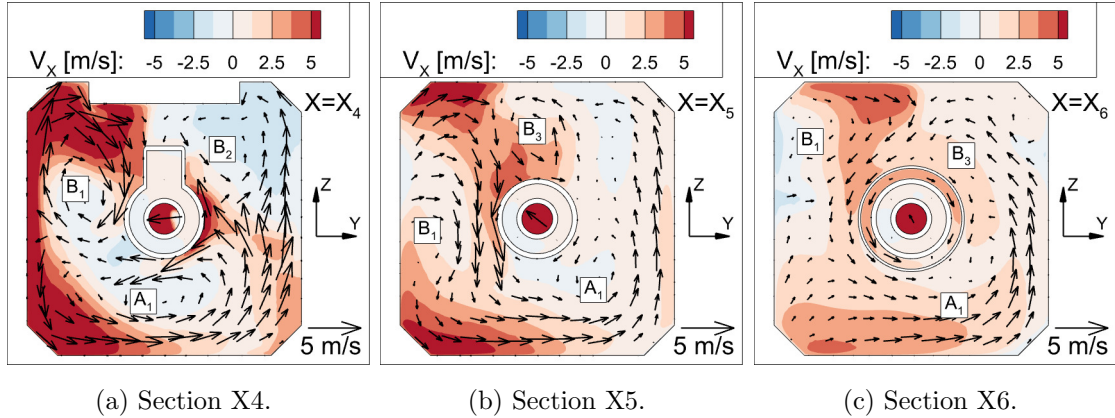


Figure 5.22: Velocity field in downstream part of burner case at V50 condition computed with RSM-BSL P-WR.

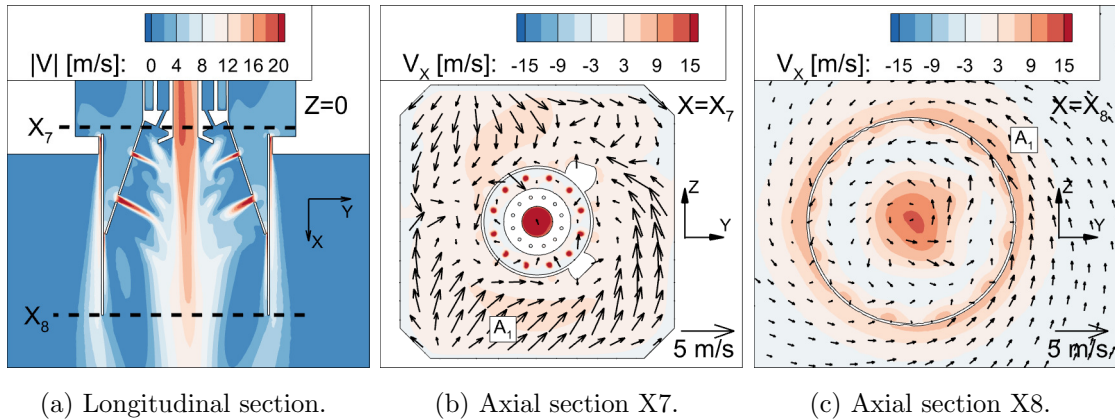


Figure 5.23: Nozzle velocity field at V50 condition computed with RSM-BSL P-WR.

$\frac{X}{d_n} < -1.5$ not seen in the experimental data. The CFD peak occurs at the position where the stream highlighted by the ellipse below in Fig. 5.21a hits the wall of the burner case. Possible reasons for this mismatch could be that the position and size of the high pressure region may depend on seemingly minor geometric features not included in the physical domain. Moreover, the distribution of the pressure taps may be too coarse to resolve this pressure variation. Both the computed and measured pressure profiles on line F4 (Fig. 5.24b shows that the adverse pressure gradient in the streamwise direction is stronger than that observed in Fig. 5.19b

for the V90 operating condition. The magnitude of the predicted and computed pressure gradient is in good agreement.

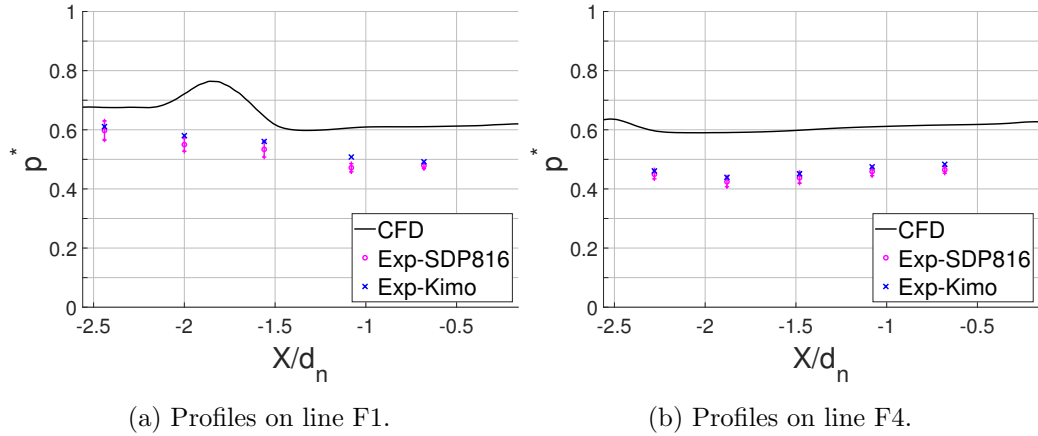


Figure 5.24: Measured and RSM-BSL P-WR profiles of nondimensionalized static pressure at V50 condition.

Measured and computed V_x profiles in the combustion chamber are compared in Fig. 5.25. An overall good agreement of experimental measurements and numerical results is observed. At the axial position E1 (left plot) close to the nozzle, a fairly good agreement is observed, with some discrepancies arising only in the region around the centerline ($Y/d_n = 0$), where the numerical model overpredicts the measured V_x profile. The agreement improves further moving downstream, as visible in the middle and right plots, comparing measurements and simulations at positions E2 and E3, respectively. Comparing the three subplots of Fig. 5.25 to those of the V90 regime reported in Fig. 5.20, highlights that also in the V50 condition all V_x profiles have a positive Y offset, indicating a lack of axial symmetry of the flow in the combustion chamber.

5.7 Conclusions

The main features of the cold flow physics of a non-premixed industrial gas burner at full and partial load have been investigated by means of RANS CFD, and flow

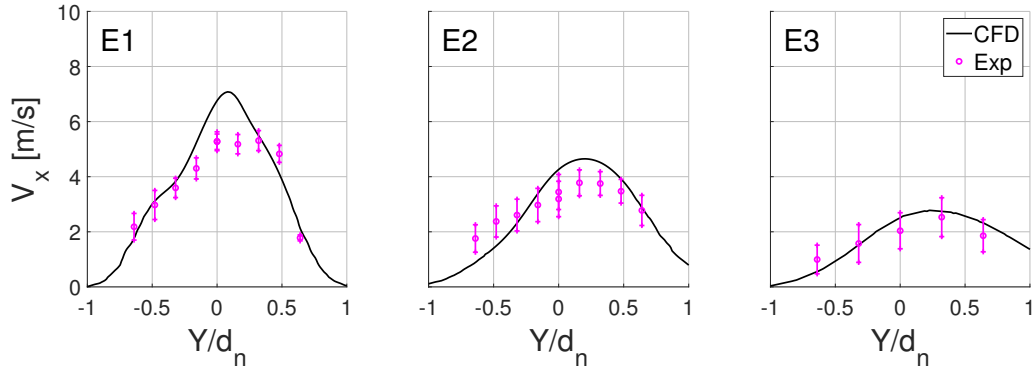


Figure 5.25: Measured and RSM-BSL P-WR V_x profiles on transversal lines E1, E2 and E3 in combustion chamber at condition V50.

measurements taken in a full scale test rig have been used for CFD validation. Parametric CFD analyses aiming at assessing the impact on the computed solution of *a*) inflow BC type (imposed velocity map or total pressure), *b*) resolution of wall-bounded flows (wall functions or integration down to walls), and *c*) turbulence closure ($k - \omega$ SST, RSM-BSL or RSM- ϵ models) have been carried out.

At both operating conditions, the flow field is dominated by highly 3D flow phenomena, including: *a*) a strong deviation of the flow field in the burner case until downstream of the nozzle exit from the axisymmetric pattern, due to a 90° turn of the flow between the air admission duct and the burner, *b*) a system of large secondary vortices caused by the abrupt change in cross sectional area at the end of the air inlet duct, *c*) a separation bubble at the beginning of the nozzle inlet duct, due to the flow arriving from the air admission duct being orthogonal to the nozzle inlet duct, and *d*) flow recirculation pockets caused by forward and backward facing steps on the inner walls of the entire system. In the partial load condition, the overall flow field pattern is made more complex also by the stalled flow pocket around the admission valve, and the two air jets between the valve ends and its bounding walls.

Overall good agreement of CFD results and experimental data has been observed at both operating conditions using the RSM-BSL turbulence model with imposed total pressure at the inlet of the air admission duct, and integration of the governing

equations down to the wall to resolve the near-wall flows.

The analysis of the solution sensitivity to the resolution of the wall bounded flows and the inflow BC type, carried out using the $k - \omega$ SST model, show that, at the full load operating condition, the largest deviations from the measured data are observed when using wall functions and imposing the inlet total pressure. At the partial load condition, the four solutions are relatively close to each other and in fairly good agreement with measured data. Some differences between the air mass flow rates computed with different set-ups suggest that a more precise method for defining \dot{m}_{air} would be best for the case with combustion included. This is because an inaccurate definition of \dot{m}_{air} in such a case would lead to an inaccurate definition of fuel to air ratio, which in turn may lead to significant differences in the flow field.

Comparative analyses of the four solutions of the full load condition, indicate that the deviation of the solution with imposed inlet pressure and using wall functions from the other three solutions may be due to both the inadequacy of the wall function approach to handle flow separation, and the sensitivity of the velocity field to local flow separations being larger when imposing the total pressure rather than the velocity at the inlet of the air admission duct. The observed flow separations occur only in localized regions, one could refine the near-wall grid and resolve BLs only in separated flow regions, and use wall functions elsewhere. This hybrid set-up would enable achieving reduced computational costs and overall adequate solution fidelity.

The improvement of the agreement of simulations and measurements obtained by using RSM may not seem sufficiently large to justify its increased computational cost over that of two-equation eddy viscosity models. However, available literature shows that RSM is better suited than eddy viscosity models to predicting turbulent diffusion flames. This holds also for gas burners notably simpler than the industrial gas burner considered herein, for example purely cylindrical combustors with fuel and oxidizer forming two coaxial non-swirling flows [106, 41]. Therefore, the RSM-BSL closure is deemed to be a well suited method for the follow-on analysis of the

reactive flow of the considered burner. Nevertheless, burner design studies have also highlighted the potential benefits that optimizing certain burner flow patterns may have on improving combustion efficiency and reducing pollutants [135, 21]. In design optimization, which typically requires analyzing a large number of system variants, computationally more affordable eddy viscosity RANS set-ups also play an important role in the initial phase of burner design optimization.

Chapter 6

Combustion analysis of industrial gas burner

This chapter aims to develop an experimentally validated computationally affordable RANS CFD methodology for the analysis and design of industrial gas burners with a particular focus on NO_x emissions. The objective of the analyses herein is two-fold: on one hand, it is to investigate the complex fluid dynamics and NO_x formation of an industrial gas burner, supporting the findings on its flow physics with measurements; on the other hand, the objective is to present parametric analyses of the simulation set-up, focusing on the approach adopted for NO_x modeling, which is achieved via the simplified method or the FGM scalar transport method. The investigation follows the work in Chap. 5, which focused on the nonreactive flow of the same burner studied herein and provided guidelines on the best choices in RANS CFD simulations for such application. The burner is designed to operate in continuous industrial processes with a firing range from 12 to 120 kW. The flow simulations and measurements of this study refer to four load conditions ranging from 41.7 to 87.5 kW. The main novelty of this study is the investigation of flame and NO_x formation physics of a non-premixed industrial gas burner, and its dependence on the operating condition. Moreover, a correction to the FGM scalar transport model for NO is proposed to enable accounting for the effect of non-adiabatic phenomena

in NO formation without increasing the FGM look-up table dimensionality. The experimental phase of this study utilizes a full-scale test rig designed to replicate the operating conditions of the gas burner in production. This ensures that the analyses presented apply to both the scientific and industrial communities within this sector.

The outline of the chapter is as follows. Section 6.1 provides a brief description of the industrial gas burner which is detailed in Chap. 5 and presents the test rig and experimental set-up. Section 6.2 describes the CFD methodology, defines the physical domain, grids, and BCs, and assesses the grid independence of the CFD solutions for the gas burner. Section 6.3 presents the results of this study: first, the temperature field is investigated; then the main features of the flow field responsible for NO_x formation in the system are presented and discussed. Finally, Section 6.4 provides a summary of the study.

This chapter is an adapted version of a part of the work in Ortolani et al.[83].

6.1 Test case and experimental rig

The industrial gas burner investigated in this study is extensively described in Chap. 5. This section summarizes this test case, and describes the experimental rig and the measurement set-up.

The outer geometry of the burner, shown in Fig. 6.1a, consists of a case containing part of the nozzle. A fan provides the airflow supply which is regulated by a throttle valve located before the case. The nozzle consists of a conical part surrounded by a coaxial cylinder with external diameter of 125 mm. The cone has several holes distributed in a periodic pattern. Figure 6.1a also highlights the presence of a flame detector. The flow path schematic is shown in Fig. 6.1b. After entering the case, the stream of fresh air turns by 90° and splits into multiple coaxial streams. The innermost stream, indicated by the central black arrow, flows in a tube whose axis lays on the centerline of the nozzle. This stream then passes through the nozzle

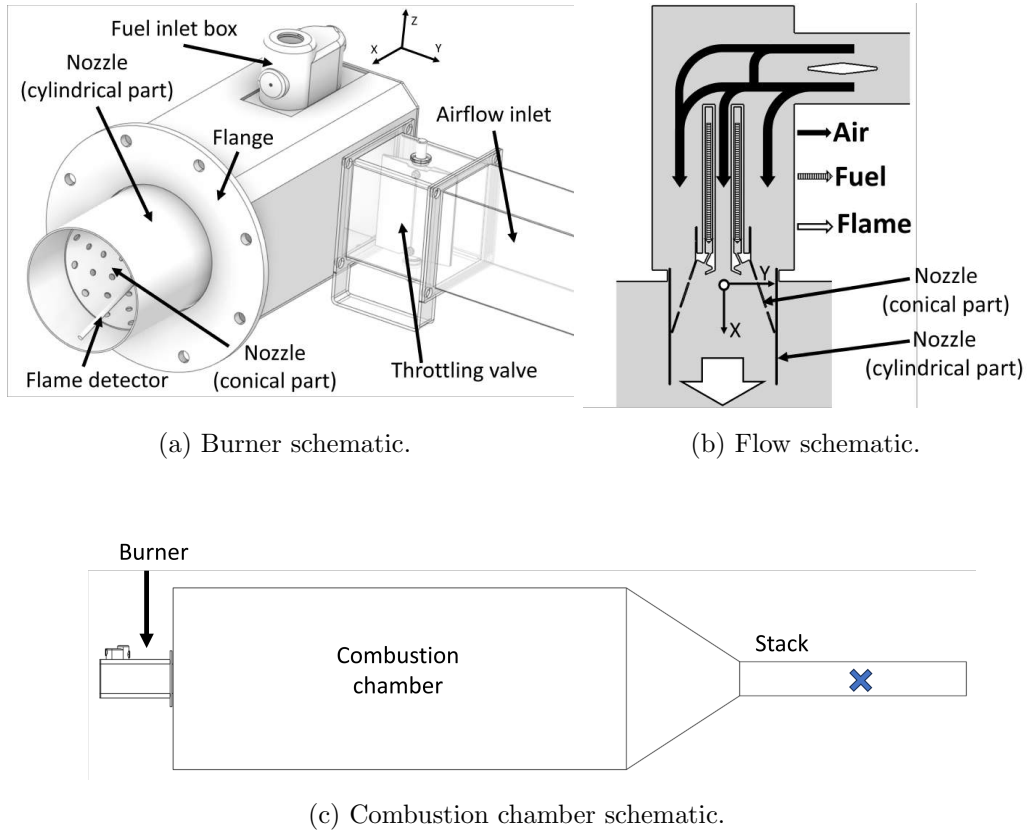


Figure 6.1: Burner and flow schematic.

and feeds the flame. The remaining air reaches the flame through the holes on the conical part of the nozzle, a gap between the internal face of the cylinder of the nozzle and the cone, and a small gap between the external face of the cylinder of the nozzle and the burner case. The fuel stream follows the path of the striped arrows in Fig. 6.1b and mixes with the air directly in the nozzle. Figure 6.1b also shows the origin and orientation of the reference frame used in the analyses below.

In the experimental rig of this study, the flange shown in Fig. 6.1a is bolted to the combustion chamber, as sketched in Fig. 6.1c. The combustion chamber is cylindrical, and has length of 2 m and diameter of 0.8 m. A converging duct following the combustion chamber connects the chamber to the 0.15 m diameter-flue gas stack. The converging duct is 0.5 m long. The combustion chamber, converging duct, and stack are made of 304L stainless steel.

The quantities measured at the inlets of the system are fuel mass flow rate, fuel static temperature, air volume flow rate, air static temperature, air barometric pressure, and air relative humidity. Those measured at the outlet of the system are flue gas static temperature and dry mole fraction of NO and NO₂.

The adopted fuel is the G25 test gas by BOC [10], made up of 86% methane and 14% nitrogen by volume. Fuel mass flow rate and static temperature are measured with a Coriolis mass flow meter, namely the DN8 F300 Promass Flow Meter [27] by Endress+Hauser. The meter is bolted in series to the system of pipes leading to the fuel inlet box shown in Fig. 6.1a. The measuring range of the meter is from 0 to 10 Kg/h. In the measurements of this study, the uncertainty on the measured fuel mass flow rate varies between $\pm 0.86\%$ for the lowest mass flow rates to $\pm 0.41\%$ for the highest ones. The static temperature range of the meter is from $-50\text{ }^{\circ}\text{C}$ to $150\text{ }^{\circ}\text{C}$, and the uncertainty close to ambient temperature, which is the region of interest of this study, is $\pm 0.2\text{ }^{\circ}\text{C}$. The meter returns the instantaneous values of the mass flow rate and temperature with a sampling frequency of 0.2 Hz.

The air volume flow rate and static temperature are measured with the LCA501 digital rotating vane anemometer [47] by TSI Incorporated. The meter is positioned with an aircone flow hood on the inlet section of the centrifugal fan. The anemometer, which has a diameter of 0.1 m, measures the cross-section averaged velocity, and returns the volume flow rate. The measuring range is from $5.9\text{ m}^3/\text{h}$ to $703.8\text{ m}^3/\text{h}$. In the range of measured values of this study, the uncertainty on the measured air volume flow rate varies between $\pm 1.44\%$ at the lowest flow rates and $\pm 1.37\%$ at the highest rates. The temperature measuring range is from $5\text{ }^{\circ}\text{C}$ to $45\text{ }^{\circ}\text{C}$, with an accuracy of $\pm 1.0\text{ }^{\circ}\text{C}$. The anemometer is set so that a sample is composed of time-averaged values of the measured quantities over 30 s.

The air barometric pressure and relative humidity are measured with the Testo 622 thermo-hygrometer and barometer [97] by Testo SE & Co. KGaA. The accuracy of the absolute static pressure measure is $\pm 3\text{ hPa}$, while that of relative humidity is $\pm 2\%$ RH. Since these quantities vary very slowly during the testing period, thus a

single reading is taken for every run.

The air mass flow rate is calculated from the aforementioned measurements. The air density is calculated using the ideal gas law considering a mixture of dry air and water vapor. The composition of dry air is assumed to be 79% N₂ and 21% O₂ by volume. The mole fraction of water vapor is computed from the measured relative humidity and temperature. Considering the accuracy of the flow meter, thermo-hygrometer and barometer, the overall uncertainty on the measured mass flow rate varies between $\pm 2.19\%$ for the lowest air flow rates and $\pm 2.13\%$ for the highest ones.

The flue gas static temperature and composition are measured with the KANE 988 Flue Gas Analyzer [52]. Due to the high temperatures reached by the flue gas, the CHSP5 285 mm high-temperature probe [51] is used. The probe is positioned on the centreline of the stack, which is reached via a hole set 0.56 m from the end of the converging duct. The position of the probe is highlighted with an X in Fig. 6.1c. The temperature measuring range is from 0 °C to 1100 °C with an accuracy of ± 0.5 °C. The measuring range of NO is from 0 to 5000 ppm_{v,d}, while that of NO₂ is from 0 to 1000 ppm_{v,d}. For the performed measurements, the uncertainty on the recorded NO and NO₂ concentrations is ± 5 ppm_{v,d}. The Flue Gas Analyzer is set so that a single sample consists of a time-averaged value of NO and NO₂ over 30 s. As the flue gas is dried before entering the gas sampling line, all experimental data are given on a dry base.

All measurements are carried out for four tests by varying both fuel and air mass flow rates, thus changing power output and equivalence ratio. The equivalence ratio had to be changed as it was found that low-power conditions needed a higher excess of air to keep a stable flame. The highest power output for which the test was performed is 87.5 kW. The lowest power output for which the test was performed is 41.7 kW.

In each test set, the burner is turned on, and all measured quantities are monitored until they stabilize. When the readings are stable, the time history of the fuel flow rate is recorded, together with 3 samples of the flue gas composition

and temperature and at least 4 samples of air flow rate. The measured air and fuel flow rates are time-averaged. Each test has a duration of approximately 10 minutes. The resulting values serve as boundary conditions for the CFD simulations.

6.2 Set-up of CFD simulations

This section describes all aspects of the CFD methodology, including the physical domain, the computational grids, and the boundary conditions. It also presents results of the assessment of the grid dependence of the computed gas burner flow field on the level of mesh refinement, aiming to determine the optimal refinement for a grid-independent solution.

The physical domain for the industrial burner simulations is shown in Fig. 6.2. The domain includes throttle valve, burner case, nozzle, ducts for fuel supply, cylindrical combustion chamber, converging duct, and stack. The spark plug, the flame sensor and the bolts are not included in the physical domain for simplicity. The air and fuel inlet boundaries and the outlet boundary are indicated in Fig. 6.2.

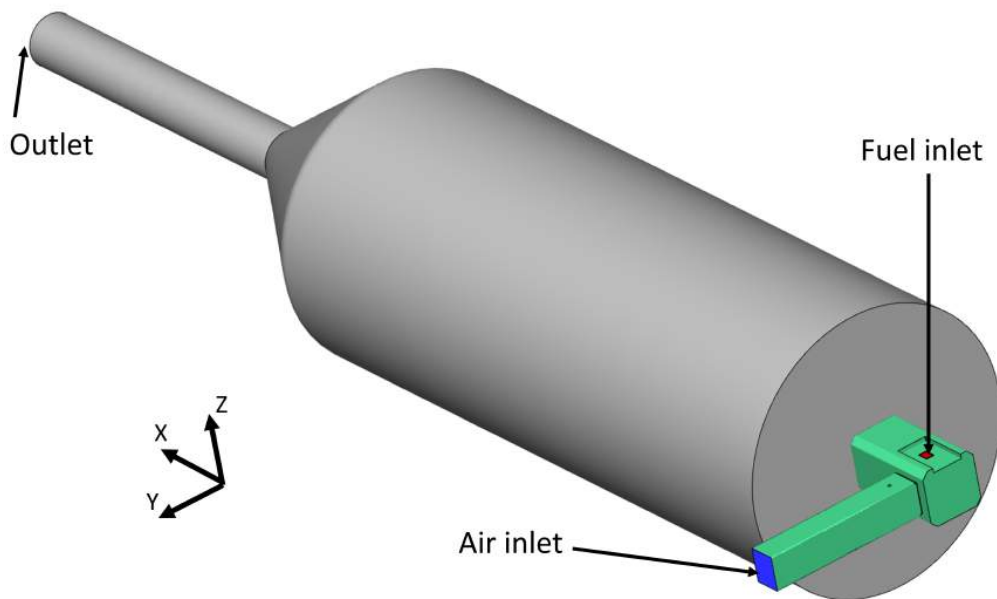


Figure 6.2: Industrial burner physical domain.

All simulations are performed with an URANS RSM approach, since converged solutions could not be obtained with steady RANS analyses. The LES method was not adopted because, with the available computer resources, this approach would have required unacceptable runtimes. As in the validation test case presented in Chap. 4, the RSM model with baseline ω equation is used for turbulence modeling in all URANS analyses below. In 3D, the RSM approach requires solving a transport equation for all the six distinct components of the Reynolds stress tensor τ_{ij} .

The approach followed to model the mixture temperature, physical properties, and chemical composition is the same used for the validation test case in Chap. 4 and described in Chap. 3. The flamelet equations are solved again using the GRI-Mech 3.0 kinetic mechanism [104]. Also in the industrial burner case, the fresh air humidity is taken into account in the flamelets generation. The approach for radiation modeling is the P-1 model extended to account for TRI via a UDF. Differently from the validation test case, the mean beam length for the computation of the absorption coefficient κ_a has been computed following the guidelines of [101], using volume and surface of the cylindrical combustion chamber.

The models adopted for NO formation are the same used in Chap. 4 and described in Chap. 3. The oxygen atom concentration in the method M3 is computed only with the partial equilibrium assumption, as it was concluded in Chap. 4 that, in the context of RANS, it yields more accurate results than using values obtained from the look-up table. The set-up labeled 'M3' in this chapter is the same as the set-up labeled 'M3 - Part. Eq. [O]' in Chap. 4.

The measured mass flow rates of air and fuel are prescribed at the two inlet boundaries. Zero gauge static pressure is prescribed at the outlet boundary. All the other boundaries are treated as viscous walls. The simulations include modeling of radiation and convection heat transfer across the walls wetted by the hot burnt gases (boundaries in gray in Fig. 6.2), which are labeled 'non-adiabatic walls'. The non-adiabatic walls are the combustion chamber, converging duct, and stack, and their emissivity is set to 0.21, the value measured in [116]. The convective

heat transfer coefficient of the non-adiabatic walls is computed according to the guidelines of [111], which considers natural convection around horizontal cylinders. The ambient temperature at the exterior of the system is set equal to that measured at the airflow inlet. All the other walls are treated as adiabatic.

As in the validation test case, the COUPLED algorithm is used for the numerical integration, and the convective terms of all equations are discretized with a second-order upwind scheme. Second-order finite-differencing is used for all diffusion terms. The URANS simulation uses a dual time-stepping approach with a first-order implicit scheme for time discretization. The time-step is 0.05 s and, in most simulations, 50 subiterations are performed at each time step. In some cases, 60 or 80 subiterations are needed to improve convergence. After the simulations reach statistically stationary flow fields, averages are computed over a period of 60 s.

All grids are high-quality hybrid unstructured meshes generated with ANSYS Fluent Meshing. Figure 6.3 shows the longitudinal section of a mesh with medium refinement. Polyhedral cells are used both close to the boundaries, where the geometrical complexity of the physical domain requires their use, and in interior flow regions where they serve as connectors between mesh portions with different refinements. Regular hexahedral cells are used to fill the remaining part of the physical domain. The grid is such that wall functions are used only in regions of well-behaved near-wall flow. Based on the observation in [82] (Chap. 5), an inflation layer that allows solving the boundary layer down to the wall is grown only on critical wall patches. This approach allows achieving an optimal trade-off of fidelity and computational cost.

The meshing approach followed for the industrial burner is rather different from that used for the validation case. The simple geometry of the Sandia flame D fluid domain allows adopting a multi-block mesh with structured blocks in the flame core region. This grid type enables one to select and optimize all geometric parameters, such as the expansion rate of the cell volumes. The resulting minimization of the cell count, achieved without compromising the grid quality, is paramount for reducing

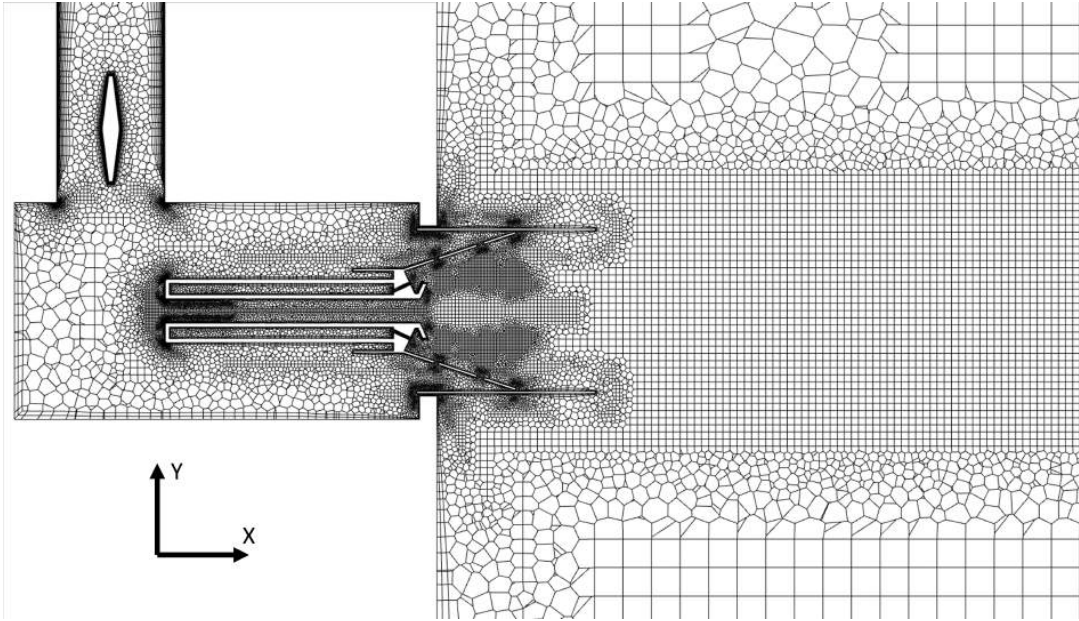


Figure 6.3: Industrial burner mesh.

the computational cost of the LES simulation. By contrast, the geometric complexity of the industrial gas burner's physical domain is more conveniently handled by a hybrid unstructured mesh generator, which handles in a more automated and user-friendly fashion the optimization of the grid quality and its cell count.

Three meshes with increasing refinement are generated applying a 1.3 refinement factor on the size of the cells of the coarser level. The three meshes, labeled 'crs.', 'med.', and 'fin.', have 2.2, 3.2, and 5.1 million cells, respectively. A mesh sensitivity analysis is carried out for the operating condition with the highest power output to assess the grid independence of the solution. The quantities that are monitored are those of interest in this study: the flue gas temperature and the NO concentration at the stack. Since the simulation with the coarse grid did not converge, only the results with the medium and fine grids are available with the set-up described above. The simulations with the three grids were instead all successful when excluding the effect of TRI, which was found to be the cause of instabilities with the coarse grid.

Table 6.1 reports values of flue gas properties computed on the coarse, medium, and fine refinement grids, respectively. Columns two to five report results obtained

neglecting TRI. The second column provides the temperature; the third, fourth, and fifth columns provide the value of NO emissions computed with methods M1, M2 and M3, respectively. Columns six to nine report corresponding results obtained taking TRI into account. One notes that neglecting TRI, the values of the temperature

Refinement	No TRI				TRI			
	T [K]	NO [ppm _{v,d}]			T [K]	NO [ppm _{v,d}]		
		M1	M2	M3		M1	M2	M3
crs.	974.1	361	237	84	-	-	-	-
med.	998.1	384	247	60	967.3	383	231	54
fin.	998.6	384	243	58	966.7	384	236	51

Table 6.1: Flue gas temperature and NO mass fraction computed with different levels of grid refinement

computed with medium and fine grids are very close, and their difference is 0.05%. The temperature computed with the coarse grid is 2.4% lower than that computed with the medium grid. The NO emissions computed with medium and fine grids and method M1 are the same, while that computed with the coarse grid is 6% lower. The value of NO emissions computed with the medium grid and method M2 is 1.6% higher than that computed with the fine grid, while that computed with the coarse grid is 2.5% lower. The value of NO emissions computed with medium and fine grids and method M3 differ by 2 ppm_{v,d}, a value which is lower than the measurement uncertainty, while that computed with the coarse grid is 24 ppm_{v,d} higher than that computed with the medium grid. The differences in the results obtained with medium and fine grids taking TRI into account are similar to those obtained neglecting TRI. These results indicate the suitability of the medium grid to properly resolve the flow physics of the considered industrial gas burner for the quantities of interest in this study.

6.3 Results

This section presents the main experimental and CFD analyses of the considered industrial gas burner. Measured and CFD data are compared, and the flow field is discussed for two conditions, that with highest and that with lowest power output. The discussion first focuses on the temperature field, and then moves to the NO_x analysis. All CFD results reported in this section are time averages of the URANS simulations.

Table 6.2 defines the tested conditions. The first column indicates the label that will be used in this discussion to reference different conditions. The second column indicates the power outputs P , while the third column provides the overall equivalence ratio Φ in the burner. As reported in Sec. 6.1, the overall equivalence

Condition	P [KW]	Φ
A	41.7	0.36
B	61.3	0.49
C	74.6	0.56
D	87.5	0.65

Table 6.2: Power and overall equivalence ratio of the studied conditions.

ratio was changed among the considered regime because the low-fire conditions needed a higher excess of air to keep a stable flame. The ratio between the highest and the lowest power outputs is approximately 2:1.

6.3.1 Temperature field

Figure 6.4 shows a comparison between computed and measured flue gas static temperature. The temperature is computed using either CFD simulations ('CFD') or adiabatically ('Adiabatic Temp.'). The adiabatic temperature is obtained neglecting radiation and convective heat transfer, and assuming that full equilibrium of the reaction is reached at the stack. In particular, the adiabatic temperature is computed

based on the mixture fraction of the mixed fuel and oxidizer streams and the equilibrium adiabatic flamelet. As no flame extinction is observed and the flue gas is close to equilibrium in all operating conditions, the adiabatic temperature is of interest to quantify the effect of non-adiabatic modeling on flue gas temperature.

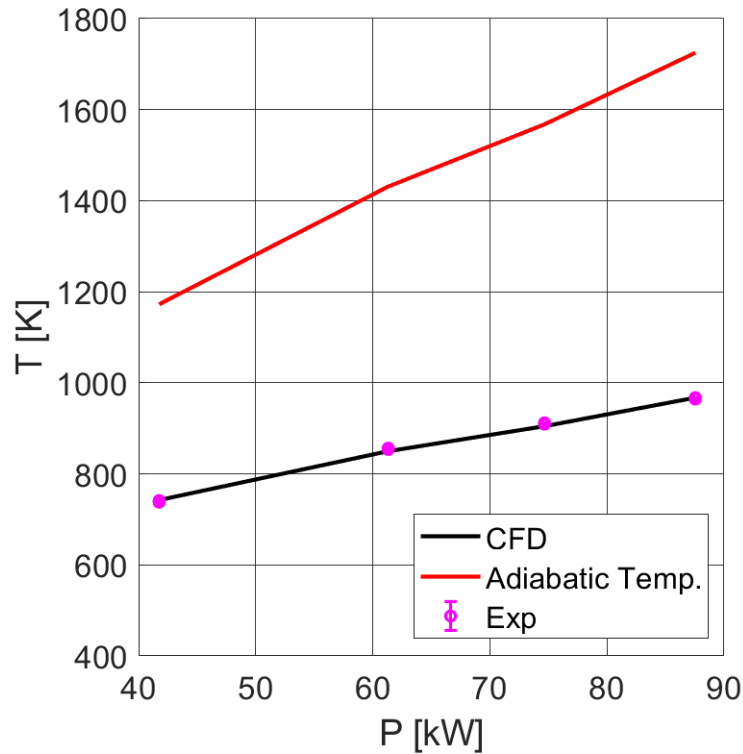


Figure 6.4: Measured and computed static temperature at the stack

Each measured point in the plot is computed as the mean of three 30 s time averages (or samples). The maximum deviation between a single sample and the plotted point for a specific condition is $<0.3\%$, showing low variability in the samples. CFD accurately predicts the flue gas temperature at all conditions. The difference between CFD and measured temperatures varies from a minimum of 0.13% at operating condition D to a maximum of 0.65% at operating condition B. Accounting for TRI is found to be relevant to improving the accuracy of the results. The temperature computed by the simulation that neglects TRI, which

is performed only for operating condition D and reported in Tab. 6.1, is found to be 3.32% higher than the measured value. The comparison of adiabatic and CFD temperatures highlights the impact of radiation and convective heat transfer. The difference between the two computed temperatures increases from 430.1 K to 757.5 K going from operating condition A to D. As expected, the heat lost due to the combination of radiation and convection heat transfer increases with the temperature in the system. Given the excellent agreement between CFD and measured data, it is possible to conclude that the set-up used in this study can accurately quantify non-adiabatic phenomena' effects on the gas temperature. The significant difference between adiabatic and CFD temperatures shown in Fig. 6.4 suggests that non-adiabatic phenomena may have a stronger impact on NO formation than in the case of Sandia flame D (Chap. 4), which is a non-luminous flame and has a very small radiative heat loss.

Figure 6.5 shows the contour plot of Favre-averaged temperature on the planes $Z=0$ and $X=0.18$ m for the operating conditions A and D. The maximum temperatures reached in operating conditions A and D are 1918.5K and 2049.3K, respectively. One sees from Figures 6.5a and 6.5c that the high-temperature regions of the two operating conditions have significantly different sizes. Defining the high-temperature region as that characterized by $\tilde{T} > 1800\text{K}$, that of condition A extends in the X direction for 30.5 cm. The high-temperature region of condition D is nearly three times longer, as it extends for 86.7 cm. The high temperatures shown in Fig. 6.5c suggest that NO_x formation via the thermal path may be the most significant at operating condition D. The contribution of other paths may be also significant at operating conditions A, as the temperatures shown in Fig. 6.5a are significantly lower. Both the maximum temperature and the size of the high-temperature region are important factors in the formation of NO. The former is important because of the high sensitivity of NO formation to temperature, while the latter is important because of an increment in the residence time of the gases in high-temperature regions.

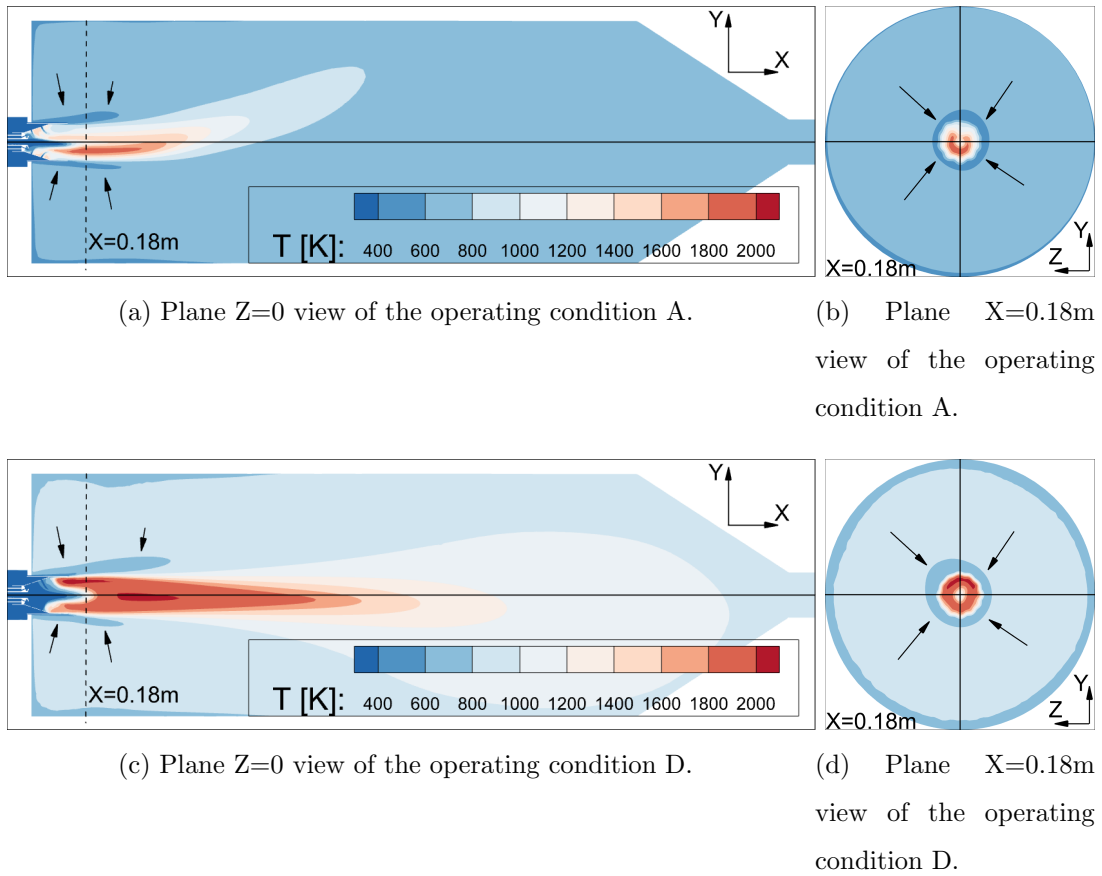


Figure 6.5: Static temperature contour plots on the $Z=0$ and $X=0.18\text{m}$ planes for the operating conditions A and D.

Figures 6.5a and 6.5b show that at operating condition A the flame is asymmetrical. The flame is asymmetric with respect to the plane $Y=0$, but symmetric with respect to the plane $Z=0$. This pattern was visually observed during the experimental tests. The symmetry axis of the nozzle and combustion chamber is drawn in Fig. 6.5a to best visualize the flame asymmetry. The highest mean temperatures are found in the region $Y<0$, while never arising above 1800K in the region $Y>0$.

Figures 6.5c and 6.5d show that the flame is asymmetrical also at operating condition D. As at condition A, the flame is asymmetric with respect to the plane $Y=0$ and symmetric with respect to the plane $Z=0$. Also at this regime, this pattern

was observed during the experiments. Figure 6.5c shows that the high-temperature region is slightly tilted toward negative values of Y . There are two regions where the mean temperature reaches values higher than 2000 K. The first region is in the core of the flame, which is located about 24 cm after the nozzle and close to the axis of the chamber. The second region is found close to the nozzle exit section, at positive values of Y . The flame asymmetry can be explained by the features of the oxidizer flow upstream of the nozzle, and can be traced back to the 90° turn of the flow after the valve shown in Fig. 6.1b. This was observed and explained in depth in [82], where the cold flow field in the system was analyzed both numerically and experimentally for different load conditions.

In both operating conditions, a significant fraction of the oxidizer flow enters the combustion chamber via a gap between the cylindrical part of the nozzle and the burner case. This is a low-temperature annular stream entering directly the combustion chamber and surrounding the flame, which is indicated by the black arrows in all the plots of Fig. 6.5. The fresh stream cools down the cylindrical part of the nozzle. This oxidizer stream surrounding the flame consists of 27.5% and 27.6% of the total air mass flow rate in operating conditions A and D, respectively. This stream of oxidizer will be referred to as the 'oxidizer annular stream' in the following discussion.

6.3.2 NO_x field

Figure 6.6 compares computed and measured NO_x emissions expressed ppm by volume on a dry base ($\text{ppm}_{v,d}$). Figure 6.6a shows the comparison of NO emissions, whereas Fig. 6.6b shows that of NO_2 emissions. The value of NO is computed with methods M1, M2 and M3. As for the case of the static temperature, the variability between measured NO_x samples is very low. The maximum deviation between a single sample and the averaged value of all samples for a specific operating condition is $<1\text{ppm}_{v,d}$ both for NO and NO_2 . The measured NO emissions increase for operating conditions characterized by a higher power output. As the equivalence

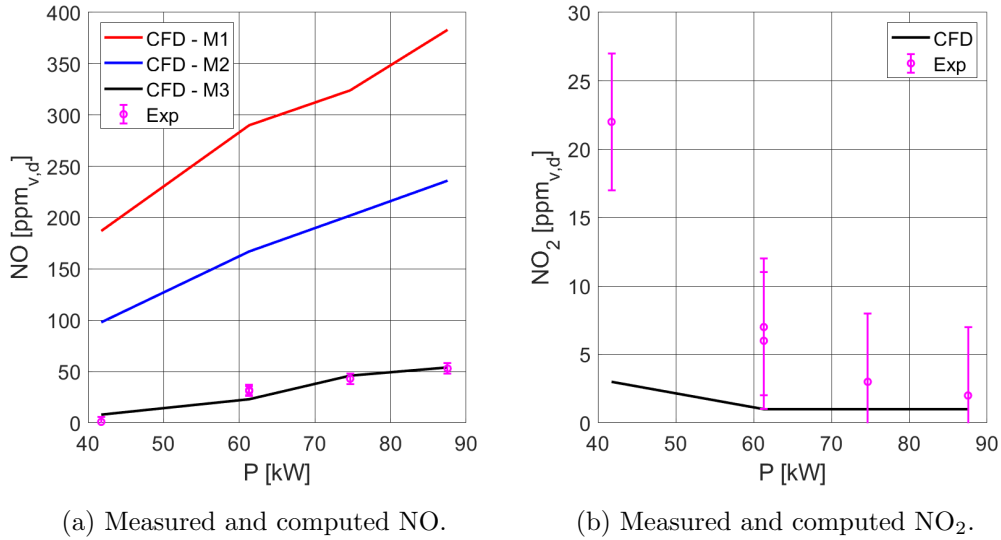


Figure 6.6: Measured and computed NO_x at the stack.

ratio of the lean mixture increases, so does the temperature in the combustion chamber, which leads to an increased formation of NO via the thermal path. In contrast, the emission of NO₂ increases for operating conditions characterized by a lower equivalence ratio: as the concentration of O₂ in the burnt gases increases, it promotes the oxidation of NO into NO₂.

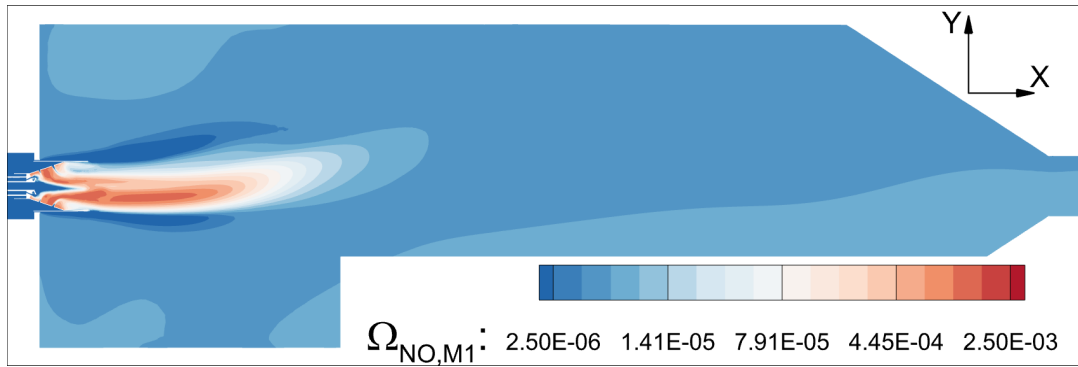
Similarly to the validation test case, methods M1 and M2 significantly over-predict the production of NO. The comparison of the results obtained with the two methods shows that accounting for non-adiabatic phenomena has a significant effect, as the NO emission predicted with M2 is 37.6% to 47.6% lower than that predicted with M1. As for the validation test case, part of the difference between the prediction of these two methods and the experiments may be explained by the choice of the type of flamelet [131]. Method M3 gives better predictions of the NO formation than methods M1 and M2 and is in overall good agreement with experimental data. At operating conditions C and D, where the thermal path dominates due to the high temperatures, the NO emissions computed via M3 are within the uncertainty range of the measured value. The comparison of M3 and experiments worsens at operating

conditions A and B, which may be due to two reasons. Firstly, temperatures in the combustion chamber at regimes A and B are lower than those at regimes C and D, and the high-temperature region is smaller. This suggests that the thermal path in such operating conditions may be less significant, while the prompt and N_2O -intermediate mechanisms may become more relevant. Since the analysis in Chap. 4 has shown that the modeling strategies for these two paths are subject to higher inaccuracies than that of the thermal path, it is plausible that these shortfalls result in mispredictions of overall NO formation at regimes A and B, dominated by the two aforementioned NO formation paths. Secondly, inspecting both plots of Figures 6.6 highlights that the deviation between M3 and measured NO is noticeable when the emissions of NO_2 increase. This may occur because method M3 does not account for the oxidation of NO into NO_2 , leading to inaccuracies when such a reaction is relevant. Methods M1 and M2 account for the oxidation of NO, and one sees that at lower power they predict the trend of NO emissions better than method M3. Figure 6.6a shows that the slope of the measured NO emission trend is steeper between $40 \text{ kW} < P < 60 \text{ kW}$ than between $60 \text{ kW} < P < 75 \text{ kW}$. This is correctly predicted by methods M1 and M2, while it is inverted by method M3.

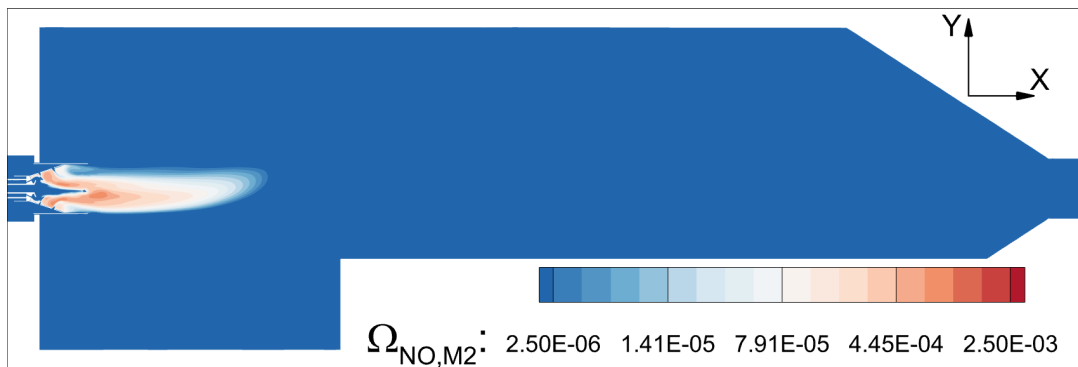
Figure 6.6b shows that the trend of NO_2 decreasing with increasing power is correctly predicted by CFD, but there is a significant difference between measured and computed emissions. Measured NO_2 decreases from 22 $\text{ppm}_{\text{v,d}}$ to 2 $\text{ppm}_{\text{v,d}}$, whereas the computed value decreases from 3 $\text{ppm}_{\text{v,d}}$ to 1 $\text{ppm}_{\text{v,d}}$. This discrepancy may occur because the tabulated source term in the NO_2 equation relies on the molar concentration of NO computed with the flamelet equations, which is notoriously inaccurate (e.g., [130, 37]).

The top, middle and bottom images of Fig. 6.7 shows the contour plot of NO formation rate Ω_{NO} in $[\text{mol}/(\text{m}^3\text{s})]$, computed by methods M1, M2 and M3, respectively. A logarithmic scaling is used for all three contour plots. Due to the significant quantitative difference of the results obtained with method M3 compared to the other two methods, the contour levels of Fig. 6.7c are different from those

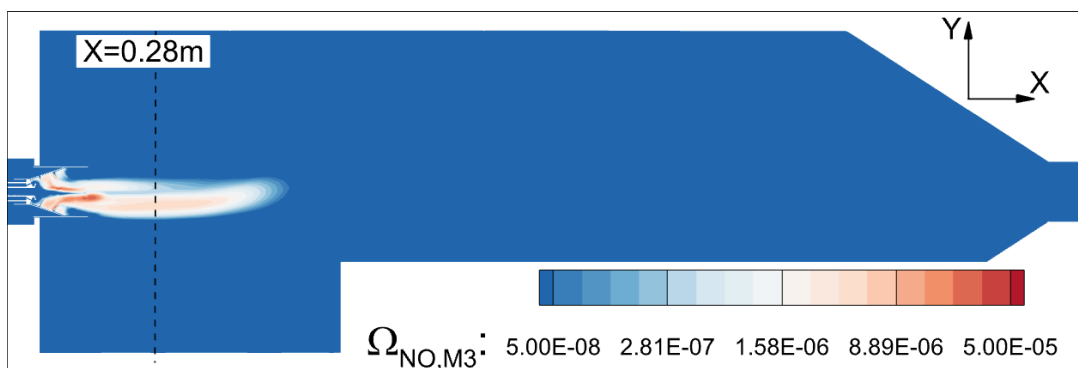
of Figures 6.7a and 6.7b. In all plots, the contour limits are chosen so that the difference between the minimum and the maximum is three orders of magnitude. Comparing Fig. 6.7a with Figures 6.7b and 6.7c highlights the impact of non-



(a) Method M1.



(b) Method M2.



(c) Method M3.

Figure 6.7: NO formation rate contour plots on the $Z=0$ plane for the operating conditions A.

adiabatic phenomena such as radiation heat transfer on NO formation rate. The formation rate computed with method M1, which does not take into account said phenomena, does not drop below the minimum contour level of the figure even when the temperature drops below 800 K (Fig. 6.5a). By contrast, the level of Ω_{NO} computed with methods M2 and M3 drops below such minimum right after the flame. All methods predict that most NO formation in operating condition A occurs in the flame core, where the peak temperatures are experienced. All three methods predict the maximum value of Ω_{NO} to be close to the exit section of the nozzle, with the formation rate gradually decreasing thereafter. Compared with methods M2 and M3, the formation rate computed with method M1 takes longer to decrease after the flame core. The images of Figures 6.7b and 6.7c are qualitatively similar.

Figure 6.8 reports the non-dimensionalized mass flow rate of NO $\dot{m}_{NO,M3}^*$ in the combustion chamber along the X direction, and a set of computed radial profiles of normalized oxygen molar fraction of the dry mixture $X_{O_2,d}$, temperature, and non-dimensionalized NO formation rate $\Omega_{NO,M3}^*$. The figure is useful to better illustrate the NO formation in operating condition A. The analysis is performed with the results of method M3, which is the most accurate. Even though the measurements seem to show that for operating condition A most of NO oxidizes into NO_2 in the combustion chamber, the analysis is useful to understand how NO is formed in the first place.

Figure 6.8a reports the non-dimensionalized mass flow rate of NO in the combustion chamber along the X direction. The NO mass flow rate is computed as follows:

$$\dot{m}_{NO,M3} = \int_{CS} \bar{\rho} \bar{V}_x \tilde{Y}_{NO,M3} \quad (6.1)$$

where CS is the cross-section of the combustion chamber. The value of $\dot{m}_{NO,M3}$ is non-dimensionalized using the maximum value of NO mass flow rate reached in the combustion chamber during condition A. The abscissa axis starts at $X=0.12$ m, which is the location of the exit section of the nozzle. One sees that 30% of the

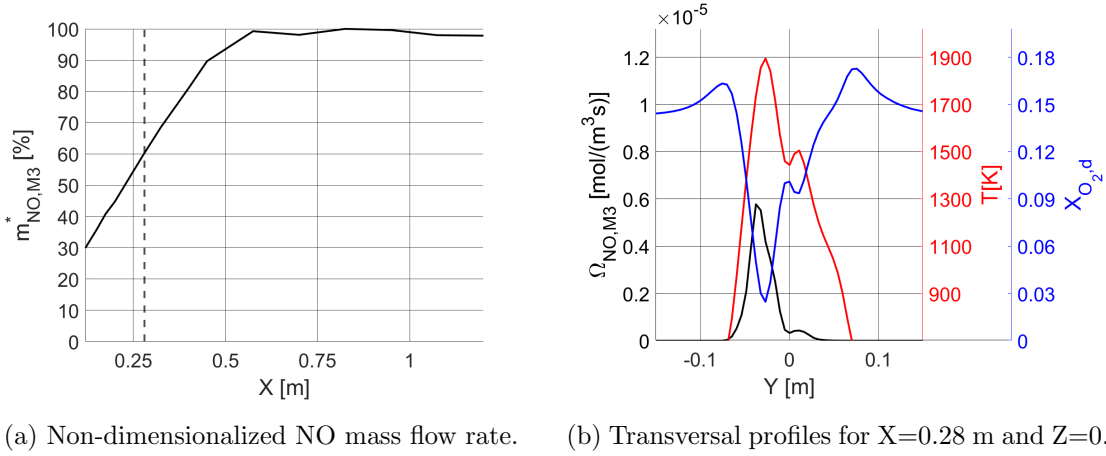


Figure 6.8: Non-dimensionalized NO mass flow rate in the combustion chamber and transversal profiles of normalized oxygen molar fraction, temperature, and non-dimensionalized NO formation rate for operating conditions A.

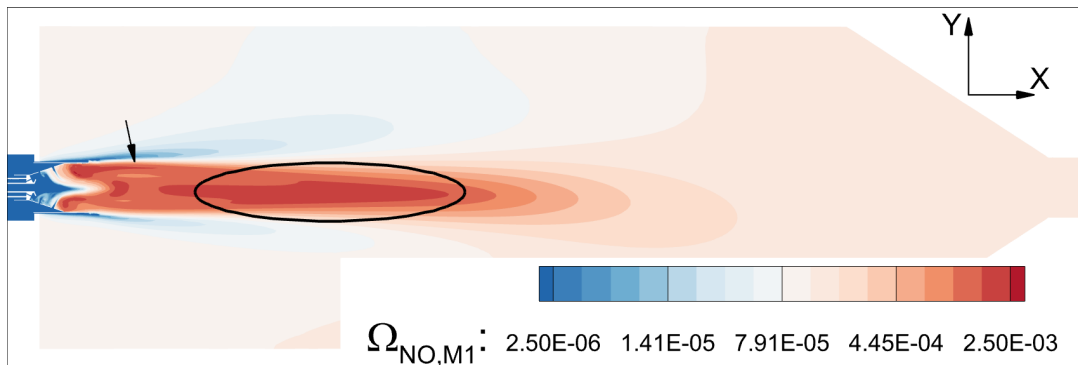
total NO is formed before the exit section of the cylindrical part of the nozzle. NO formation continues at a steady rate for 33 cm (up to $X=0.45$ m), where 90% of NO has formed. The formation rate then decreases, and after $X=0.57$ m the mass flow of NO hardly changes.

Figure 6.8b shows the computed profiles of normalized oxygen molar fraction of the dry mixture $X_{O_2,d}^*$, temperature, and non-dimensionalized NO formation rate. The profiles are those on the line $X=0.28$ m and $Z=0$, whose location is highlighted with a dashed line in Figures 6.7c and 6.8a. The profile of $X_{O_2,d}$ is normalized taking the value of 0.21 as a reference, that is the molar fraction of oxygen in the dry fresh air. The value of $\Omega_{NO,M3}$ is non-dimensionalized taking the value of $1.19 \cdot 10^{-5}$ mol/(m³ s) as a reference, that is the maximum value found in the computed $\Omega_{NO,M3}$ profiles for condition D (Fig.6.10b). One sees that there is a 1900 K temperature peak at $Y=-0.027$ m and a lower peak at $Y=0.011$ m. The $X_{O_2,d}^*$ profile presents valleys where the T profile presents peaks. Around these radial locations, oxygen reacts with fuel causing a local reduction in oxygen molar fraction and increment in temperature. The NO formation rate peaks in the same locations as temperature,

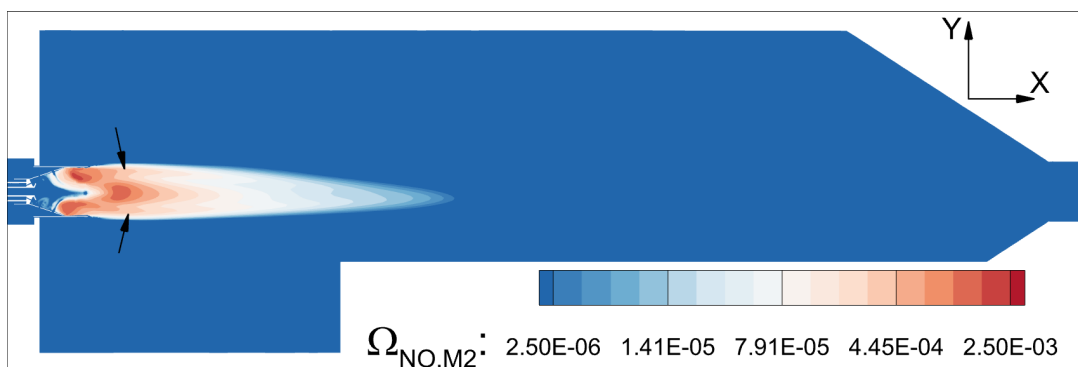
even though the oxygen molar fraction is at its low points in the profile. Figure 6.8b confirms that for operating condition A, most of NO is formed in the core of the flame and that the oxidizer annular stream does not impact NO emissions.

Figure 6.9 has the same structure of Fig. 6.7 and refers to operating condition D. Comparing Fig. 6.9a with Figures 6.9b and 6.9c highlights the impact of non-adiabatic effects at regime D. The level of Ω_{NO} computed after the flame with method M1 is significantly higher than that computed with methods M2 and M3. The difference between adiabatic and non-adiabatic cases in terms of Ω_{NO} field is higher than that observed in Fig. 6.7 for operating condition A. This is expected, because higher temperatures lead to stronger non-adiabatic phenomena. A second significant difference between the predictions of methods M1 and M2 is found towards the end of the flame. In the adiabatic case, the NO formation rate is at its maximum in this region, which is highlighted with an ellipse in Fig. 6.9a. In contrast, the non-adiabatic case does not present such high values of Ω_{NO} in the same region.

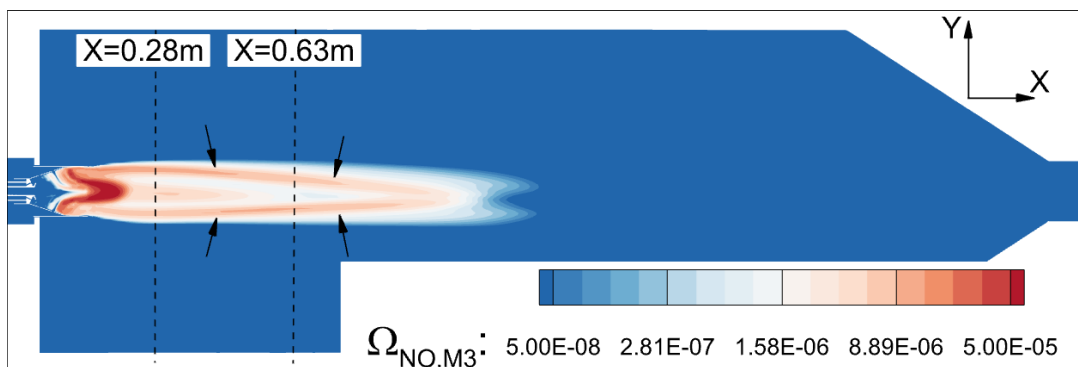
Similarly to the case of operating condition A, the Ω_{NO} field computed with methods M2 and M3 (Figures 6.9b and 6.9c) are qualitatively more similar to each other than either field is to that computed with method M1. Qualitative differences between the M2 and M3 results are more evident for operating condition D than for operating condition A, as the assumptions made in the derivation of method M2 may be overly restrictive. For instance, the assumption of constant c_p computed at the non-adiabatic temperature may lead to inaccuracies when the temperature deviation from the adiabatic case increases. Nevertheless, method M2 shows a significant improvement over method M1. Method M3 yields the best predictions, since its result for the NO emissions at condition D is in excellent agreement with experiments. This good prediction of method M3 may be due to two factors. Firstly, the high temperatures in the flame lead to the thermal path dominating the formation of NO. As seen in Chapter 4, method M3 properly predicts NO formation via the thermal path. Secondly, the emission of NO₂ in condition D



(a) Method M1.



(b) Method M2.



(c) Method M3.

Figure 6.9: NO formation rate contour plots on the $Z=0$ plane for the operating conditions D.

is very low, which makes the effect of NO oxidation negligible.

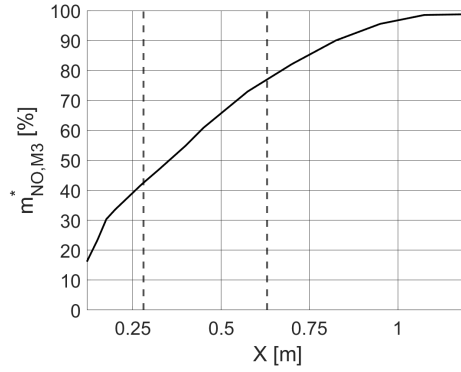
Contrary to condition A, the views of Fig. 6.9 show that all three methods predict an increase in the NO formation rate where the oxidizer annular stream meets the

flame. This is highlighted by the black arrows in all three images of the figure. The effect is evident in the solution of method M3, reported in Fig. 6.9c.

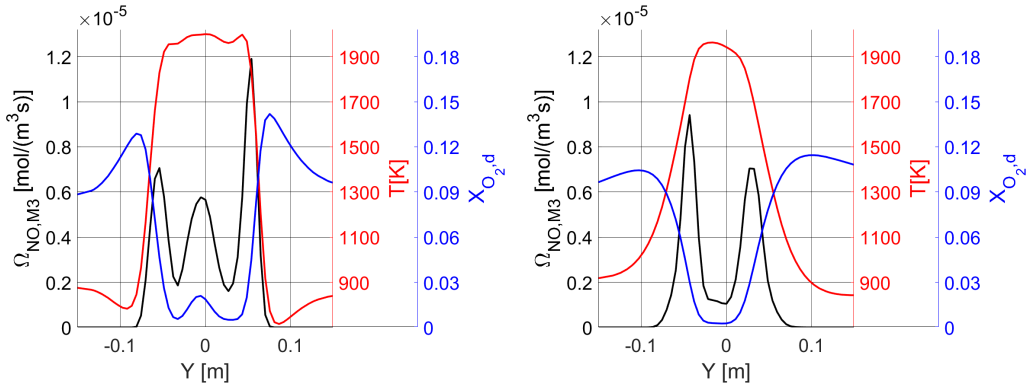
Figure 6.10 reports the non-dimensionalized mass flow rate of NO $\dot{m}_{\text{NO},\text{M3}}^*$ in the combustion chamber along the X direction, and two sets of computed radial profiles of normalized oxygen molar fraction of the dry mixture $X_{\text{O}_2,\text{d}}$, temperature, and non-dimensionalized NO formation rate $\Omega_{\text{NO},\text{M3}}^*$. The figure is useful to better illustrate the NO formation in operating condition D. The analysis is performed with the results of method M3, which is the most accurate.

As for operating condition A, Figure 6.10a reports the non-dimensionalized mass flow rate of NO in the combustion chamber along the X direction. The value of $\dot{m}_{\text{NO},\text{M3}}^*$ is computed with Eq. (6.1) and non-dimensionalized using the maximum value of NO mass flow rate reached in the combustion chamber during condition D. Similarly to Figure 6.8a, the abscissas start at the nozzle exit. One sees that 17% of the maximum NO mass flow rate reached in the chamber is formed in the nozzle. After the nozzle, the non-dimensionalized mass flow rate of NO increases to 30% in 5 cm ($X=0.17$ m). The rapid 13% increase of $\dot{m}_{\text{NO},\text{M3}}^*$ close to the nozzle is due to the high formation rate of NO observed in this region of the flame and seen in Fig. 6.9c. The curve of $\dot{m}_{\text{NO},\text{M3}}^*$ is less steep in the following part of the flame, and its slope remains approximately constant for 28 cm, up to $X=0.45$ m. At this point the value of $\dot{m}_{\text{NO},\text{M3}}^*$ is 60%. In the last part of the flame, NO forms at a rate that gradually decreases, and, from $X=1.08$ m, the value of the non-dimensionalized NO mass flow rate no longer varies significantly.

Figure 6.10b shows computed profiles of normalized oxygen molar fraction of the dry mixture, temperature, and normalized NO formation rate. The profiles refer to the line $X=0.28$ m, $Z=0$, highlighted with a dashed line in Figures 6.9c and 6.10a. At this axial location the value of $\dot{m}_{\text{NO},\text{M3}}^*$ is 42%. The profile of $X_{\text{O}_2,\text{d}}^*$ has three peaks. A peak is on the axis of the combustion chamber and is due to the stream of fresh air feeding the flame from the tube whose axis lies on the axis of the combustion chamber. The other two peaks, which are higher than that on



(a) Non-dimensionalized NO mass flow rate.



(b) Transversal profiles for $X=0.28$ m and (c) Transversal profiles for $X=0.63$ m and $Z=0$.

Figure 6.10: Non-dimensionalized NO mass flow rate in the combustion chamber and transversal profiles of normalized oxygen molar fraction, temperature, and non-dimensionalized NO formation rate for operating conditions D.

the combustion chamber axis, are found at $Y=-0.080$ m and $Y=0.076$ m and are due to the oxidizer annular stream. One sees the presence of an extended region characterized by high temperatures varying between 1960 K and 2000 K close to the axis of the chamber. The temperature rapidly drops in correspondence with the Y position of the oxygen peaks due to the oxidizer annular stream. Similarly to the $X^*_{O_{2,d}}$ profile, the profile of $\Omega^*_{NO,M3}$ has three peaks. The lowest peak is on the axis of the combustion chamber and it occurs where the temperature profile is at its highest and in correspondence with the lowest peak of oxygen molar fraction. The

remaining two peaks of $\Omega_{\text{NO,M3}}^*$ occur at the junction where the zone marked by elevated temperature intersects with the oxidizer annular stream. This result shows that the oxygen provided by the oxidizer annular stream is a crucial element in the formation of NO in operating condition D.

Figure 6.10c is structured as Fig. 6.10b, and the profiles refer to the line $X=0.63$ m, $Z=0$, indicated by the dashed line in Figures 6.9c and 6.10a. At this location the value of $\dot{m}_{\text{NO,M3}}^*$ is 77%. The oxygen from the central tube is completely consumed by the flame. Consequently, the formation rate of NO on the axis of the chamber does not present a peak despite the temperature being >1900 K. Conversely, the peaks found where the high-temperature region meets the oxidizer annular stream are still present. The formation of NO in the last part of the flame is almost completely due to the presence of the oxidizer annular stream.

6.4 Conclusions

The main features of the complex fluid dynamics and NO_x formation of a non-premixed industrial gas burner at different load conditions have been investigated using unsteady RANS CFD and flow measurements performed in a full scale test rig. Temperature and NO_x measurements carried out in the same rig have been used for validating all CFD analyses. The industrial burner has been tested for different conditions with power output varying from 41.7 to 87.5 kW.

This study has included a parametric CFD analysis aiming at assessing the accuracy of different NO_x modeling strategies for computing NO_x emissions. NO formation has been modeled by resolving an additional transport equation for its mass fraction, and the source term of the equation has been computed with three methods: a) the FGM scalar transport approach neglecting the effect of non-adiabatic phenomena on species composition; b) the FGM scalar transport approach with a modification enabling to account for the effect of non-adiabatic phenomena without increasing the look-up table dimensionality and thus burden on

the computer memory; c) a sum of formation rates computed with simplified models for thermal, prompt, and N₂O-intermediate paths. Only one method has been used to model NO₂ formation, which is the FGM scalar transport approach neglecting the effect of non-adiabatic phenomena on species composition.

The flow field of the industrial gas burner at the highest and lowest power has been analyzed. Maximum temperatures reach 1918.5 K to 2049.3 K depending on the operating conditions. The high-temperature region (>1800 K) at the highest power operating condition is nearly three times longer than that at the lowest power operating condition. The temperature fields suggest significant NO_x formation via the thermal path at high power, while other paths may contribute more at low power, due to lower temperatures. Both simulated conditions exhibit asymmetric flames, consistent with visual observations during the experiments. Flame asymmetry is attributed to features in the oxidizer flow upstream of the nozzle, specifically a 90° turn after the throttle valve, as reported in [82] (Chap. 5). A notable portion of oxidizer flow enters the combustion chamber through a gap between the nozzle and burner case, forming a low-temperature annular stream. Analyses of the NO formation rate show that at low power most NO is formed in the core of the flame. At high power, a significant amount of NO is formed where the high-temperature region composed mainly of burnt gases meets the annular stream of oxidizer coming from the gap between the nozzle and burner case.

The simulations of the industrial gas burner show that CFD accurately predicts the flue gas temperature at all conditions. The difference between CFD predictions and experimental results ranges from a minimum of 0.13% to a maximum of 0.65%. The large differences between adiabatic and CFD temperatures highlight the significant impact of radiation and convective heat transfer in the considered problem, with differences ranging from 430.1 K to 757.5 K across operating conditions A to D. Including TRI in the analyses proves to be relevant for improving prediction accuracy, as the temperature computed without TRI is found to be 3.32% higher than the measured value at operating condition D (maximum power). The

study concludes that the CFD set-up accurately captures non-adiabatic phenomena' effects on gas temperature, given the excellent agreement between CFD predictions and measured data.

Methods M1 and M2, based on the FGM scalar transport approach, consistently overpredict NO emissions. The NO emission predicted M2, method that accounts for the effect of non-adiabatic phenomena on NO formation, predicts NO emissions to be 37.6% to 47.6% lower than that predicted with M1. The sum of contributions method M3 provides better predictions than M1 and M2, improving the agreement with experimental data at operating conditions where the thermal path dominates (regimes C and D). However, at conditions A and B, discrepancies with measured data arise, possibly due to lower temperatures and smaller high-temperature regions, conditions that make prompt and N_2O -intermediate mechanisms more relevant. Method M3 does not consider NO oxidation into NO_2 , causing inaccuracies when this reaction is significant. Conversely, methods M1 and M2, which account for NO oxidation, better predict the trend at lower power. CFD predicts the trend of NO_2 decreasing with increasing thermal power, although the difference between measured and computed values remains significant. Measured NO_2 decreases from 22 $\text{ppm}_{\text{v,d}}$ to 2 $\text{ppm}_{\text{v,d}}$, while the computed value decreases from 3 $\text{ppm}_{\text{v,d}}$ to 1 $\text{ppm}_{\text{v,d}}$. These differences may derive from inaccuracies in the tabulated source term for the NO_2 equation, which relies on the molar concentration of NO computed with steady flamelet equations. Finally, part of the differences between predicted and measured NO_x emissions of the industrial gas burner may be due to the use of a RANS approach rather than a higher-fidelity LES approach.

Chapter 7

Conclusions and Future Work

This thesis has presented a comprehensive analysis of the fluid dynamics and pollutant formation in a non-premixed industrial gas burner, contributing novel insights into both cold flow characteristics and NO_x formation mechanisms. Using advanced CFD modeling validated with both experimental data in the literature and new bespoke experimental work, this study has advanced knowledge in two key areas, namely the non-reactive flow characteristics of industrial burners, featuring complex 3D patterns, and the formation processes of nitrogen oxides during combustion in such burners.

The work presented provides guidelines and validation for modeling NO_x emissions in industrial burners in the context of Reynolds-Averaged Navier-Stokes computational fluid dynamics, using the Flamelet Generated Manifold approach for chemistry and the Reynolds stress model for turbulence closure. Three approaches to modeling NO_x formation are tested. This modeling framework enables industries to simulate combustion processes more accurately, facilitating the design of burners that minimize NO_x emissions. In addition, by pinpointing specific zones and conditions that lead to increased NO_x formation, industries can implement targeted control measures, such as adjusting fuel-air mixing or modifying burner geometry, to mitigate emissions.

In the first phase of the CFD set-up development, the problem of modeling

turbulent combustion in diffusion flames was investigated by considering the Sandia flame D, using this reference test case in validating the developed CFD set-ups. The simulations of the Sandia flame D were carried out using both RANS- and LES-based approaches for the turbulence closure. Overall, all numerical results were in agreement with experimental data. The cross-comparison of simulations and experiments highlighted that the RANS approach predicts faster fuel and oxidizer mixing than observed in the experiment, most likely due to complex turbulent patterns of fuel jets poorly resolved by RANS turbulence closures. Conversely, the LES analysis improved mixing rate predictions, achieving good agreement with measured longitudinal profiles of mixture fraction, temperature, CO and OH mass fractions. Although the peak temperature is consistently well predicted, irrespective of turbulence modeling, the LES predictions of the CO and OH peaks are closer to measured values than the RANS analysis, which the latter analysis tending to overpredict the CO peak and underpredict the OH peak. Thus, it is highlighted that LES enables sufficiently accurate modeling of chemistry and turbulence-chemistry interaction. The FGM scalar transport methods used for modeling pollutant formation consistently overpredict NO peak, both with RANS and LES, but the proposed correction for non-adiabatic effects improves the CFD predictions of this variable. The 'sum of contributions' approach, whereby the total NO formation rate is determined by adding the NO formation rate due to thermal, prompt, and N₂O intermediate mechanisms, underpredicts the NO profile. Such occurrence is attributed to the model describing the prompt path contribution, which significantly underpredicts the amount of NO formed near the front flame via the prompt mechanism. This is highly relevant in a flame such as Sandia Flame D, where the prompt pathway is the predominant contributor to NO formation. An analysis based on experimental data and available literature shows that the model describing the thermal path contribution gives accurate predictions if proper oxygen atom concentration modeling is used. This conclusion hints at the fact that the 'sum of contribution' approach may lead to better results when the investigated problem is

characterized by higher temperatures such as those of the industrial burner at hand. In these cases it is expected that the thermal path becomes the main contributor to NO formation.

The second phase of the CFD set-up development focused on the study of the cold flow physics (without combustion) of the industrial gas burner under investigation, characterized by notable geometric and fluid dynamic complexity. Fluid dynamic modeling challenges arose due to sharp turns, backward facing steps, and transversally injected jets. A test rig was also set up to perform experimental measurements to be used for validating the CFD analyses. The cold flow experiments and simulations provided an understanding of the key flow patterns, which influence combustion dynamics and, consequently, pollutant formation. Such flow patterns generated an asymmetric flow in the combustion chamber, which was later observed in the flame as well, both in CFD simulations and physical tests. Since these features influence the flame, accurately modeling them is crucial. However, they also significantly increase the complexity of modeling the industrial burner. Among different turbulence models tested, the Reynolds stress model with baseline ω equation was identified as the best compromise in terms of accuracy, stability, and computational cost. The model was particularly effective in replicating experimental observations, especially under full-load conditions. Overall, the use of wall functions to describe wall-bounded flows affected the simulations' accuracy. Flow separations were identified in certain regions of the burner. Here the wall function approach shows its limits. The evidence that flow separations did not cover the majority of the internal surfaces of the burner prompted the strategy of refining the near-wall grid and resolving BLs only in separated flow regions while using wall functions elsewhere in the subsequent reactive flow analyses of the industrial burner. This hybrid set-up would enable achieving reduced computational costs and overall adequate solution fidelity. The aforementioned findings contribute new guidelines for selecting and applying turbulence models and defining numerical strategies in the analysis of industrial burners of the considered type. They also emphasize the value of accurate

cold flow modeling as a precursor of optimized reactive flow analyses.

Building on the numerical and physical findings of the Sandia Flame D analyses and those of the cold flow analyses of the industrial burner, the investigation of the fluid dynamics and NO_x formation of the non-premixed gas burner under investigation was carried out for various load conditions. The main analyses used time-dependent RANS simulations with the Reynolds stress model and the ω baseline equation, and also experimental data acquired by developing, building, and using a bespoke test rig. The rig was a full scale replica of the industrial burner with minimal alterations with respect to the original design which did not result in any difference between the key nondimensional parameters of the original design and the test rig variant. The flames of the burner, operating at power output between 41.7 kW and 87.5 kW, exhibited a notable lack of axial symmetry, a feature attributed to the asymmetry of the oxidizer flow. The CFD analyses accurately predicted flue gas temperatures, showing excellent agreement with experimental data, with deviations ranging from 0.13% to 0.65%. A comparison with the adiabatic flame temperatures computed for the tested equivalence ratios highlighted the role of non-adiabatic phenomena, with radiation and convective heat transfer causing significant differences between adiabatic and CFD temperatures. High-power regimes are characterized by wide high-temperature regions, an occurrence favoring NO formation via thermal pathways, whereas at low power, lower temperatures make such mechanism less pronounced. Three NO formation modeling strategies were assessed. The FGM scalar transport methods (M1 and M2), overpredict NO emissions, though M2, accounting for non-adiabatic effects with a modeling strategy proposed and developed in this study, yields improved accuracy. The 'sum of contributions' method (M3) performs better at high-power regimes, dominated by thermal NO formation, but underperforms at low-power regimes, where prompt and N_2O -intermediate mechanisms are more significant. The predictions of NO_2 , while capturing the overall trends observed in the experiments, reveal quantitative discrepancies with the same experimental data, likely due to limitations in the

tabulated source term of the NO_2 mass fraction transport equation. The most probable issue with such term is the fact that it relies on the molar concentration of NO computed with steady flamelet equations. While leading to good results in many cases, steady flamelets have often proven to be inaccurate in predicting NO mass fraction. This is because of their tendency to predict equilibrium concentrations in positions downstream of the flame front, while NO is typically present in sub-equilibrium concentrations.

Expanding on the findings and methodologies developed in the research underlying this thesis, future work could focus on applying the developed simulation-based analysis to optimize the design of industrial gas burners with the objectives of reducing pollutant emissions while maintaining or maximizing burner performance and efficiency. One promising future design avenue emerging from the analyses of the considered gas burner is the simplification of the present design, accomplished, for example, by eliminating unnecessary geometry features yielding flow perturbations potentially detrimental to performance and emissions. Such features include backward facing steps and sharp bends. Furthermore, from a design methodology viewpoint, these design alterations could have the additional benefit of reducing the flow unsteadiness to an extent enabling the use of steady RANS CFD analysis for performance and emission assessments. This reduction of the computational burden would enable both using this relatively high-fidelity analysis approach to assess performance and emissions of significantly different burner design concepts, and deploying the approach in automated design optimization systems. Leveraging new insights into NO_x formation dynamics enabled by the demonstrated simulation approach, new burner and nozzle geometries can be developed to minimize emissions.

In light of the global transition toward cleaner energy, the use of hydrogen as a fuel presents a compelling direction for future research. It is worth mentioning that since prompt NO_x formation is not relevant in hydrogen flames, and thermal NO has been generally well captured by the model used in this work, there is a strong indication that this modeling approach could be applicable to hydrogen combustion.

However, further validation would still be necessary to confirm its accuracy in such conditions. Moreover, while hydrogen combustion poses challenges for flamelet-based models due to preferential diffusion effects, high-turbulence conditions may mitigate these issues, allowing the existing modeling framework to remain largely applicable. However, for scenarios where preferential diffusion is significant, the demonstrated modeling strategy can be adapted to include appropriate corrections (e.g. [50]). These efforts will require rigorous validation to ensure accuracy and reliability. Through these extensions, future research can further enhance the efficiency and sustainability of the industrial burner technologies.

While the study offers valuable insights, it is important to acknowledge certain limitations. In particular, quantitative discrepancies in NO emissions arise when the prompt NO mechanism plays a significant role in the combustion process. Furthermore, the model exhibits divergence between measured and predicted NO₂ levels. These issues suggest that further refinement of the modeling approach is needed for accurate emission forecasting, especially in scenarios where such mechanisms are prominent. Another limitation is the specificity of the setup. The experiments and simulations were conducted using a particular burner design and fuel under well-defined conditions. The results may not directly translate to different burners or fuel compositions. For different applications, further testing and model validation across diverse configurations would be necessary.

Bibliography

- [1] Ebrahim Abtahizadeh, Philip de Goey, and Jeroen van Oijen. “LES of Delft Jet-in-Hot Coflow burner to investigate the effect of preferential diffusion on autoignition of CH₄/H₂ flames”. In: *Fuel* 191 (2017), pp. 36–45. ISSN: 0016-2361.
- [2] Ansys-Inc. *Fluent theory guide, release 2019.r3*. <https://www.ansys.com/Products/Fluids/ANSYS-Fluent>. Accessed on 11 May 2022. 2019.
- [3] Ansys-Inc. *ANSYS ICEM CFD User Manual*. 2021.
- [4] Ansys-Inc. *Fluent theory guide, release 2021.r2*. <https://www.ansys.com/Products/Fluids/ANSYS-Fluent>. Accessed on 08 Feb 2023. 2021.
- [5] Ansys-Inc. *Fluent user guide, release 2021.r2*. <https://www.ansys.com/Products/Fluids/ANSYS-Fluent>. Accessed on 08 Feb 2023. 2021.
- [6] B.F. Magnussen and B.H. Hjertager. “On mathematical modeling of turbulent combustion with special emphasis on soot formation and combustion”. In: *Symposium (International) on Combustion* 16.1 (1977), pp. 719–729. ISSN: 0082-0784.
- [7] R.S. Barlow and J. Frank. *TNF Workshop*. <https://tnfworkshop.org/data-archives/pilotedjet/ch4-air/>. Accessed on 14 March 2023. 2003.
- [8] R.S. Barlow and J.H. Frank. “Effects of turbulence on species mass fractions in methane/air jet flames”. In: *Symp. (Int.) Combust.* 27 (1998), pp. 1087–1095. ISSN: 0082-0784.

-
- [9] BBC. *Rishi Sunak: Need more pragmatic approach to net zero*. <https://www.bbc.com/news/av/uk-politics-66871115>. Accessed on 15 December 2024. 2023.
- [10] BOC. *G25 test gas datasheet*. <https://www.boconline.co.uk/shop/en/uk/1-200bar-g25-test-gas-149781>. Accessed on 20 December 2023. 2023.
- [11] Joseph Boussinesq. *Essai sur la theorie des eaux courantes*. Vol. XXIII. 1. Paris: Imprimerie Nationale, 1877.
- [12] *Building Trust through an Equitable and Inclusive Energy Transition*. World economic forum, 2024.
- [13] C. Schluckner and C. Gaber and M. Landfahrer and M. Demuth and C. Hochenauer. “Fast and accurate CFD-model for NO_x emission prediction during oxy-fuel combustion of natural gas using detailed chemical kinetics”. In: *Fuel* 264 (2020), p. 116841. ISSN: 0016-2361.
- [14] R. Cabra et al. “Lifted methane–air jet flames in a vitiated coflow”. In: *Combust. Flame* 143 (2005), pp. 491–506. ISSN: 0010-2180.
- [15] Changyeop Lee and Sewon Kim and Minjun Kwon. “An Experimental Study on Industrial Boiler Burners Applied Low NO_x Combustion Technologies”. In: *Journal of Clean Energy Technologies* 4.6 (2016), pp. 430–434.
- [16] Ping Cheng. “Two-dimensional radiating gas flow by a moment method”. In: *AIAA Journal* 2 (1964), pp. 1662–1664.
- [17] *Coal 2023*. IEA, 2023.
- [18] P.J. Coelho, O.J. Teerling, and D. Roekaerts. “Spectral radiative effects and turbulence/radiation interaction in a non-luminous turbulent jet diffusion flame”. In: *Combust. Flame* 133 (2003), pp. 75–91. ISSN: 0010-2180.

- [19] European Commission. *Regulation of the European Parliament and of the Council establishing the Just Transition Fund*. <https://www.europarl.europa.eu/legislative-train/theme-regional-development-regi/file-just-transition-fund>. Accessed on 15 December 2024. 2023.
- [20] G.G. De Soete. “Overall reaction rates of NO and N₂ formation from fuel nitrogen”. In: *Symp. (Int.) Combust.* 15 (1975), pp. 1093–1102. ISSN: 0082-0784.
- [21] He Du et al. “Influence of the Parallel C-Layer Secondary Air on Flow, Combustion and Nox Generation Characteristics of a 600mwe FW Down-Fired Boiler Retrofitted with a Stable Combustion Organization Mode”. In: *Combust. Sci. Technol.* 0 (2022), pp. 1–25.
- [22] Yifan Duan et al. “LES of the Sandia flame series D-F using the Eulerian stochastic field method coupled with tabulated chemistry”. In: *Chinese J. Aeronaut.* 33 (2020), pp. 116–133. ISSN: 1000-9361.
- [23] V. Dupont et al. “The reduction of NO_x formation in natural gas burner flames”. In: *Fuel* 72 (1993), pp. 497–503. ISSN: 0016-2361.
- [24] Marcin Dutka, Mario Ditaranto, and Terese Løvås. “NO_x emissions and turbulent flow field in a partially premixed bluff body burner with CH₄ and H₂ fuels”. In: *International Journal of Hydrogen Energy* 41 (2016), pp. 12397–12410. ISSN: 0360-3199.
- [25] E. R. G. Eckert. “Radiative transfer, H. C. Hottel and A. F. Sarofim, McGraw-Hill Book Company, New York, 1967. 52 pages”. In: *AIChE Journal* 15 (1969), pp. 794–796.
- [26] Hossam Elasrag and Shaoping Li. “Investigation of extinction and reignition events using the flamelet generated manifold model”. In: *ASME Turbo Expo 2018: Turbomachinery Technical Conference and Exposition*. Vol. Volume 4A: Combustion, Fuels, and Emissions. 2018, V04AT04A023.

-
- [27] Endress+Hauser. *F300 Promass Flow Meter*. <https://www.endress.com/en/field-instruments-overview/flow-measurement-product-overview/coriolis-flowmeter-promass-f300-8f3b?t.tabId=product-overview>. Accessed on 23 August 2023. 2023.
- [28] Erfan Khodabandeh and Hesam Moghadasi and Mohsen Saffari Pour and Mikael Ersson and Pär G. Jönsson and Marc A. Rosen and Alireza Rahbari. “CFD study of non-premixed swirling burners: Effect of turbulence models”. In: *Chin. J. Chem. Eng.* 28.4 (2020), pp. 1029–1038. ISSN: 1004-9541.
- [29] Qi Fengsheng et al. “Numerical study on characteristics of combustion and pollutant formation in a reheating furnace”. In: *Therm. Sci.* 22 (2018), pp. 2103–2112. ISSN: 1540-7489.
- [30] J.H. Frank, R.S. Barlow, and C. Lundquist. “Radiation and nitric oxide formation in turbulent non-premixed jet flames”. In: *Proc. Combust. Inst.* 28 (2000), pp. 447–454. ISSN: 1540-7489.
- [31] S. Fu, B.E. Launder, and M.A. Leschziner. “Modelling strongly swirling recirculating jet flow with Reynolds-stress transport closures”. In: *6th Symposium on Turbulent Shear Flows*. Jan. 1987, 17_6_1–17_6_6.
- [32] G.D. Rago and G. Rossiello and R. Dadduzio and T. Giani and A. Saponaro and F. Cesareo and M. Lacerenza and F. Fornarelli and G. Caramia and B. Fortunato and S.M. Camporeale and M. Torresi and V. Panebianco. “CFD analysis of a swirl stabilized coal combustion burner”. In: *Energy Procedia* 148 (2018), pp. 703–711. ISSN: 1876-6102.
- [33] Gautham Krishnamoorthy and Md Ashiqur Rahman. “Assessing the role of turbulence-radiation interactions in hydrogen-enriched oxy-methane flames”. In: *Int. J. Hydrog. Energy* 43.11 (2018), pp. 5722–5736. ISSN: 0360-3199.
- [34] Massimo Germano et al. “A dynamic subgrid-scale eddy viscosity model”. In: *Phys. Fluids A-Fluid* 3 (1991), pp. 1760–1765.

- [35] M. M. Gibson and B. E. Launder. “Ground effects on pressure fluctuations in the atmospheric boundary layer”. In: *J. Fluid Mech.* 86 (1978), pp. 491–511.
- [36] Peter Glarborg, James A. Miller, and Robert J. Kee. “Kinetic modeling and sensitivity analysis of nitrogen oxide formation in well-stirred reactors”. In: *Combust. Flame* 65 (1986), pp. 177–202. ISSN: 0010-2180.
- [37] Guillaume Godel, Pascale Domingo, and Luc Vervisch. “Tabulation of NO_x chemistry for Large-Eddy Simulation of non-premixed turbulent flames”. In: *Proc. Combust. Inst.* 32 (2009), pp. 1555–1561. ISSN: 1540-7489.
- [38] Joyeeta Gupta. “A history of international climate change policy”. In: *WIREs Climate Change* 1.5 (2010), pp. 636–653.
- [39] Ronald K. Hanson and Siamak Salimian. “Survey of Rate Constants in the N/H/O System”. In: *Combustion Chemistry*. New York, NY: Springer, 1984. Chap. 25, pp. 361–421. ISBN: 978-1-4684-0186-8.
- [40] Hao Zhou and Sheng Meng. “Numerical prediction of swirl burner geometry effects on NO_x emission and combustion instability in heavy oil-fired boiler”. In: *Appl. Therm. Eng.* 159 (2019), p. 113843. ISSN: 1359-4311.
- [41] Di He et al. “Model Comparisons of Flow and Chemical Kinetic Mechanisms for Methane–Air Combustion for Engineering Applications”. In: *Applied Sciences* 11 (2021). ISSN: 2076-3417.
- [42] John Christopher Hewson. *Pollutant emissions from nonpremixed hydrocarbon flames*. University of California, San Diego, 1997.
- [43] John B Heywood. *Internal combustion engine fundamentals*. McGraw-Hill Education, 1988.
- [44] Takafumi Honzawa et al. “Experimental and numerical study of water sprayed turbulent combustion: Proposal of a neural network modeling for five-dimensional flamelet approach”. In: *Energy and AI* 5 (2021), p. 100076. ISSN: 2666-5468.

-
- [45] Matthias Ihme, Chong M. Cha, and Heinz Pitsch. “Prediction of local extinction and re-ignition effects in non-premixed turbulent combustion using a flamelet/progress variable approach”. In: *Proc. Combust. Inst.* 30 (2005), pp. 793–800. ISSN: 1540-7489.
- [46] Matthias Ihme and Heinz Pitsch. “Modeling of radiation and nitric oxide formation in turbulent nonpremixed flames using a flamelet/progress variable formulation”. In: *Phys. Fluids* 20 (2008), p. 055110.
- [47] TSI incorporated. *LCA501 rotating vane anemometer*. <https://tsi.com/products/ventilation-test-instruments/airflow-instruments/airflow-instruments-rotating-vanes/airflow-instruments-rotating-vanes-lca501/>. Accessed on 23 August 2023. 2023.
- [48] G. Indelicato et al. “An efficient modeling framework for wall heat flux prediction in rocket combustion chambers using non adiabatic flamelets and wall-functions”. In: *Int. J. Heat Mass Transf.* 169 (2021), p. 120913. ISSN: 0017-9310.
- [49] J. Warnatz. “NO_x formation in high temperature processes”. In: *Proc. Eurogas '90*. 1990, pp. 303–320.
- [50] Reo Kai et al. “LES flamelet modeling of hydrogen combustion considering preferential diffusion effect”. In: *International Journal of Hydrogen Energy* 48.29 (2023), pp. 11086–11101. ISSN: 0360-3199.
- [51] Kane. *CHSP5 285mm high temperature probe*. <https://www.kane.co.uk/shop/products/chsp5>. Accessed on 23 August 2023. 2023.
- [52] Kane. *Kane 988 Industrial Flue Gas Analyser*. <https://www.kane.co.uk/products/kane988-industrial-flue-gas-analyser>. Accessed on 23 August 2023. 2023.
- [53] Theodore von Kármán. “Mechanical similitude and turbulence”. In: 1931.

- [54] Hiroki Kasuya et al. “LES/flamelet/ANN of oxy-fuel combustion for a supercritical CO₂ power cycle”. In: *Applications in Energy and Combustion Science* 12 (2022), p. 100083. ISSN: 2666-352X.
- [55] A. Ketelheun et al. “NO prediction in turbulent flames using LES/FGM with additional transport equations”. In: *Proc. Combust. Inst.* 33 (2011), pp. 2975–2982. ISSN: 1540-7489.
- [56] JS Kim and FA Williams. “Extinction of diffusion flames with nonunity Lewis numbers”. In: *J. Eng. Math.* 31 (1997), pp. 101–118.
- [57] G. Kuenne, A. Ketelheun, and J. Janicka. “LES modeling of premixed combustion using a thickened flame approach coupled with FGM tabulated chemistry”. In: *Combust. Flame* 158 (2011), pp. 1750–1767. ISSN: 0010-2180.
- [58] Lancaster University. *High End Computing (HEC)*. www.lancaster.ac.uk/iss/info/IThandouts/hec/HEC-flyer.pdf. Accessed on 20 December 2023.
- [59] B. E. Launder, G. J. Reece, and W. Rodi. “Progress in the development of a Reynolds-stress turbulence closure”. In: *J. Fluid Mech.* 68 (1975), pp. 537–566.
- [60] B. E. (Brian Edward) Launder. *Lectures in mathematical models of turbulence / B. E. Launder and D. B. Spalding*. eng. London: Academic Press, 1972.
- [61] Brian Launder. “Second-Moment closure and its use in modelling turbulent industrial flows”. In: *International Journal for Numerical Methods in Fluids* 9 (1989), pp. 963–985.
- [62] Brian Launder. “Second-moment closure: present... and future?” In: *International Journal of Heat and Fluid Flow* 10 (1989), pp. 282–300.
- [63] D. K. Lilly. “A proposed modification of the Germano subgrid-scale closure method”. In: *Phys. Fluids A-Fluid* 4 (1992), pp. 633–635.

-
- [64] Lin, Jiming and Bao, Ming and Zhang, Feng and Zhang, Yong and Yang, Jianhong. “Numerical and Experimental Investigation of a Non-Premixed Double Swirl Combustor”. In: *Energies* 15.2 (2022). ISSN: 1996-1073.
- [65] Kimo Electronic Pvt. Ltd. *Kimo MP 200 P Thermo Anemometer Manometer datasheet*. <https://www.netzerotools.com/assets/images/pdfs/kimo/mp200/NZ-kimo-MP200-manometer-datasheet.pdf>. Accessed on 03 October 2022.
- [66] B Magnussen. “On the structure of turbulence and a generalized eddy dissipation concept for chemical reaction in turbulent flow”. In: *19th aerospace sciences meeting*. 1981, p. 42.
- [67] B.M. Masum et al. “Effect of ethanol–gasoline blend on NO_x emission in SI engine”. In: *Renewable Sustainable Energy Rev.* 24 (2013), pp. 209–222. ISSN: 1364-0321.
- [68] F. Menter. “Stress-Blended Eddy Simulation (SBES)—A New Paradigm in Hybrid RANS-LES Modeling”, booktitle=”Progress in Hybrid RANS-LES Modelling”. In: ed. by Yannick Hoarau et al. Cham: Springer International Publishing, 2018, pp. 27–37. ISBN: 978-3-319-70031-1.
- [69] Florian Menter, M. Kuntz, and RB Langtry. “Ten years of industrial experience with the SST turbulence model”. In: *Heat and Mass Transfer* 4 (Jan. 2003).
- [70] Florian R Menter. “Two-equation eddy-viscosity turbulence models for engineering applications”. In: *AIAA journal* 32 (1994), pp. 1598–1605.
- [71] Florian R Menter. “Review of the shear-stress transport turbulence model experience from an industrial perspective”. In: *International journal of computational fluid dynamics* 23 (2009), pp. 305–316.
- [72] Florian R Menter. “Best practice: scale-resolving simulations in ANSYS CFD”. In: *ANSYS Germany GmbH* 1 (2012).

- [73] Christoph Meraner et al. “Cold flow characteristics of a novel bluff body hydrogen burner”. In: *International Journal of Hydrogen Energy* 43 (2018), pp. 7155–7168. ISSN: 0360-3199.
- [74] M Missaghi. *Mathematical modelling of chemical sources in turbulent combustion*. The University of Leeds, Leeds, UK, 1987.
- [75] A. Morrall, S. Quayle, and M.S. Campobasso. “Turbulence modelling for RANS CFD analyses of multi-nozzle annular jet pump swirling flows”. In: *International Journal of Heat and Fluid Flow* 85 (2020), p. 108652. ISSN: 0142-727X.
- [76] C.M. Müller, H. Breitbach, and N. Peters. “Partially premixed turbulent flame propagation in jet flames”. In: *Symp. (Int.) Combust.* 25 (1994), pp. 1099–1106. ISSN: 0082-0784.
- [77] *Net Zero by 2050*. IEA, 2023.
- [78] Nhan, H.K. and Kwon, M. and Kim, S. and Park, H.P. “CFD investigation of NO_x reduction with a flue-gas internal recirculation burner in a mid-sized boiler”. In: *J. Mech. Sci. Technol.* 33 (2019), pp. 2967–2978.
- [79] Nicol, D. G. and Steele, R. C. and Marinov, N. M. and Malte, P. C. “The Importance of the Nitrous Oxide Pathway to NO_x in Lean-Premixed Combustion”. In: *J. Eng. Gas Turbines Power* 117.1 (Jan. 1995), pp. 100–111. ISSN: 0742-4795.
- [80] Angela O. Nieckele, Monica F. Naccache, and Marcos Sebastião P. Gomes. “Combustion performance of an aluminum melting furnace operating with natural gas and liquid fuel”. In: *Appl. Therm. Eng.* 31 (2011), pp. 841–851. ISSN: 1359-4311.
- [81] Clemens Olbricht et al. “Assessing the Predictive Capabilities of Combustion LES as Applied to the Sydney Flame Series”. In: *Flow Turbul. Combust.* 85 (Dec. 2010), pp. 513–547. ISSN: 1573-1987.

-
- [82] A. Ortolani et al. “Numerical and Experimental Analysis of the Cold Flow Physics of a Nonpremixed Industrial Gas Burner”. In: *J. Fluids Eng.* 145.8 (Apr. 2023), p. 081202.
- [83] A. Ortolani et al. “Numerical and experimental analysis of the formation of nitrogen oxides in a non-premixed industrial gas burner”. In: *Results in Engineering* 23 (2024), p. 102392. ISSN: 2590-1230.
- [84] P.C. Malte and D.T. Pratt. “Measurement of atomic oxygen and nitrogen oxides in jet-stirred combustion”. In: *Symp. (Int.) Combust.* 15.1 (1975). Fifteenth Symposium (International) on Combustion, pp. 1061–1070. ISSN: 0082-0784.
- [85] Pradeep Pantangi et al. “LES of Premixed Methane Flame Impinging on the Wall Using Non-adiabatic Flamelet Generated Manifold (FGM) Approach”. In: *Flow Turbul. Combust.* 92 (June 2014), pp. 805–836. ISSN: 1573-1987.
- [86] François Pecquery et al. “Modelling nitrogen oxide emissions in turbulent flames with air dilution: Application to LES of a non-premixed jet-flame”. In: *Combust. Flame* 161 (2014), pp. 496–509. ISSN: 0010-2180.
- [87] Peiyong Ni and Xiangli Wang. “Modeling the Formation of Nox and Soot Emissions in a Diesel Engine at Different Humidity”. In: *Int. J. Green Energy* 9.8 (2012), pp. 815–828.
- [88] N. Peters. “Laminar diffusion flamelet models in non-premixed turbulent combustion”. In: *Prog. Energ. Combust.* 10 (1984), pp. 319–339. ISSN: 0360-1285.
- [89] Charles D. Pierce and Parviz Moin. “Progress-variable approach for large-eddy simulation of non-premixed turbulent combustion”. In: *J. Fluid Mech.* 504 (2004), pp. 73–97.
- [90] H. Pitsch and H. Steiner. “Large-eddy simulation of a turbulent piloted methane/air diffusion flame (Sandia flame D)”. In: *Phys. Fluids* 12 (2000), pp. 2541–2554.

- [91] Heinz Pitsch and Matthias Ihme. “An unsteady/flamelet progress variable method for LES of nonpremixed turbulent combustion”. In: *43rd AIAA Aerospace Sciences Meeting and Exhibit*. 2005, p. 557.
- [92] Heinz Pitsch and Helfried Steiner. “Scalar mixing and dissipation rate in large-eddy simulations of non-premixed turbulent combustion”. In: *Proc. Combust. Inst.* 28 (2000), pp. 41–49. ISSN: 1540-7489.
- [93] Reuters. *Germany approves bringing coal-fired power plants back online this winter*. <https://www.reuters.com/business/energy/germany-approves-bringing-coal-fired-power-plants-back-online-this-winter-2023-10-04/>. Accessed on 15 December 2024. 2023.
- [94] Beate Ritz, Barbara Hoffmann, and Annette Peters. “The Effects of Fine Dust, Ozone, and Nitrogen Dioxide on Health”. In: *Dtsch Arztebl Int* 51-52.51-52 (2019), pp. 881–886.
- [95] Rohit Saini et al. “Investigation of NO_x in piloted stabilized methane-air diffusion flames using finite-rate and infinitely-fast chemistry based combustion models”. In: *Thermal Science and Engineering Progress* 5 (2018), pp. 144–157. ISSN: 2451-9049.
- [96] Ch. Schneider et al. “Flow field measurements of stable and locally extinguishing hydrocarbon-fuelled jet flames”. In: *Combust. Flame* 135 (2003), pp. 185–190. ISSN: 0010-2180.
- [97] Testo SE and Co. KGaA. *Testo 622 thermo hygrometer and barometer*. <https://www.testo.com/it-IT/testo-622/p/0560-6220>. Accessed on 23 August 2023. 2023.
- [98] Sensirion. *TA440 thermal anemometer datasheet*. https://tsi.com/getmedia/fd36afb0-67d4-4cf5-a517-cc3743024329/TA410-TA430-440_Thermal_Anemometers_A4_UK_2980548-web?ext=.pdf. Accessed on 03 October 2022. 2014.

-
- [99] Sensirion. *SDP8xx-Analog datasheet*. https://www.mouser.co.uk/datasheet/2/682/SERI_S_A0004817208_1-2524897.pdf. Accessed on 03 October 2022. 2018.
- [100] Tsan-Hsing Shih et al. “A new $k - \epsilon$ eddy viscosity model for high reynolds number turbulent flows”. In: *Computers & Fluids* 24 (1995), pp. 227–238. ISSN: 0045-7930.
- [101] R. Siegel and J. R. Howell.. *Thermal Radiation Heat Transfer*. Hemisphere Publishing Corporation, Washington DC, 1992.
- [102] Sivakumaran Sivaramanan. “Acid rain, causes, effects and control strategies”. In: (Apr. 2015).
- [103] J. Smagorinsky. “General circulation experiments with the primitive equations: I. The basic experiment”. In: *Monthly Weather Review* 91 (1963), pp. 99–164.
- [104] Gregory P. Smith et al. *GRI-Mech 3.0*. <http://combustion.berkeley.edu/gri-mech/version30/>. 2003.
- [105] T. F. Smith, Z. F. Shen, and J. N. Friedman. “Evaluation of Coefficients for the Weighted Sum of Gray Gases Model”. In: *J. Heat. Transf.* 104 (Nov. 1982), pp. 602–608. ISSN: 0022-1481.
- [106] Alexander Snegirev and A. Frolov. “The large eddy simulation of a turbulent diffusion flame”. In: *High Temperature* 49 (Oct. 2011), pp. 690–703.
- [107] S. Solomon et al. “Irreversible climate change due to carbon dioxide emissions”. In: *Proceedings of the national academy of sciences* 106.6 (2009), pp. 1704–1709.
- [108] Charles G. Speziale, Sutanu Sarkar, and Thomas B. Gatski. “Modelling the pressure–strain correlation of turbulence: an invariant dynamical systems approach”. In: *J. Fluid Mech.* 227 (1991), pp. 245–272.

- [109] Mohan Sripathi et al. “Laminar Flamelet Based NO_x Predictions for Gas Turbine Combustors”. In: *ASME Turbo Expo 2014: Turbine Technical Conference and Exposition*. Vol. Volume 4B: Combustion, Fuels and Emissions. 2014, V04BT04A060.
- [110] K. Stephan and A. Laesecke. “The Thermal Conductivity of Fluid Air”. In: *J. Phys. Chem. Ref. Data* 14 (1985), pp. 227–234.
- [111] Stuart W. Churchill and Humbert H.S. Chu. “Correlating equations for laminar and turbulent free convection from a horizontal cylinder”. In: *Int. J. Heat Mass Transf.* 18.9 (1975), pp. 1049–1053. ISSN: 0017-9310.
- [112] Jihao Sun et al. “Reduced Methane Combustion Mechanism and Verification, Validation, and Accreditation (VV&A) in CFD for NO Emission Prediction”. In: *Journal of Thermal Science* 30.2 (Mar. 2021), pp. 610–623.
- [113] William Sutherland. “LII. The viscosity of gases and molecular force”. In: *Lond. Edinb. Dublin Philos. Mag. J. Sci* 36 (1893), pp. 507–531.
- [114] Tao Ren and Michael F. Modest and Daniel C. Haworth. “Simulating turbulence–radiation interactions using a presumed probability density function method”. In: *Int. J. Heat Mass Transf.* 121 (2018), pp. 911–923. ISSN: 0017-9310.
- [115] Trisjono, P and Kleinheinz, K and Pitsch, H and Kang, S. “Large eddy simulation of stratified and sheared flames of a premixed turbulent stratified flame burner using a flamelet model with heat loss”. In: *Flow, turbulence and combustion* 92 (2014), pp. 201–235.
- [116] Tuomas Paloposki and Leif Liedquist. *Steel emissivity at high temperatures*. VTT Tiedotteita - Meddelanden - Research Notes 2299. Finland: VTT Technical Research Centre of Finland, 2005. ISBN: 951-38-6717-X.
- [117] J.A. van Oijen and L.P.H. de Goey. “Modelling of Premixed Laminar Flames using Flamelet-Generated Manifolds”. In: *Combust. Sci. Technol.* 161 (2000), pp. 113–137.

-
- [118] L.M. Verhoeven et al. “Modeling non-premixed laminar co-flow flames using flamelet-generated manifolds”. In: *Combust. Flame* 159 (2012), pp. 230–241. ISSN: 0010-2180.
- [119] Pauline Eugenie Vervisch et al. “NO Relaxation Approach (NORA) to predict thermal NO in combustion chambers”. In: *Combust. Flame* 158 (2011), pp. 1480–1490. ISSN: 0010-2180.
- [120] Frederick A. Villamena. “Chapter 2 - Chemistry of Reactive Species”. In: *Reactive Species Detection in Biology*. Ed. by Frederick A. Villamena. Boston: Elsevier, 2017, pp. 13–64.
- [121] A.W. Vreman et al. “Premixed and nonpremixed generated manifolds in large-eddy simulation of Sandia flame D and F”. In: *Combust. Flame* 153 (2008), pp. 394–416. ISSN: 0010-2180.
- [122] Gernot Wagner and Martin L. Weitzman. *Climate Shock : The Economic Consequences of a Hotter Planet*. Princeton University Press, 2016.
- [123] Steffen Weise et al. “A computationally efficient implementation of tabulated combustion chemistry based on polynomials and automatic source code generation”. In: *Flow Turbul. Combust.* 100 (2018), pp. 119–146.
- [124] Xu Wen et al. “Large eddy simulation of a semi-industrial scale coal furnace using non-adiabatic three-stream flamelet/progress variable model”. In: *Appl. Energ.* 183 (2016), pp. 1086–1097. ISSN: 0306-2619.
- [125] David C Wilcox et al. *Turbulence modeling for CFD*. Vol. 2. DCW industries La Canada, CA, 1998.
- [126] *World Energy Employment 2023*. IEA, 2023.
- [127] Tomasz Wronski et al. “Numerical simulation through Fluent of a cold, confined and swirling airflow in a combustion chamber”. In: *European Journal of Mechanics - B/Fluids* 96 (2022), pp. 173–187. ISSN: 0997-7546.

- [128] Xiao Yang and Zhihong He and Shikui Dong and Heping Tan. “Prediction of turbulence radiation interactions of CH₄H₂/air turbulent flames at atmospheric and elevated pressures”. In: *Int. J. Hydrog. Energy* 43.32 (2018), pp. 15537–15550. ISSN: 0360-3199.
- [129] Yunfei Xing et al. “Large eddy simulation of a turbulent non-premixed flame based on the flamelet-generated manifolds approach and a reduced mechanism verification”. In: *Aerosp. Sci. Technol.* 105 (2020), p. 105952. ISSN: 1270-9638.
- [130] Rakesh Yadav, Shaoping Li, and Ellen Meeks. “A Scale Separation Method for Pollutant Prediction in Turbulent Flames Using Transported Scalars With Flamelet Generated Manifold (FGM) Method”. In: *ASME Turbo Expo 2018: Turbomachinery Technical Conference and Exposition*. Vol. Volume 4B: Combustion, Fuels, and Emissions. 2018, V04BT04A058.
- [131] Yue, Chuanfeng and Wang, Jingbo and Li, Xiangyuan. “Modeling of Sandia Flame D with the non-adiabatic chemistry tabulation approach: the effects of different laminar flames on NO_x prediction”. In: *RSC Adv.* 13.7 (2023), pp. 4590–4600.
- [132] YA Zeldovich, D Frank-Kamenetskii, and P Sadovnikov. *Oxidation of nitrogen in combustion*. Publishing House of the Acad of Sciences of USSR, 1947.
- [133] Weijie Zhang et al. “Large eddy simulation of the Cambridge/Sandia stratified flame with flamelet-generated manifolds: Effects of non-unity Lewis numbers and stretch”. In: *Combust. Flame* 227 (2021), pp. 106–119. ISSN: 0010-2180.
- [134] Yan Zhang et al. “Large eddy simulation of spray combustion using flamelet generated manifolds combined with artificial neural networks”. In: *Energy and AI* 2 (2020), p. 100021. ISSN: 2666-5468.

- [135] Yu Zhang, Yuming Xing, and Sheng Chen. “CFD investigation based on gas burner with low-NO_x strategy of fuel-staging”. In: *IOP Conference Series: Earth and Environmental Science* 153 (May 2018), p. 032022.
- [136] Yu Zhang et al. “Feasibility of biogas and oxy-fuel combustion in steam cracking furnaces: Experimental and computational study”. In: *Fuel* 304 (2021), p. 121393.
- [137] Zhi Yi and Zhenggang Su and Qiangda Yang and Guojun Li and Weijun Zhang. “Study of the non-gray-TRI effect on the turbulent methane combustion under O₂/CO₂ atmosphere”. In: *Appl. Therm. Eng* 130 (2018), pp. 449–457. ISSN: 1359-4311.